The Dissertation Committee for Sahar Ayazianmavi Certifies that this is the approved version of the following dissertation:

Photovoltaic (PV) and Fully-Integrated Implantable CMOS ICs

Committee:

Arjang Hassibi, Supervisor

John A. Pearce

Sanjay K. Banerjee

Adnan Aziz

Eric Soenen

Photovoltaic (PV) and Fully-Integrated Implantable CMOS ICs

by

Sahar Ayazianmavi, B.Sc., M.Sc.

Dissertation

Presented to the Faculty of the Graduate School of

The University of Texas at Austin

in Partial Fulfillment

of the Requirements

for the Degree of

Doctor of Philosophy

The University of Texas at Austin

May 2012

Dedicated to

My Parents, Hamideh and Firouz

My Sisters, Samar and Sara

My Angel, Nickan

And

My Love, Behnam

Acknowledgements

Here, I would like to take the opportunity to acknowledge a group of people who had a role in my educational endeavors. This work, for all the value it has, would have not happened without their support.

My deepest gratitude goes to my advisor, Dr. Arjang Hassibi. His kind mentorship and wise leadership throughout my PhD taught me how to turn an idea into a piece of valuable research work. His unique original ideas in research will be a source of inspiration for me in the rest of my career.

I am grateful to my committee members, Prof. John Pearce, Prof. Sanjay Banerjee, Prof. Adnan Aziz and Dr. Eric Soenen for taking the time to be in my PhD committee and giving me valuable feedbacks, which tremendously add to the value of this dissertation.

I would like to thank Dr. Eric Soenen once more and Taiwan Semiconductor Manufacturing Company (TSMC) for providing us with free tape-out shuttles, which facilitates implementing our research ideas. I greatly appreciate Semiconductor Research Corporation (SRC) for partially funding this project and Center for Nano and Molecular Science (CNM) at the University of Texas at Austin, for providing the facilities for my measurements.

I have learnt the basics of research from two of my professors, Prof. Ali Banai, and Prof. Ranjit Gharpurey. Here, I would like to express my gratitude to them for all I have learnt under their supervision.

I would like to thank Melissa Campos, Debi Prather, Andrew Kieschnik, and Melanie Gulick for their prompt logistic helps.

My special thanks go to my group members, Dr. Arun Manickam and Rituraj Singh for the valuable discussions and brainstorming sessions we had. I am thankful to my UT fellows Dr. Vahid Akhavan, Aaron Chevalier, Shreepriya Das, Babak Fallahazad, Dr. Diptendu Ghosh, Dr. Junghwan Han, Ashish Khandelwal, Rouyo Li, Maryam Mortazavi, and Yousof Mortazavi for all their insightful ideas and helpful discussions.

I am deeply indebted to two of my teachers, Ms. Mansoureh Nikbakht for teaching me how to read and write and Mr. Pirouz Al-e-Bouyeh for believing in my abilities. I take this opportunity to thank them here.

I would like to specially thank my dear friend Shahrzad Mirkhani for all her kindness. My life in Austin has become a very wonderful experience with the companionship of my friends Fatemeh Alavizadeh, Maedeh Faraji, Rouzbeh Ghanbarnezhad, Nasim Hajari, Hoda Hashemi, Zoya Heidari, Maysam Lavasani, Shahriyar Lavasani, Newsha Mirzaie, Mohammad Morovati, Setareh Nematollahi, Ardavan Pedram, Faezeh Raei, Parisa Razaghi, Pooneh Sabouri, Maryam Salimpour, Neda Shahidi, Maryam Vesal, and Sepideh Ziaii. Thanks for making all those beautiful memories.

My special gratitude goes to my dear parents, Hamideh and Firouz, who have been a source of inspiration and a symbol of hard work for me, and to my lovely sisters, Samar and Sara, who have always encouraged me to strive and move forward.

The presence of my son, Nickan, in the past year has brought joy and happiness to my life and has given it a new meaning. I would like to thank him for his beautiful innocent smiles that brighten my days from the beginning.

At the end, I would like to specially thank my husband, Behnam, who has been my best friend, and my source of energy and love. His continuous love and care makes solving all problems easy. Thank you.

Photovoltaic (PV) and Fully-Integrated Implantable CMOS ICs

Sahar Ayazianmavi, Ph.D.

The University of Texas at Austin, 2012

Supervisor: Arjang Hassibi

Today, there is an ever-growing demand for compact, and energy autonomous, implantable biomedical sensors. These devices, which continuously collect *in vivo* physiological data, are imperative in the next generation patient monitoring systems. One of the fundamental challenges in their implementation, besides the obvious size constraints and the tissue-to-electronics biocompatibility impediments, is the efficient means to wirelessly deliver power to them.

This work addresses this challenge by demonstrating an energy-autonomous and fully-integrated implantable sensor chip which takes advantage of the existing on-chip photodiodes of a standard CMOS process as photovoltaic (PV) energy-harvesting cells. This 2.5 mm × 2.5 mm chip is capable of harvesting μW's of power from the ambient light passing through the tissue and performing real-time sensing. This system is also MRI compatible as it includes no magnetic material and requires no RF coil or antennae.

In this dissertation, the optical properties of tissue and the capabilities of the CMOS integrated PV cells are studied first. Next, the implementation of an implantable sensor using such PV devices is discussed. The sensor characterizing and the *in vitro* measurement results using this system, demonstrate the feasibility of monolithically

integrated CMOS PV-driven implantable sensors. In addition, they offer an alternative method to create low-cost and mass-deployable energy autonomous ICs in biomedical applications and beyond.

Table of Contents

List of Tables

List of Figures

Chapter 1: Introduction

1.1 MOTIVATION

Since 1970's the invention of implantable devices has changed the lives of hundreds of thousands of people worldwide for better. These devices sense, correct and communicate physiological functions of the patients' bodies. Cardiac pacemaker [1], for example, is a very successful implementation of such devices. It produces electronic (synthetic) heart pulses when the body cannot. Pacemakers are usually battery-operated and only need checkups every 6 months. Arne Larsson in 1958 in Sweden had the first pacemaker and received 26 different pacemakers throughout his life until 2001. Interestingly, he even outlived his first surgeon and the pacemaker inventor!

To name a few other applications, cochlear implants [2], implantable defibrillators [3], glucose monitoring systems [4], intra-ocular pressure monitor [5], and neuro-modulation devices can be mentioned which are used to treat Parkinson [6], chronic pains [7], etc. Currently, 75,000 people also have Deep Brain Stimulation implants [8].

The design of all of the implantable devices comprises addressing three main challenges which are: *i*) design of tissue-device physical interface, *ii*) data flow and processing, and *iii*) energy source and power management [8]. The focus of this thesis is on the third challenge which is the power management.

In the early generation of implantable devices, wires were used to provide power, and communicate the data, from and to the implant [9]. Although such an approach is still sparsely used in neuroscience [10], it is not acceptable for patient monitoring applications since it is exceptionally inconvenient while drastically increasing the chance of infection. In most applications today (e.g., pacemaker), batteries are implanted with

the device to provide long term power for the electronics [11-12]. This is despite the fact that batteries can be very hazardous if they leak within the body [13]. Also, batteries have limited lifetimes and eventually are discharged; yet it has been demonstrated that by implementing ultra-low power embedded electronics, one can achieve years of functional operation in specific applications [14].

Recently, power delivery through inductive coupling (i.e., near-field coupling) has become popular [15-17]. Using this approach, one can directly power up the device or recharge the implanted battery, if any. In near-field coupling, efficient coupling for reasonable power delivery necessitates proper alignment between the external transmitter coils and the *in vivo* receiver coils. An alternative approach along the same lines is to take advantage of far-field coupling of two antennae in RF and send power from a transmitter to the implanted receiver [18]. In this particular approach, the direction of the radiated RF power (antennae directivity) in view of the directivity of the *in vivo* receiving antenna is critical. In both of these methods, tissue introduces some loss in the power delivery systems which is larger in RF frequency using antennas compared to the inductive coupling approach [19-20].

Regardless of the frequency used, the presence of a relatively large coil or antenna is inevitable in both methods. It is widely known that the larger they are (up to the order of the wavelength which is very large comparable to the size of the chip), the higher the delivered power can be. This is a fundamental disadvantage of this type of power delivery which also makes the implanted devices unsafe in MRI machines. i.e., MRI-incompatible.

In this dissertation, an energy-autonomous and fully-integrated complementary metal-oxide semiconductor (CMOS) implantable sensor chip is presented. The general idea is to take advantage of the existing on-chip photodiodes of the process as

photovoltaic (PV) energy-harvesting photocells to power up the embedded circuitry. The design, and successful implementation of an integrated CMOS integrated circuit (IC) based on this idea is also discussed. This 2.5 mm × 2.5 mm CMOS chip is capable of harvesting μW's of power from the ambient light passing through the tissue to perform real-time sensing while the acquired data can be transmitted in a neuromorphic fashion and by using a set of *in vivo* polarized electrodes [21]. The transmitted signal is then sensed by a set of commercially available Electrocardiography (ECG) electrodes. This power harvesting system implemented in this research is MRI compatible since it requires no RF coil or antenna and contains no paramagnetic material [22].

1.2 OUTLINE

Chapter 2 reviews the methods that have been used to deliver power to implanted devices. In these methods, either the power supply is "wired" to the devices or "wireless" power delivery methods have been applied. All these methods are discussed in detail and the proposed alternate technique which is based on optical power harvesting is introduced.

To examine the feasibility of *in vivo* optical power harvesting, an understanding of the optical characteristics of the body and different types of tissue is required. Chapter 3 studies this and the conditions in which optical power harvesting is feasible based on both literature review and measurements.

Another important challenge is to determine whether integrated CMOS PV cells are capable of harvesting optical power and generating adequate electrical power to run an implantable device. Chapter 4 studies this both in theory and practice and provides a comprehensive discussion regarding the advantages and disadvantages of these devices.

Chapter 5 provides the details in the design of the prototype sensor and explains the challenges of this design.

In Chapter 6, the chip measurement results are demonstrated and Chapter 7 is dedicated to the summary of this dissertation and future work.

Chapter 2: Delivering Power to *In Vivo* Implanted Devices

2.1 INTRODUCTION

Today, there is an ever-growing demand for compact, energy autonomous, and non-invasive *in vivo* implantable biomedical sensors. These devices, which continuously collect *in vivo* physiological data, are imperative in the next generations of patient monitoring systems. One of the fundamental challenges in their implementation, besides the obvious size constraints and the tissue-to-electronics biocompatibility impediments, is the efficient means to wirelessly deliver power to, and receive data from them. This chapter discusses the methods currently used for powering implanted devices. Subsequent to explaining those methods, a new approach which is based on optical energy harvesting using CMOS integrated PV cells is introduced.

2.2 CONNECTED POWER SUPPLIES

The start of using implanted devices goes back fifty years [23]. At the beginning, basic, and to some degree "primitive" methods of powering had been used. In those devices the power supply was physically connected to the device, and wires were used. However, currently wireless methods are preferred. Accordingly, powering methods can be categorized into two major categories. In the first category, the power supply is connected to the device, while in the second power is delivered to the device wirelessly. The following section explains two examples of this type of power supplies in more detail.

2.2.1 Wired Method

In the early generation of implantable devices, wires were mainly used to provide power and communicate the data from and to the system. For example in [9], leads have been used to provide power and receive data from a multichannel probe designed for measuring neural activity. The structure of the microprobe is shown in Fig. 2.1. It acquires the data from eight active recording sites, amplifies it with a gain of ~300 V/V (15 Hz to 7 kHz bandwidth), and sends it to the outside world through a couple of leads. The total power consumption of this probe is 2.5 mW using a 5V power supply.

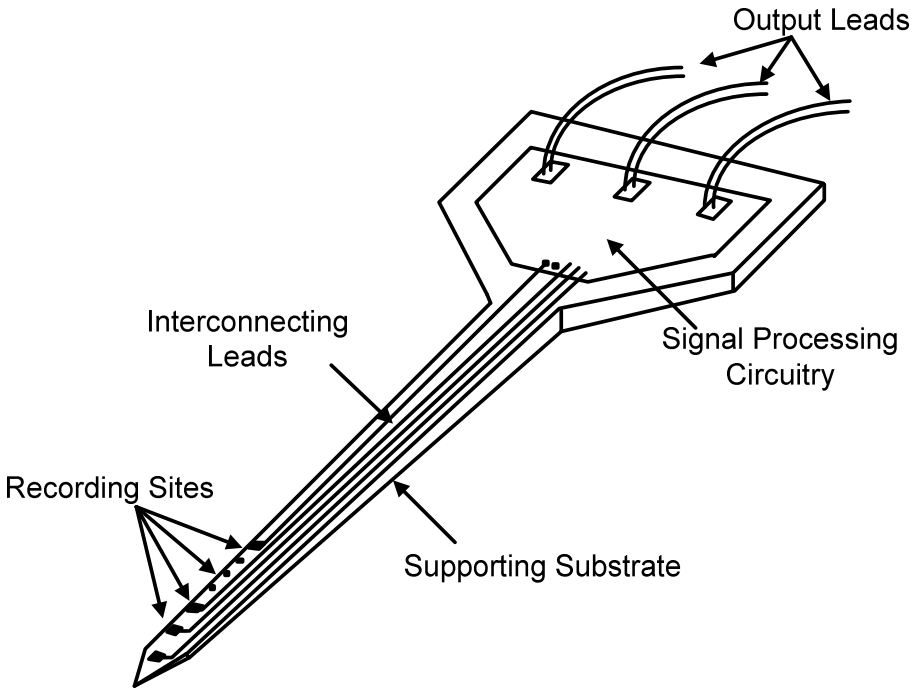

Figure 2.1: Structure of an active multichannel microprobe [9] using "wired" power delivery.

While "wired" approaches are still used; they are limited to research applications. For example, in [10] a neural recording system is implemented for freely behaving primates. In this setup, the chip is powered by batteries but the batteries are integrated

outside the body and connected to the power supply using short wires going through the skull and skin. This device which has an integrated accelerometer, records broadband neural (~30 kS/sec) and acceleration data for up to 48 hours on a removable flash card. Fig. 2.2 shows how wires provide power for such an implanted device.

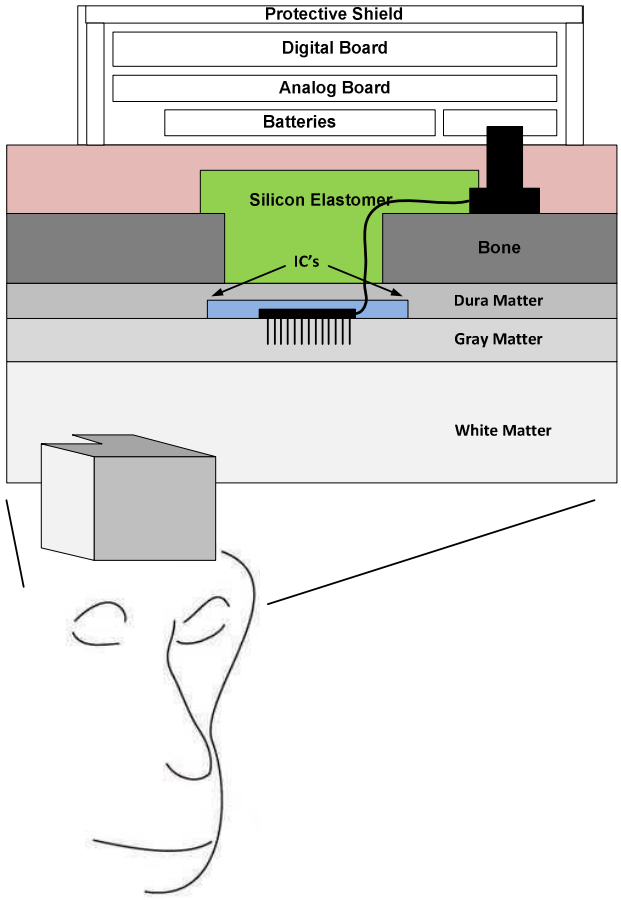

Figure 2.2: Use of wires to connect the battery to the implanted IC [10].

Although this method still has some applications in the research field it is not practical for human monitoring applications since it drastically increases the chance of infection while it introduces extreme constraints in terms of mobility and day-to-day activities.

2.2.2 *In vivo* Batteries

In most of *in vivo* devices today (e.g., pacemakers or cochlear implants), batteries are implanted with the electronics to provide long term and reliable power. For example in [24], two lithium batteries (Sanyo Model CR1220) have been used to power up an intracranial pressure telemetry system. The battery size in this case is ~12 mm in diameter and 2 mm in height with the capacity of 30 mAh. In order to extend the lifetime of the battery, the power-hungry wireless transmitter which consumes 0.4 mW, is shut off by a CMOS RF command receiver and is on for only an hour a day. As a result, the lifetime of the system is extended to more than a year without the need to change the battery.

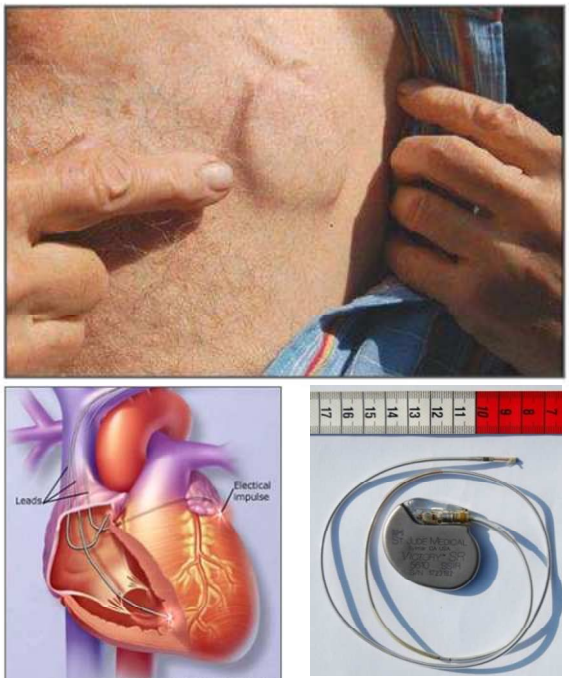

Figure 2.3: Cardiac pacemaker.

In [25], an 8 cm^3, 2.5 Ah lithium battery powers a neurophysiological telemetry system which includes a signal processor and a transmitter. The signal processor amplifies, filters, and multiplexes eight channels of physiological data which include three neural action-potentials, three electrograms and two temperature signals. The transmitter can communicate data for 500 hours, and is capable of operating at a frequency of up to 125 MHz. The lifetime of the system can be multiplied by three if the transmitter is switched to its low-bandwidth mode.

Generally speaking, the lifetime of batteries can be extended by disconnecting the batteries while they are not in use. However, they are fundamentally sub-optimal choices for powering implanted devices because they can be very hazardous if they leak within the body [26]. Clearly, batteries have limited lifetimes and eventually will be fully discharged; yet as discussed before, their lifetime can be extended by using ultra-low power embedded electronics [1]. For example in [1], a pacemaker is designed to continuously deliver monophasic impulses with magnitude of 8V and a current of approximately 15 mA across the 500 Ohms electrode pair. This pacemaker is powered by six mercury cells each of which has a capacity of 1000 mAh. This battery is estimated to operate the system for approximately five years.

Ref	Battery	Size	Capacity	Power	Life-time
[24]	×2 lithium batteries (Sanyo Model CR1220)	0.24 cm^3	30 mAh	0.4 mW	~ 1 year
[25]	×1 lithium battery	8 cm^3	2.5 Ah	11 mW	500 hours
[1]	×6 mercury cells	66.3 cm^3	1000 mAh	120 mW	5 year

Table 2.1: Some examples of the batteries used in implantable devices.

2.3 POWER HARVESTING

It is more convenient to provide power to the implants without physically accessing the device. This is mainly due to the fact that accessing the implant implies surgery. This sub-section discusses powering methods in which the power supply is not physically connected to the device but the power is harvested *in vivo* by using external energy sources. Examples are inductive coupling and RF energy harvesting methods that provide energy to the implants through near field and far field coupling, respectively.

2.3.1 Inductive Coupling (Near-field Magnetic Coupling)

Recently, power delivery through inductive coupling (i.e., near-field magnetic coupling) has become popular [17],[26-27]. In this approach, one can directly power up the device or recharge any storage component *in vivo*, if any. In this approach, efficient

magnetic coupling for reasonable power delivery necessitates proper alignment between the external transmitter coils and the *in vivo* receiver coils.

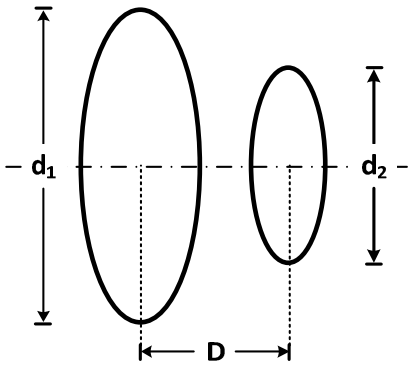

(a)

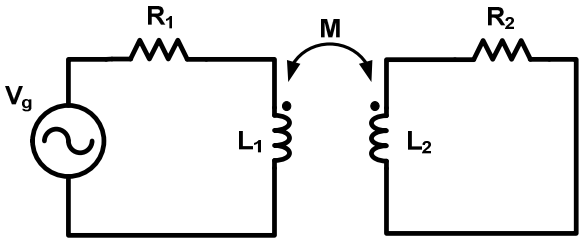

(b)

Figure 2.4: (a) An inductive coupling pair and (b) the equivalent circuit.

In inductive coupling, power transfer occurs by magnetically coupling two coils; i.e., the transmitter coil and the receiver coil represented by L_1 and L_2 in Fig. 2.4b. Usually in this method, L_1 and L_2 are only a few wavelengths apart to reach a reasonable coupling factor (M). In Fig. 2.4b, R_1 represents the equivalent resistor of the power supply and the primary circuit, and R_2 represents the series resistance of the unloaded secondary coil. The frequency for inductive coupling is generally below 10MHz.

In [28], the basic implementation of an inductive coupling system is reported. Fig. 2.5 illustrates this system, where V_{pk} is the peak voltage at the L_2 and C_2 tank and V_O denotes the voltage across the load, i.e., $V_O = V_{pk} - V_{diode}$.

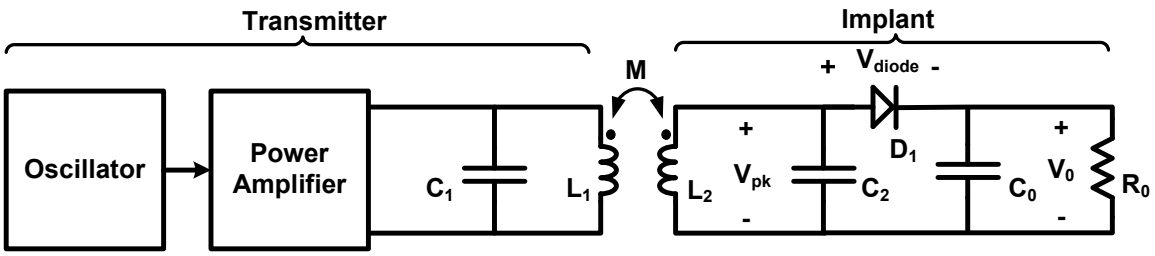

Figure 2.5: Basic inductive coupling circuit.

In this circuit, the diode efficiency is defined by V_O/V_{pk} . In the higher voltage applications such as in [28] where the supply voltage is assumed to be 6 V and $R_O C_O \gg 1/f$, the diode efficiency is ~1, however, when the supply is (on) the efficiency can drop to below 20%. The resistance at which dissipated AC power is equivalent to the DC power in the load is $R = R_O/2$. Now, in order to have a better estimate of the available power at the load, the equivalent circuit from the primary coil is calculated. The equivalent AC resistance seen is

$$R_L = (\omega L_2)^2/R = 2\,(\omega L_2)^2/R_O\,. \tag{2.1}$$

Based on this, the total resistance in the secondary tank is approximately $R_2 + R_L$. Hence, the equivalent reflected resistance to the primary coil, R_e, then becomes

$$R_e = (\omega M)^2/(R_2 + R_L) = R_1 \cdot Rk^2 Q_1 Q_2/(R + Q_2^2 R^2). \tag{2.2}$$

In Equation (2.2) M is the mutual inductance of the coils ($M = k\sqrt{L_1 L_2}$ where k is the coefficient of coupling and a function of the size of the coils and their distance), and $Q_1 = \omega L_1/R_1$ and $Q_2 = \omega L_2/R_2$ are the unloaded quality factors of the primary and secondary coils and the equivalent circuit has the form, which is illustrated in Fig. 2.6.

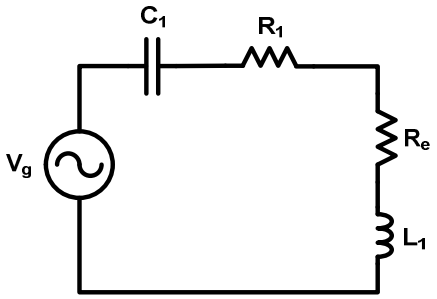

Figure 2.6: Equivalent circuit looking into the primary coil.

From the equivalent circuit, the efficiency of the circuit at resonance, η, can be calculated using the following equations:

$$P_i = \frac{1}{2}\left(\frac{|V_g|^2}{R_e+R_1}\right), \tag{2.3}$$

and

$$P_o = \frac{R_L}{R_L+R_2} \cdot \frac{R_e}{R_1+R_e} \cdot P_i, \tag{2.4}$$

therefore

$$\eta = \frac{P_O}{P_i} = \frac{k^2 Q_1 {Q_2}^3 R_2 R}{(R+{Q_2}^2 R_2)[(1+k^2 Q_1 Q_2)R+{Q_2}^2 R_2]}. \tag{2.5}$$

In the above equations, P_i represents the available power from the power supply, and P_o is the power dissipated at the load equivalent resistance (R_e).

Now, to find out the optimal load, the derivative of the efficiency is set equal to zero with respect to R_2. Therefore, R_{2opt} which is the optimal resistance present at the unloaded secondary circuit, is found by

$$R_{2opt} = \frac{R(1+k^2Q_1Q_2)^{\frac{1}{2}}}{{Q_2}^2}. \quad (2.6)$$

The optimal load results in the optimal efficiency available from a structure, which is

$$\eta_{opt} = \frac{k^2Q_1Q_2}{\left[1+(1+k^2Q_1Q_2)^{\frac{1}{2}}\right]^2}. \quad (2.7)$$

It is important to realize that in these calculations, the medium is assumed to be air and mutual inductance is only a function of the shape of the coils.

Examples of implanted devices powered by inductive coupling are shown in Table 2.2. The frequency of operation is under 10 MHz. The generated power in the devices is obviously a function of the provided power from the transmitter, and can be as high as 1.2 W in [26]. The size of the *in vivo* receiver is usually in the range of a few cm^2 which is considerably larger than the size of the microelectronic devices that are operated by them. As expected from [28], the efficiency in these systems is between 20 to 30%. The efficiency in [29] is 30% which is higher than the predicted value in [28].

Reference	Frequency	Generated Power	TX size (Diameter)	RX size (Diameter)	Distance	Power efficiency
[26] uses antennae in [30]	6.78 MHz	1.2W	5.9cm (4 turns)	3cm (5 turns)	2.5cm	20%
[28]	3.5 MHz	-	5cm (15 turns)	1.25cm (22 turns)	2.5cm	23%
[30]	8.75 MHz	80 mW	5.9cm (4 turns)	3cm (5 turns)	2.54cm	20%
[29]	<1 MHz	242 mW	4cm (34 turns)	2cm (30 turns)	1cm	29.9%

Table 2.2: Examples of the implanted devices powered through inductive coupling.

2.3.2 RF Powering (Far-field Coupling)

An alternative approach along the same lines of inductive coupling is to take advantage of far-field coupling of two antennae in RF frequencies (e.g. above 100 MHz) and send power from an RF transmitter to a receiver [31-33]. In this particular approach, the direction of the power radiating antenna in view of the directivity of the *in vivo* receiving antenna is critical.

In [31], the authors have used RF radiation to power a glaucoma monitoring system that is implanted in the eye of a porcine. Although at RF frequencies tissue introduces significant loss to the RF signals [19-20], such systems can be practical when the antenna is implanted underneath a thin layer of tissue which slightly attenuates the signal. In [31] this loss was reported to be as low as 5dB.

Due to the obvious restriction in the available area inside the body, the *in vivo* antenna ought to be small. This makes the radiation resistance of the antenna small, and therefore reduces the harvested power. Yet, it has been shown in [31] that at 2.4 GHz RF frequency, with an antenna length of around 4% of the wavelength, can harvest enough power to operate the sensor.

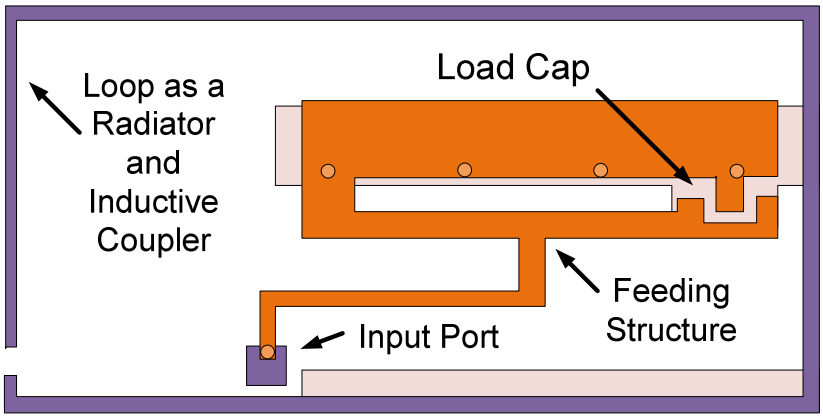

Figure 2.7: The embedded antenna structure in [31].

In [32], the feasibility of powering implanted devices through millimeter and sub-millimeter receiving antennas is studied. The reported results show that a 0.4 mm diameter receiving antenna can harvest 0.46 mW power from a 140 mm diameter transmitting antenna at 20 MHz frequency. However, the voltage transfer ratio is a function of square of the receiver coil diameter, number of turns in the receiver coil, and the permeability of the ferrite cores in the receiver coil. The mutual inductance is minimumm when the coils are in axial alignment and it increases as they move from alignment.

In [33] a 7.62 cm diameter receiver loop harvests power transmitted by an outer loop with the diameter of 12.7 cm. The receiver generates a stable DC voltage of 2.8 V with a DC current of 2 mA from a 50 MHz RF power source with power efficiency of 11%.

Table 2.3 lists the important properties of some of the systems that take advantage of far-field powering methods. These devices work at a higher range of frequency compared to near-field power delivery systems up to a few GHz. They can have significantly smaller sizes at the price of lower power efficiency.

Ref	Frequency	Generated Power	TX size	RX size	Power Efficiency
[31]	2.4 GHz	-	-	0.5 cm (4% of the λ)	1.13%
[32]	20 MHz	0.46mW	140mm diameter	0.4mm diameter	-
[33]	50MHz	5.6 mW	7.62 cm diameter	12.67 cm diameter	11%

Table 2.3: Some examples of the implanted devices powered by RF coupling.

2.3.3 Alternative Methods

In addition to the previously discussed power harvesting techniques, other methods have been reported, which rely on other energy sources such as human motion [34], electrostatic energy [35], and temperature difference [36]. Most of these solutions include a mechanically moving transducer element, and therefore, the analysis of these methods is outside the scope of this work; however, a few of them are briefly discussed here.

In [34], the authors study the possibility of mechanical energy harvesting inside a prototype total knee replacement (TKR). The authors have investigated the power generation efficiency of stiff lead (Pb) Zirconate Titanate (PZT) in implanted devices. PZT is an inorganic compound that shows piezoelectric effects. A voltage difference is created across a PZT when the structure is deformed. According to the results of this research, four units of PZT ceramic elements with the size of 0.5 × 0.5 × 1.8 cm harvest approximately 1.2 mW of power in typical walking condition.

Reference [35] reports a BiCMOS electrostatic energy harvesting system which harvests the vibrational energy. The principle of operation is based on a vibration-driven variable capacitor which can get charged by the ambient kinetic energy. In this system, the charge is held and when the capacitance decreases by plate separation, an electrical current is induced which in turn provides energy for the pre-charger, the harvester, the monitoring and the control microelectronics. The consumed energy is 1.27 nJ, 2.14 nJ, and 2.87nJ per cycle for battery levels of 2.7 V, 3.5 V, and 4.2 V, respectively. This energy level implies generation of 38.1, 64.2, and 86.1nW for a system operating at 30Hz.

Reference [36] introduces an energy harvesting with thermoelectric (TE) devices using unique nano-scale materials. The results of this research demonstrate 775 μW of power created by a $1mm^3$ TE device with an external temperature variation of $\Delta T = 9\ K$. While this power generation level is impressing, this system is less likely to become mainstream. The main reason is that this level of temperature variation deep inside the body does not usually occur and it is maintained at approximately 37 ºC.

Table 2.4 summarizes the characteristics of the discussed alternative power harvesting methods used in implanted devices. As evident, their size and generated power levels can vary according to their physical properties.

Ref	Energy Source	Transducer	Size	Generated Power
[34]	Human motion	Piezoelectric (PZT)	0.45 cm^3	1.2 mW
[35]	Ambient kinetic energy (vibration)	Vibration-driven variable capacitor	$1mm^2$	86.1nW
[36]	Temperature difference	Nano-scale thermoelectric device (TE)	1 mm^3	775 µW

Table 2.4: Some examples of other power harvesting methods for implanted devices.

2.4 THE PROPOSED METHOD

This thesis proposes and shows the feasibility of a new power harvesting method. The general idea is to harvest optical energy that passes through the tissue, using integrated CMOS PV cells. The body tissue introduces optical loss to the light hitting its surface but depending on the amount of incoming energy and the loss, a portion of the optical energy can be harvested and converted to electrical power.

A neuromorphic method is suggested for transmission of the acquired *in vivo* data to the outside by using a set of *in vivo* polarized electrodes. This set of electrodes transmits the output signal to the tissue and the signal can be picked up by a set of commercially available ECG electrodes. In the proposed method, the need for replacing

elements in implanted devices is obviated. Fig. 2.8 illustrates the general idea of the proposed powering method.

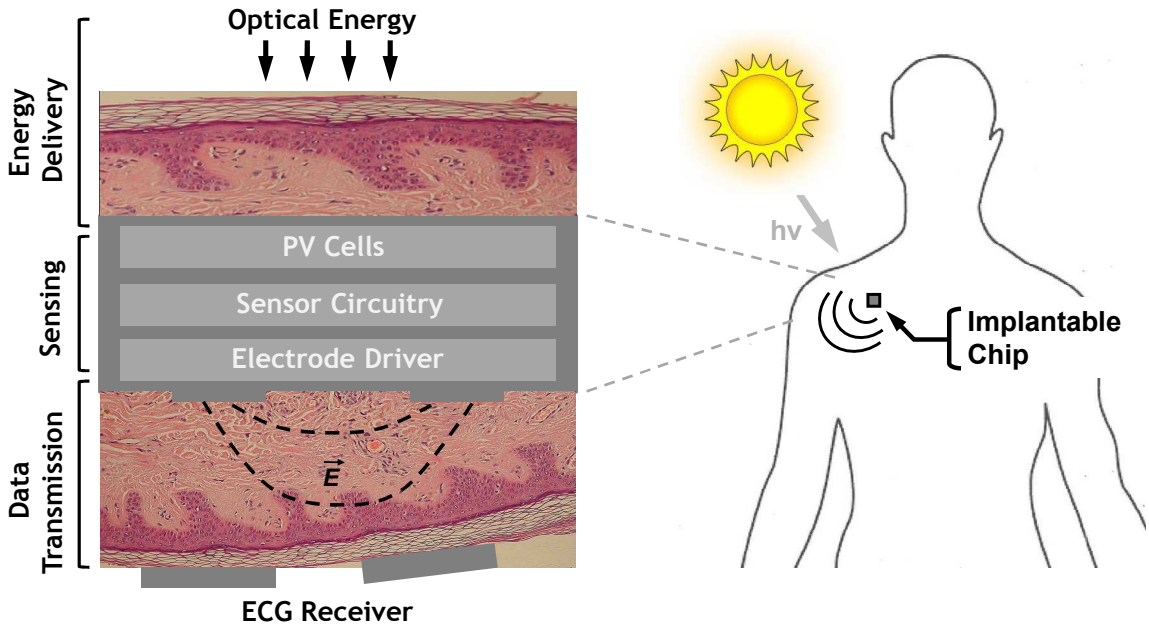

Figure 2.8: Delivering power to implanted devices using CMOS integrated PV cells.

2.5 SUMMARY

Powering implanted devices is a challenging aspect in the design of such systems. Successful techniques for addressing this challenge comprise two major categories. In the first category, power supply is physically connected to the implant and in the second, one form of power harvesting is applied to provide energy.

A new power harvesting method is proposed for implanted devices. This method suggests taking advantage of the light passing through the tissue and converting it to electrical energy using integrated solar cells. In the following chapter, the optical

characteristics of the body tissue are reviewed. The results of this study give an idea of the amount of loss that body introduces to the incoming light.

Chapter 3: Tissue Optical Characteristics

3.1 INTRODUCTION

This chapter reviews the optical characteristics of the tissue and examines whether it is feasible to harvest adequate power using an implanted PV cell. First, some basic optics parameters are reviewed. Subsequently, the optical absorption of a few tissue types is studied based on the previously reported data as well as measurement results.

3.2 DEFINITIONS

The intensity of an incident collimated beam of light changes exponentially when it hits a turbid medium by two mechanisms: absorption and scattering [37]. The intensity (I_0) of an incident beam changes according to Equation (3.1) when it hits a homogeneous and non-scattering medium of thickness x,

$$I(x) = I_0 e^{-\mu_a x}. \tag{3.1}$$

$I(x)$ is the transmitted light intensity and μ_a represents the absorption coefficient (mm^{-1}) of the medium for a given wavelength λ (see Fig. 3.1).

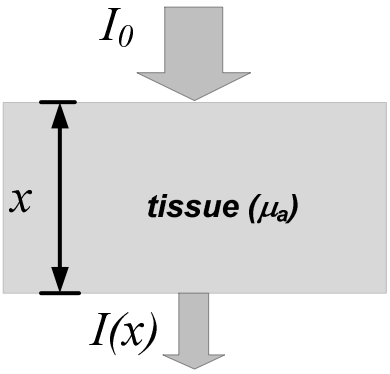

Figure 3.1: Tissue light absorption.

The second mechanism, scattering, is a physical process in which the light interacts with matter and changes its direction. The path of light is not direct in a scattering medium as shown in Fig. 3.2. The scattering is a function of the size of the scattering particles, λ, the refractive indices of the various tissue types, and other variables.

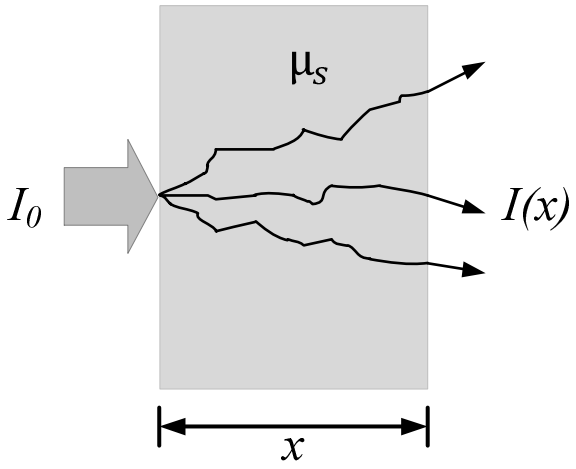

Figure 3.2: Light scattering in a tissue.

The light intensity after passing through the scattering medium, $I(x)$, is generally described by

$$I(x) = I_0 e^{-\mu_s x}, \tag{3.2}$$

where μ_s denotes the scattering coefficient of the medium (mm^{-1}) for a given wavelength λ. "Reduced scattering coefficient," μ'_s, is a parameter that includes the effect of scattering anisotropy and is defined as:

$$\mu'_s = \mu_s(1 - g). \tag{3.3}$$

where g is the coefficient of anisotropy and varies between 0.69 and 0.99 in biological tissues [38]. Therefore, the total transport attenuation coefficient, μ_T, is accordingly

$$\mu_T = \mu'_s + \mu_a = \mu_a + \mu_s(1 - g), \tag{3.4}$$

and,

$$I(x) = I_0 e^{-\mu_T x} = I_0 e^{-(\mu_a + \mu_s(1-g))x}. \tag{3.5}$$

3.3 TISSUE OPTICAL PROPERTIES

There are several contributors to the absorption spectrum of tissue. At ultraviolet, the absorption increases at shorter wavelengths because of the existence of protein, DNA and other molecules. In the infrared the absorption increases at longer wavelengths due to the water content (~75% of the tissue is assumed to be water). In the red to near-infrared (NIR) region, between visible range and IR, the absorption of the tissue is minimal. That is the reason this region is generally referred to as "diagnostic" or "therapeutic" window [39].

It is important to mention here that blood is a strong absorber in the NIR region, and if light strikes a blood vessel, it will be significantly absorbed by blood. Therefore, the local contents of the tissue will indicate the absorption characteristics of the tissue.

Melanosomes of skin contain Melanin, the strongest light absorbing pigment found in animals. Therefore, the volume percentage of the melanosome in the epidermis (the outermost layer of the skin), is of great importance in determining the absorption characteristics of the tissue. [39]

Fig. 3.3 shows the absorption coefficient of water and blood. As discussed the absorption of water shows a dramatic drop in the visible range and NIR region [40]. The absorption coefficient of blood which is shown by molar scale decreases in the NIR region [41].

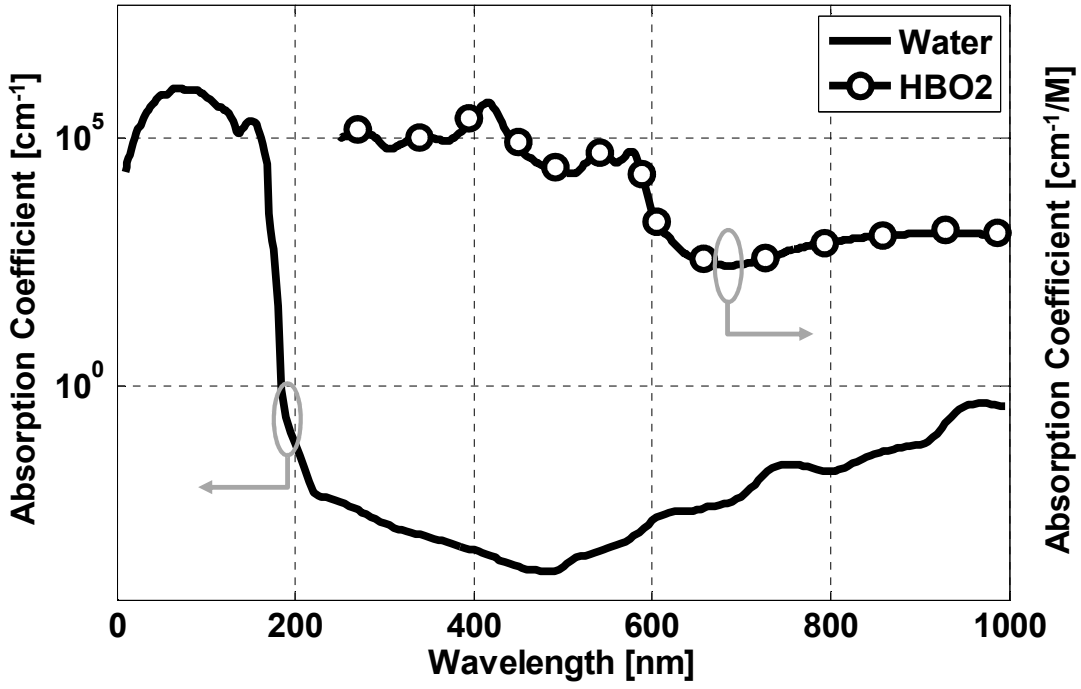

Figure 3.3: Absorption coefficient of water (cm^{-1}) [40] and HbO2 (cm^{-1}/M) [41].

Due to its various structural components, tissue cannot be considered as a homogeneous medium obeying Beer-Lambert Law. However, to simplify the required calculations of light-tissue interactions, a specific tissue type (muscle, liver, skin, fat and etc.) is generally modeled as a homogeneous medium with specific absorption (μ_a) and scattering (μ_s) coefficient. In order to have an estimate of the expected level of absorption in the tissue, two specific tissue types relevant to this work are studied in detail. The presented data is mainly extracted from [42].

3.3.1 Muscle Tissue

According to [43], the optical properties of muscle tissue are not isotropic, which means they are not identical in all directions. The blood volume in resting muscle is very low (0.5 ml/100g) but it is much higher during exercise and it can rise up to 2ml/100g. In literature, the light absorption of *post mortem* bovine muscle at a wavelength of 630 nm is reported to be $\mu_a = 0.15$ mm^{-1} and $\mu_s(1-g) = 0.7$ mm^{-1} [44] and $g = 0.954 \pm 0.016$ [45]. Karagiannes et al report values at the above wavelength of $\mu_a = 0.166$ mm^{-1} and $\mu_s(1-g) = 0.438$ mm^{-1}, and at 1064 nm they report $\mu_a = 0.118$ mm^{-1} and $\mu_s(1-g) = 0.281$ mm^{-1}, which shows scattering decrease as the wavelength gets longer [46]. The optical parameters for human muscle at 515nm are $\mu_a = 1.12 \pm 0.18$ mm^{-1} and $\mu_s = 53 \pm 4.4$ mm^{-1} [47]. Using equation (3.4) ($\mu_T = \mu_a + \mu_s(1-g)$), the optical loss for each case can be calculated.

Reference	Tissue	Wavelength (nm)	Loss (Absorption) (dB/mm)	Loss (Absorption and Scattering) (dB/mm)
[44]	*Post mortem* bovine muscle	630	0.65	3.69
[46]	*Post mortem* bovine muscle	630	0.72	2.62
		1064	0.51	1.73
[47]	Human muscle	515	4.86	235

Table 3.1: Interpretation of absorption and scattering coefficients in muscle

Table 3.1 shows how much optical loss should be expected from muscle. Reference [47] indicates that in human muscle scattering can be very important. In this design, the scattering can limit the acceptance angle of the device. However, the effect of scattering can be minimized by choosing appropriate incidence angle and proper light beam thickness. The reason is that the scattered photons can also contribute to energy harvesting if the cosine of scattering is in an acceptable range for the light beam thickness.

3.3.2 Skin

Skin includes various layers. Epidermis is the top layer and which itself can be divided into few other layers. *Stratum corneum* is the outermost layer with a refractive index of 1.55 [48-50]. This layer consists of highly keratinized dead squamous cells with a high lipid and protein and relatively low water content. It is an extremely scattering and absorbing layer. Its scattering and absorption coefficients for the wavelengths of 254-546

nm are 250 and 10 mm^{-1}, respectively and these values decrease by wavelength. The reported value for g is 0.9 and this number increases slowly with wavelength [51-54].

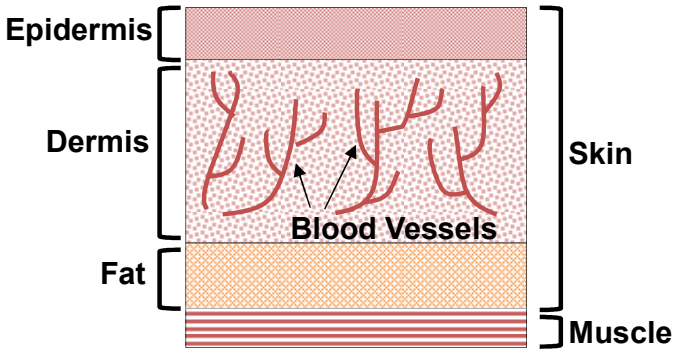

Figure 3.4: Side view of the structure of the skin on top of muscle.

The rest of the epidermis contains layers which have a total thickness of 100 µm and contain most of the skin pigmentation, mostly melanin. These layers have scattering and absorption coefficients which are lower than that of *Stratum corneum* but still higher than other types of tissue. Typical values for absorption and scattering coefficients of these layers in the visible range are $\mu_a = 4\ mm^{-1}$ and $\mu_s = 50\ mm^{-1}$ and the absorption coefficient tends to dramatically increase toward the UV wavelengths. The scattering cosine (g) is reported to have a value of 0.75 and it increases with increasing wavelength [53-55].

The other part of the skin, the dermis, is a much thicker layer, about 2-4 mm and is highly vascularized. The main absorbers in the dermis are blood-borne pigments hemoglobin, β-carotene and bilirubin. Scattering is mostly caused by collagen fibers in the connective tissues in the dermis. The expected absorption and scattering coefficients are around $\mu_a = 0.2{\sim}0.5\ mm^{-1}$, and $\mu_s = 20{\sim}50\ mm^{-1}$, with $g = 0.7{\sim}0.9$ [54],[56]. To get a feeling of how much optical power is attenuated passing through the skin, these results are interpreted in Table 3.2.

Tissue	Wavelength	Loss: Absorption (dB/mm)	Loss: Absorption and Scattering (dB/mm)
Epidermis (*Stratum corneum*)	254-546 (nm)	43	1120
Epidermis (Other layers)	Visible range	17	234
Dermis	Visible range	0.86-2.17	87-219

Table 3.2: Interpretation of absorption and scattering coefficients in skin

The numbers in Table 3.2 show that for a typical sample of skin composed of 12µm *Stratum corneum* and 100µm other layers of Epidermis and 1mm of Dermis at least 3 dB absorption and 123 dB scattering loss can be expected. Similar to what was discussed for muscles, scattering loss may have a minimal effect on this application depending on the characteristics of the light source.

3.4 MEASUREMENTS

Although the optical characteristics of tissue have been measured and reported in the literature, I also did measure the characteristics of the tissue types that I finally used in the sensor. In order to measure the optical loss of these tissues I put the tissue samples (*post mortem* bovine muscle and fat and 1~2 mm thick chicken skin) in a micro-titer plate and put it in a spectrophotometer (TECAN SAFIRE micro-plate reader). The results are shown in Fig. 3.5. As expected, the tissue loss graphs demonstrate a significant drop in

the higher end of the visible range and the near infrared region (i.e., 600nm and up). This is pertinent to the characteristics of water and blood as explained in section 3.3. It can also be observed that the absorption from muscle is about 17 dB/mm in NIR region, which is higher than the reported value in Table 3.1. This might be because of the non-idealities in the measurement conditions. But this result gives a pessimistic estimate of the loss in the specific tissues used in the rest of measurements in this dissertation. The results also confirm that the optical loss in the skin is comparably higher than that of the muscle and fat tissues over the whole spectrum. About 40 dB attenuation is expected when skin layer and 1mm of muscle exist on top of the implanted device.

In addition to the tissue absorption, the reflection and absorption of any clothing that covers the tissue on top of the implanted device shrinks the total number of photons reaching to the device. The level of this attenuation depends on the type and color of the clothing fabric. [57] shows that the light attenuation increases with the number of threads per area unit.

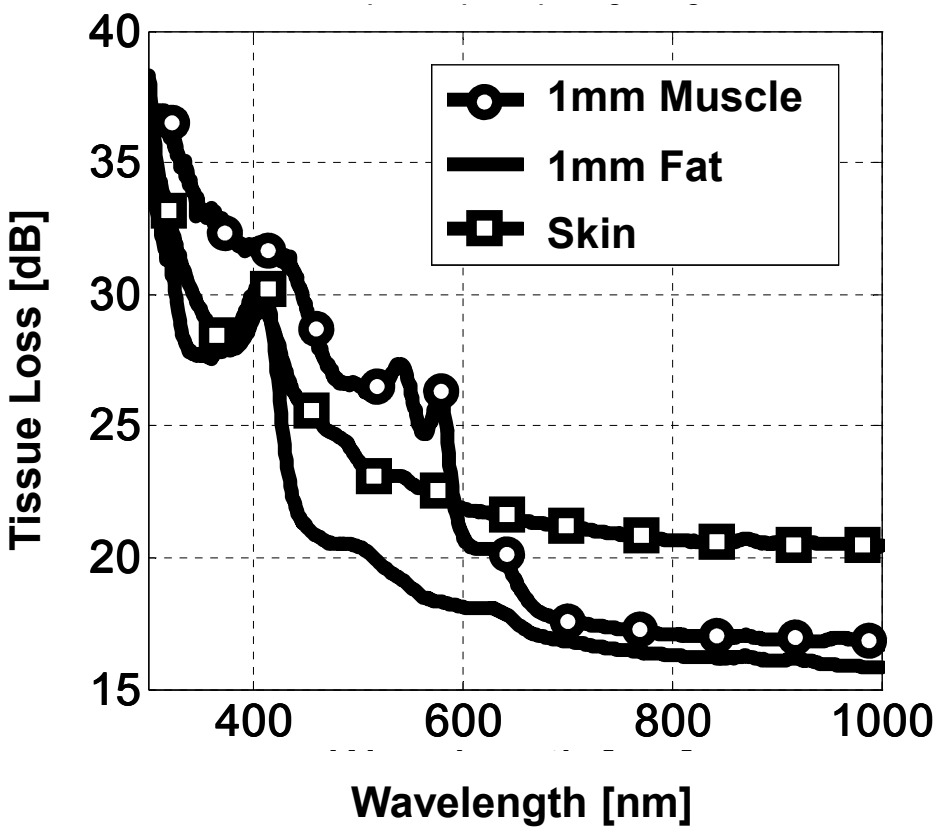

Figure 3.5: The measured optical path loss in tissue.

3.5 SUMMARY

In this chapter, some basic optics parameters were reviewed in order to explain the optical characteristics of the tissue. Subsequently, the optical properties of tissue in general, and two types of tissue in specific, were studied in the visible and NIR range. The expected tissue loss in that range was discussed using the data reported in the literature and with the measurements results. According to these results, around 20 dB loss per mm is expected from different tissue types. The next chapter studies the characteristics of the CMOS integrated PV cells and it will be found out if this amount of loss is tolerable for running implanted devices with CMOS PV cells.

Chapter 4: Power Harvesting Photovoltaic (PV) Cells

4.1 INTRODUCTION

Today, energy harvesting is one of the fastest growing research areas in the analog and mixed-signal IC design field. The main driver behind studying and developing these systems is the need for energy-autonomous VLSI systems with operational life-times much longer than the existing life-time of their batteries, if any. One of the main limitations of energy harvesting elements is the presence of the off-chip (and hence non-integrated) transducer elements (e.g., piezoelectric element or RF coils). In this chapter, a CMOS-compatible and on-chip power harvesting element, which is the photodiode is examined.

4.2 PHOTOVOLTAIC CELLS

A solar cell is a two-terminal device which acts as a diode in the dark and generates photovoltage when light is shined on it. It is usually a planar semiconductor device, the surface of which is treated to reflect as little as possible in the light. In its general use, it has an area around 100's of cm^2 and generates milliamps of current at voltage of around 0.5V.

PV cells can be created using various types of P-N junctions, e.g. PN, PIN, etc., but the most widely used structure for photovoltaics is the P-N homojunction. The choice for the doping of P-type and N-type results in various potential barriers between the regions. The photovoltage formed across the junction grows with the width of the created potential barrier.

When the PN junction is under the illumination, electron-hole pairs are created in the three regions which are quasi neutral P, N, and the depletion region. This generation rate, $G(x)$, which is a function of absorption coefficient of the semiconductor, $\alpha(\lambda)$, decays exponentially with depth in the junction (x) such that

$$G(x) = \alpha(\lambda)F_0 e^{-\alpha(\lambda)x}, \tag{4.1}$$

where F_0 stands for the incident photon flux density. In Fig. 4.1, x_1 and x_2 mark the edges of the depletion region from the surface and x_3 shows the depth of the quasi-neutral P region.

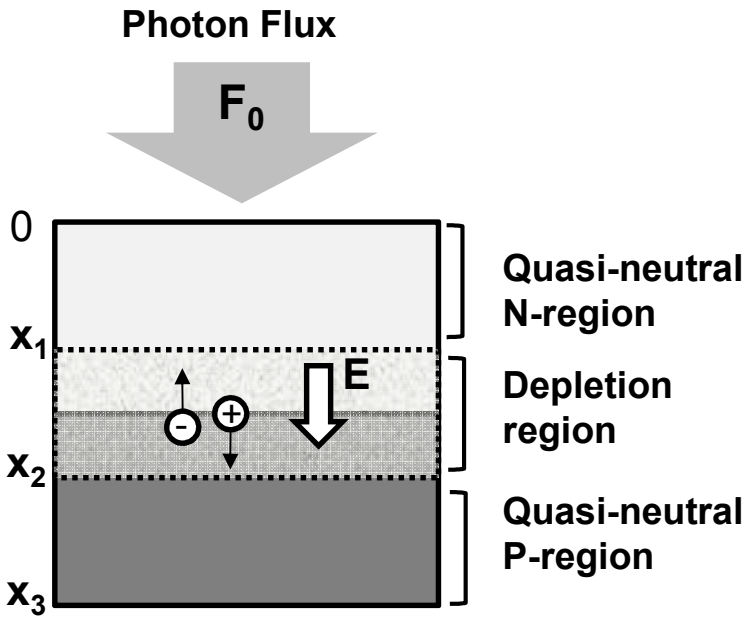

Figure 4.1: P-N junction under illumination.

The generated photocurrent is composed of the drift and diffusion currents from these three regions and is a function of junction parameters such as junction depth and width and F_0.

$$j_{ph} = \frac{qF_0}{\alpha(\lambda)}\left\{\frac{1-e^{-\alpha(\lambda)x_1}}{x_1} - \frac{e^{-\alpha(\lambda)x_2} - e^{-\alpha(\lambda)x_3}}{x_3 - x_2}\right\}. \tag{4.2}$$

In (4.2) j_{ph} is the photocurrent density and q stands for the charge magnitude of an electron. The amount of photocurrent is also a function of the wavelength of the light. Quantum Efficiency (QE), which describes the electrical sensitivity of the device to light, is generally used to demonstrate this dependence. QE expresses the percentage of the photons that produce an electron-hole pair when hitting the surface which becomes

$$QE(\lambda) = \frac{j_{ph}}{qF_0} = \frac{1}{\alpha(\lambda)}\left\{\frac{1-e^{-\alpha(\lambda)x_1}}{x_1} - \frac{e^{-\alpha(\lambda)x_2} - e^{-\alpha(\lambda)x_3}}{x_3 - x_2}\right\}. \tag{4.3}$$

When the junction is under illumination, a voltage is formed across it. This voltage is called "Open Circuit" voltage, V_{OC}, which can be formulated by

$$V_{OC} = \frac{kT}{q}\ln\left(\frac{I_{ph}}{I_s} + 1\right) \cong \frac{kT}{q}\ln\left(\frac{I_{ph}}{I_s}\right), \tag{4.4}$$

where I_s stands for the saturation current in the junction, k is the Boltzman constant and T is the absolute temperature. The first order circuit model of a photovoltaic cell is shown in Fig. 4.2 in which I_{ph} represents the short circuit current under illumination.

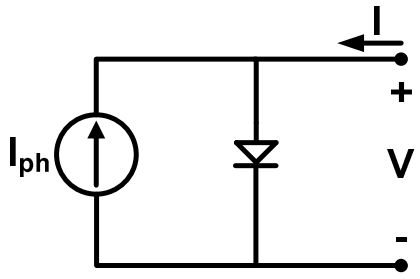

Figure 4.2: Photovoltaic cell first order circuit model.

The I-V characteristic of the PV cell is similar to a simple diode, but the curve is shifted down with I_{ph} as shown in Fig. 4.3.

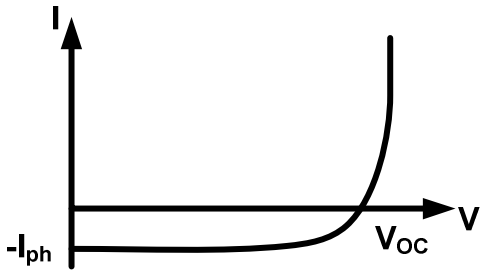

Figure 4.3: I-V curve of a photovoltaic cell.

It is important to realize that a considerable amount of the incident photon flux does not contribute to the total current because of reflection at the surface and recombination inside the material. According to [58] around 30-40 % of the light at visible range gets reflected from the surface of a semiconductor. In order to maximize the current density, different types of treatment such as anti-reflection coating get done on the junction [58].

4.3 CMOS PV CELLS

In standard bulk CMOS processes, there are three types of PN junctions (diodes) that can potentially operate as PV cells. As shown in Fig. 4.4, these devices are $P+/N_{WELL}$, N_{WELL}/P_{SUB}, and $N+/P_{SUB}$ photodiodes.

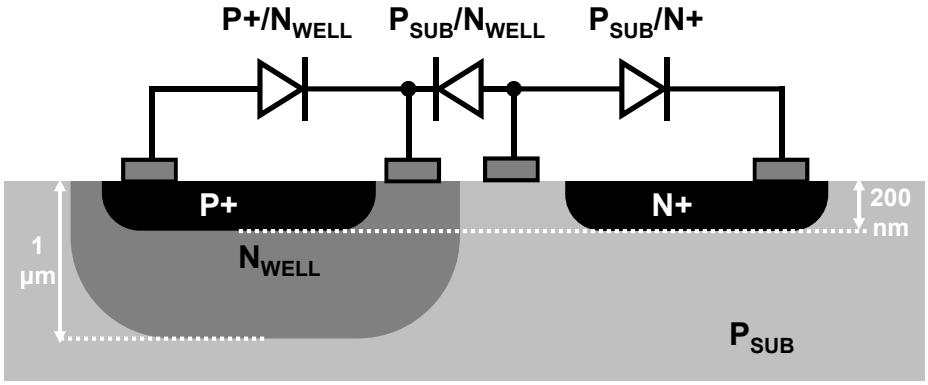

Figure 4.4: Photodiodes available in bulk CMOS processes.

In this project, the cells are designed using a 0.18µm CMOS process from Taiwan Semiconductor Manufacturing Company (TSMC). To make the cells producible in standard bulk CMOS with no post-processing requirement, the available PN junctions should be utilized. Accordingly, a comparison among the available types of diode is necessary to examine and compare the performance of each type under illumination. In this comparison, the important parameters in photo-current generation are calculated using typical numbers for the properties of the junctions listed in Table 4.1.

Parameter		Value
Impurity Concentration	P_{SUB}	10^{15} /cm^3
	P_{WELL}	5×10^{17} /cm^3
	N_{WELL}	10^{18} /cm^3
	N+	10^{20} /cm^3
	P+	10^{20} /cm^3
Dimensions	N+/P_{SUB} junction depth	200 nm
	P+/N_{WELL} junction depth	200 nm
	N_{WELL}/P_{SUB} junction depth	1 μm
Excess carrier lifetimes (at room temperature)	$\tau_{n,p}$ (P_{SUB})	100 μs
	$\tau_{n,p}$ (P_{WELL})	0.55 μs
	$\tau_{n,p}$ (N_{WELL})	0.25 μs
	$\tau_{n,p}$(N+ and P+)	0.8 ns
Diffusion constants (at room temperature)	D_n(P_{SUB})	34.8 cm^2/s
	D_n(P_{WELL})	10 cm^2/s
	D_n(N_{WELL})	7 cm^2/s
	D_n(N+ and P+)	2 cm^2/s
	D_p(P_{SUB})	3 cm^2/s
	D_p(N_{WELL})	2.5 cm^2/s
	D_p(N+ and P+)	1.8 cm^2/s
Diffusion length $\left(\sqrt{D_\tau}\right)$ (at room temperature)	L_n(P_{SUB})	590 μm
	L_n(P_{WELL})	23.5 μm
	L_p(N_{WELL})	7.9 μm
	L_n(N+ and P+)	0.4 μm

	L_p(N+ and P+)	0.38 μm

Table 4.1: Typical doping profile and process parameters for 0.18μm CMOS

Using the typical numbers given in Table 4.1, I calculated the internal QE of the available diodes in the visible spectrum and NIR using equation (4.3). An important point in this calculation is that the recombination of the electron-hole pairs in the depletion and quasi-natural regions is not considered. Therefore, the calculated QE numbers are somewhat optimistic. However, for the purpose of comparison, this is an appropriate approach.

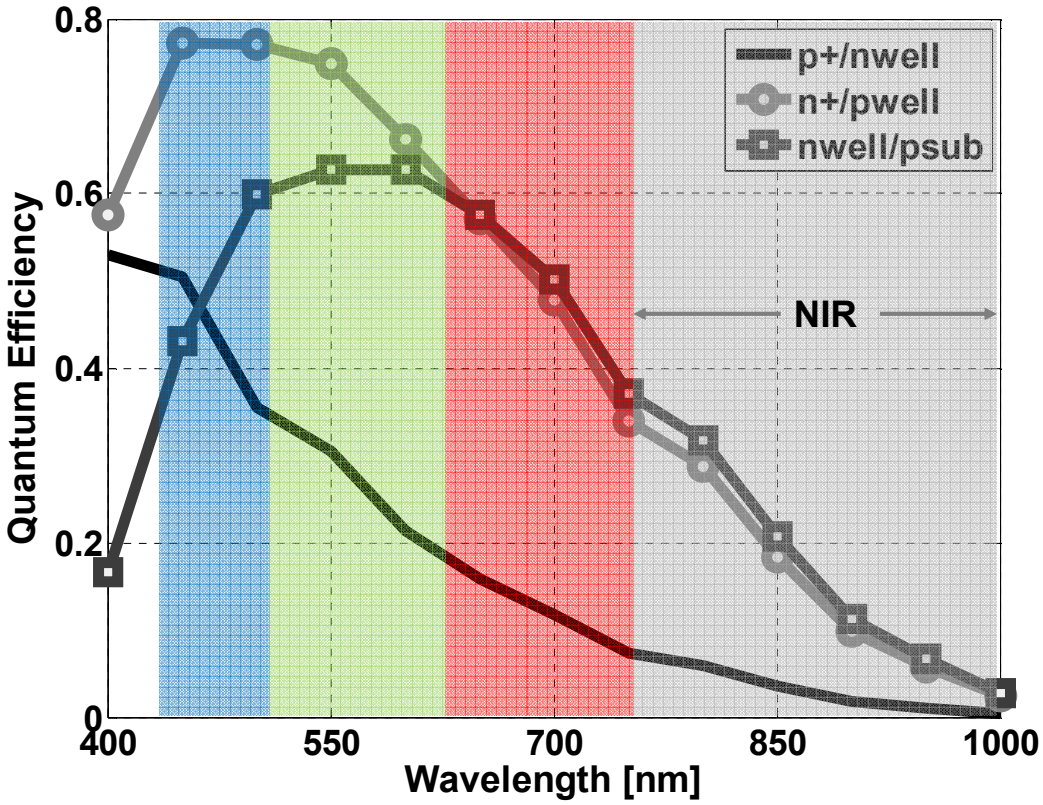

Figure 4.5: Quantum efficiency (QE) of the available diodes in CMOS bulk process (recombination not included).

According to Fig. 4.5 that illustrates QE of the three available diode types, the N_{WELL}/P_{SUB} and $N+/P_{WELL}$ diodes act more efficiently in the NIR region because of their deeper junctions and lower doping concentrations, which create wider depletion regions. However, there is a constraint when these diodes are used as power supplies in a CMOS circuit. Since P_{SUB} of bulk CMOS processes is always connected to the lowest possible voltage (V_{SS}), neither N_{WELL}/P_{SUB} nor $N+/P_{SUB}$ can be used as an on-chip PV cell. The reason being that in the PV mode (i.e., forward bias), the anode of the diode (P_{SUB}) becomes the positive node of the PV cell for these two types of junction, a condition which is not acceptable in bulk CMOS processes. As a result, the only viable device for creating PV cells remains $P+/N_{WELL}$ photodiode.

4.3.2 Design

The $P+/N_{WELL}$ diode designs that are available in the TSMC 180 nm parameterized cell (P-Cell) libraries are not optimal to be used as a PV cell. The reason is that in a PV cell, the area that exposed to light should be maximized while the ready-to-use cells are not optimized for that goal. Therefore, I had to custom-design each cell. To ensure flexibility in using the chip area, I have created a unit cell of 100 µm ×100 µm which meets all the layout design rules of the CMOS fabrication process and for making larger areas of PV cell, I put multiple of these units in parallel.

The first step in designing a $P+/N_{WELL}$ diode is placing P+ and N_{WELL} regions such that minimum area is wasted for meeting the fabrication design rules. On top of the N_{WELL}, N-type diffusion (N+) is placed to realize Ohmic contact to the N_{WELL} terminal. Fig. 4.6 shows the area allocation for the P+, N_{WELL}, and N+ in a PV unit cell.

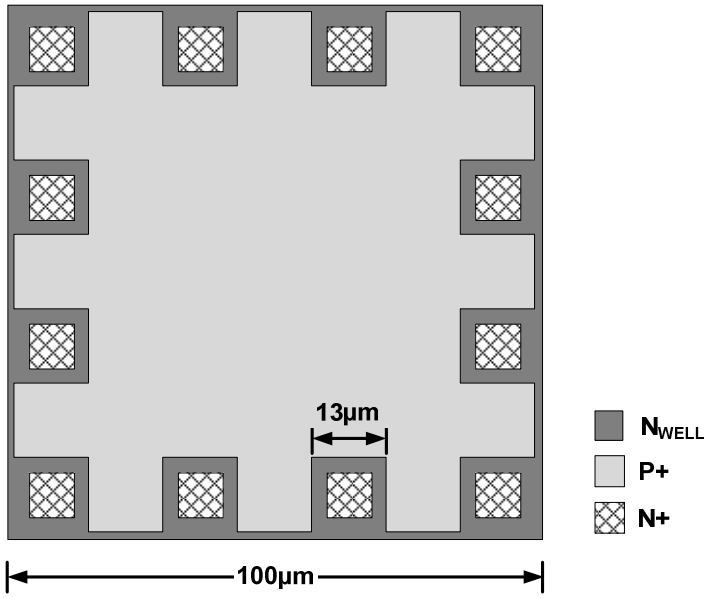

Figure 4.6: The P+ and N_{WELL} diffusion areas in a unit cell.

According to the fabrication rules, the poly silicon layer ("poly") should be filled by the minimum required percentage which is specified by the foundry. Poly layer should not be placed on top of the diffusion layers because it can create unwanted transistors. Fig. 4.7 shows how the design rules requirements are met by placing the poly pieces on top of the N_{WELL} region.

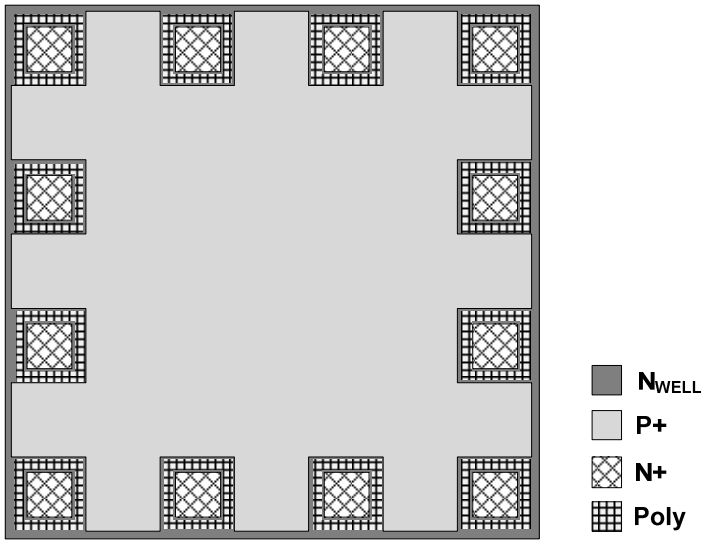

Figure 4.7: Placing the required poly silicon layer in the custom designed diode.

After placing the diffusions, diffusion-metal contacts (CO) and metal pieces should be placed on top of the diffusion layers to make Ohmic contact to the diode terminals and to fill up the area such that the required metal-filling by the fabrication rules are satisfied. These rules also mandate minimum metal coverage in all layers to ensure layer homogeneity and avoid dishing during the chemical mechanical process (CMP). Fig. 4.8 shows how the first metal layer (M_1) is positioned with respect to the diffusion layers.

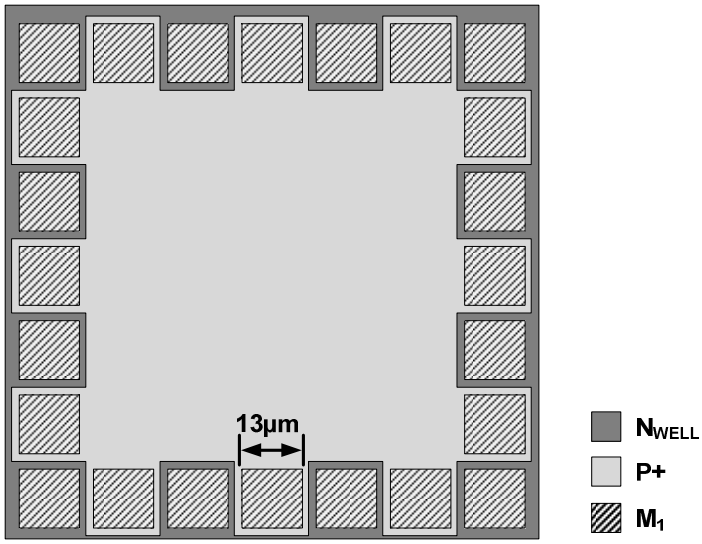

Figure 4.8: Metal placement in the custom designed diode.

The width of the metal layers at each side is approximately 13µm which results in 55% photodiode fill factor for the cell. As shown in Fig. 4.8 the metal portion is also pushed to the periphery to maximize the exposure of the junction to the light and it completely covers the poly silicon and N+ layers.

This 0.18 µm CMOS technology has six available metal layers. The previously discussed metal-fill constraint for the M_1 is required for all six layers. Therefore, all the metal layers (M_2 to M_6) should be filled with the minimum filling requirement. It is preferred to implement the routings of the final chip in the last metal layer (M_6), because it is generally the thickest layer and therefore it has the lowest sheet resistance. Consequently, the contact to the diode terminals should be connected to the top metal layer. As shown in Fig. 4.9, inter-metal contacts (Vias) are inserted between the metal layers and the connection to the top metal layer is implemented.

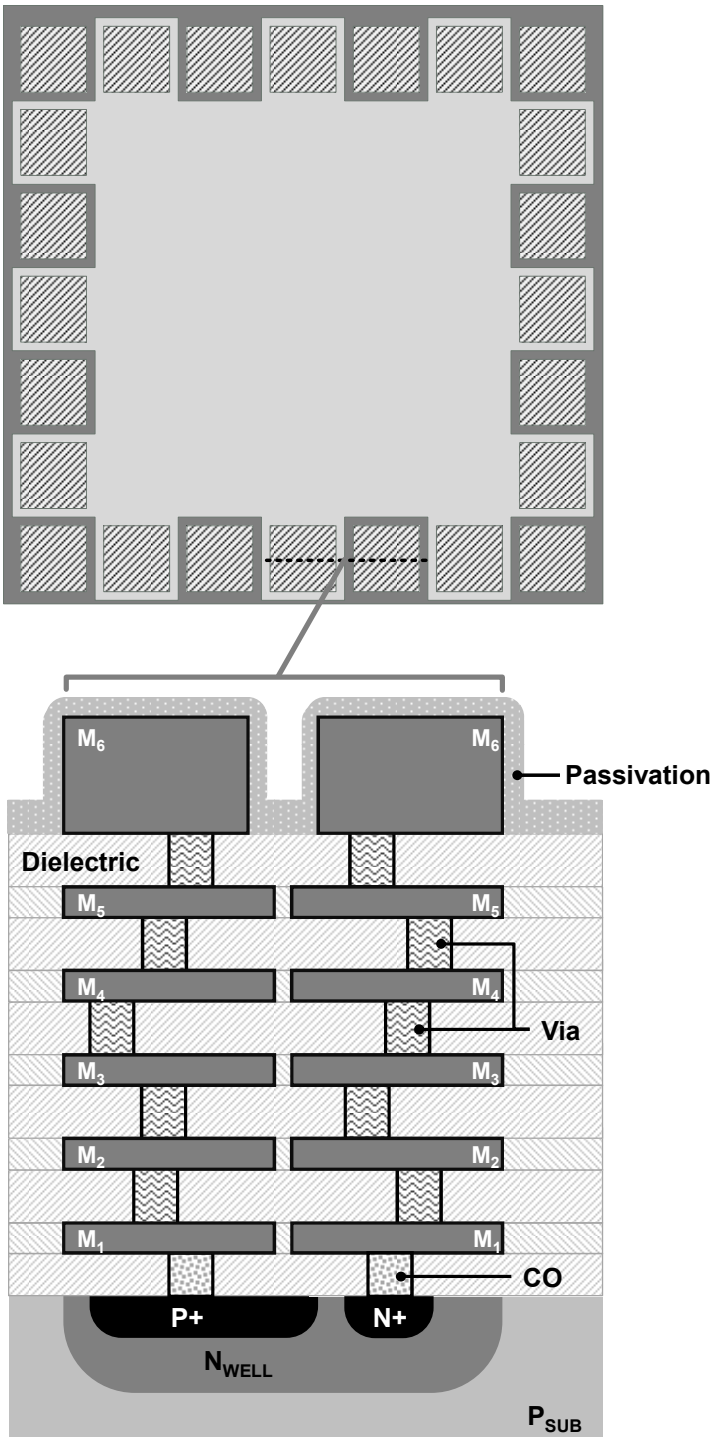

Figure 4.9: Side view of the metal layers.

Larger areas of the diode are made by connecting multiple smaller units in parallel. Fig. 4.10 shows how larger PV cells are formed by connecting these unit cells by metal pads in M_1.

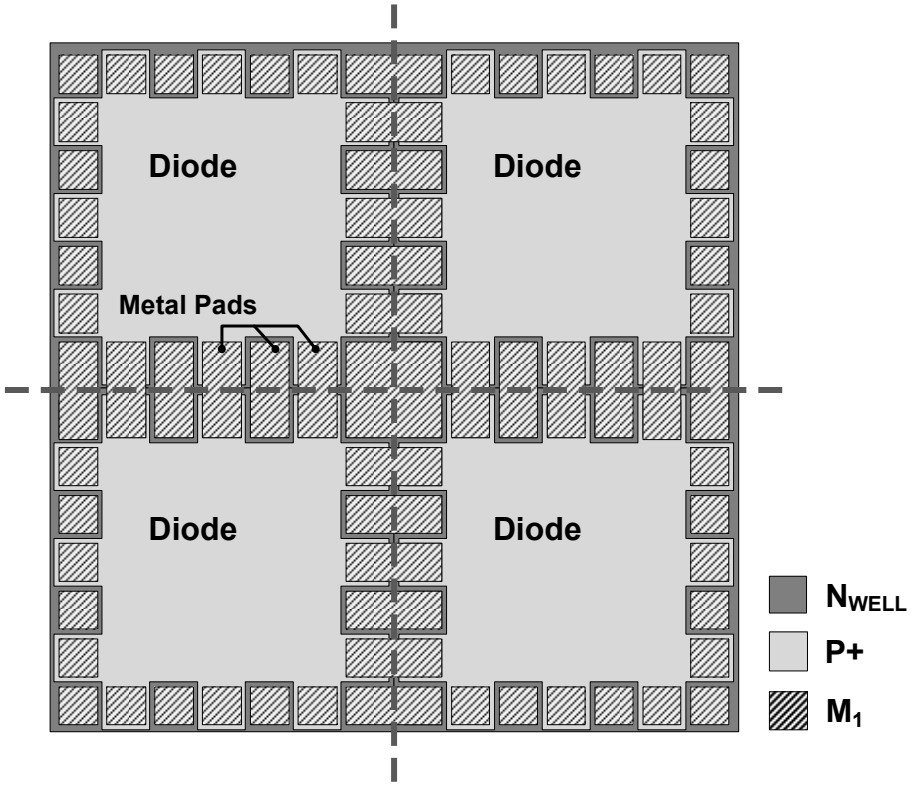

Figure 4.10: Parallel connection of four unit cells with metal pads.

Fig. 4.11 shows the area allocated to the PV cells in the final chip design. Three diodes are present in the final chip; D_1, D_2, and D_3. This will be discussed in detail later.

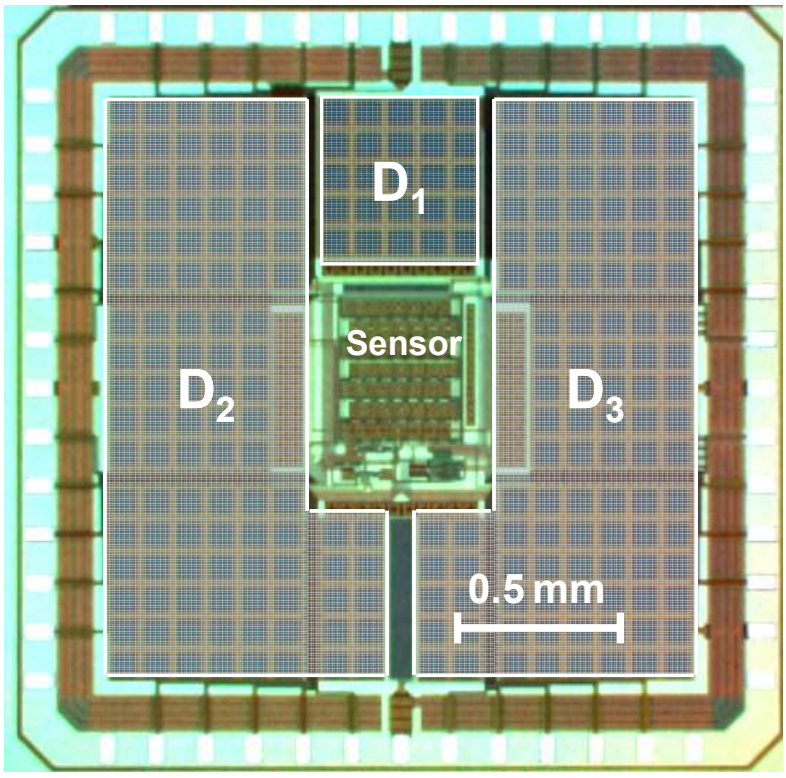

Figure 4.11: Final PV cells in the fabricated chip.

4.3.3 I-V Curve Measurement

The I-V curve of the CMOS P+/N_{WELL} PV cells is identical to the I-V curve of its diode, except that in the PV mode, the whole curve is shifted down by I_{sc}, which is generally referred to as the short-circuit current. Generally speaking, I_{sc} in PV cells is not a constant and is a function of wavelength, λ, the incident photon flux $F_i(\lambda)$, and the photodiode external quantum efficiency $Q_{ex}(\lambda)$, and it can be formulated as

$$I_{sc} = \int_{\lambda=0}^{\infty} F_i(\lambda) Q_{ex}(\lambda) d\lambda. \tag{4.5}$$

The setup shown in Fig. 4.12 has been used to measure the I-V characteristic of the diodes. The diode is tested in two conditions of dark and under solar conditions.

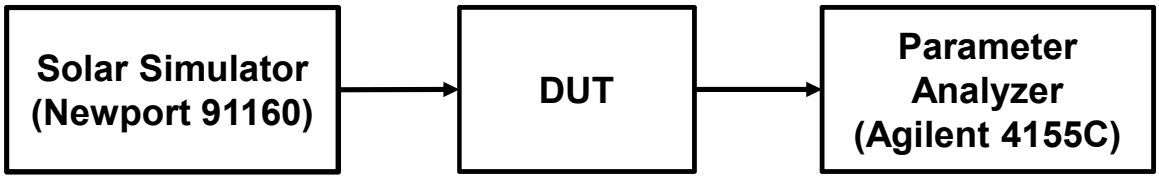

Figure 4.12: Block diagram of the setup for I-V measurement.

The parameter analyzer shown in Fig. 4.12 sweeps the voltage across the diode and measures the current. Solar conditions are emulated using the Solar Simulator (Newport, US). This system uses a 150 W ozone free xenon lamp, and produces a 1.3-inch (33 mm) diameter collimated beam. An AM1.5 air mass filter is added to re-shape the spectral output.

At the surface of the sun, the power density is around 62 MWm^2 [58]. At a point right above earth atmosphere, the power density is reduced to 1353 Wm^{-2}. Light is absorbed and scattered passing through the atmosphere and this also changes the shape of the solar spectrum. The portion of light with wavelengths smaller than 300nm is filtered by atomic and molecular oxygen, ozone, and nitrogen. The infrared portion is mostly absorbed by water and CO_2. Water is responsible for the dips in the spectrum at 900, 1100, 1400 and 1900nm and CO_2 shapes the dips at 1800 and 2600nm. The attenuation by the atmosphere is quantified by a factor named "Air Mass", n_{AM} , which is defined by the following equation:

$$n_{AM} = \frac{\text{optical path length to sun}}{\text{optical path length if sun directly overhead}} = cosec(\gamma_s). \tag{4.6}$$

As shown in Fig. 4.13, γ_s is the angle of elevation of Sun. The Air Mass spectrum with n_{AM} is the extra-terrestrial solar spectrum which is attenuated by n_{AM} thickness of the Earth atmosphere with standard composition and thickness.

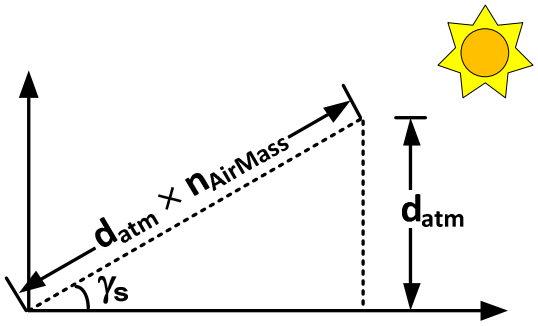

Figure 4.13: Illustration of the atmosphere depth and Sun angle with respect to the observer on Earth.

Air Mass 1.5, or AM1.5 is the standard spectrum for temperature latitudes, and corresponds to the Sun being at the angle of 42°. The solar spectrum must be attenuated to ~900 Wm^{-2}, but for convenience the standard terrestrial solar spectrum is defined as the normalized AM1.5 in a way that the integrated irradiance is 1000 Wm^{-2}. The AM1.5 filtered solar spectrum is shown in Fig. 4.14.

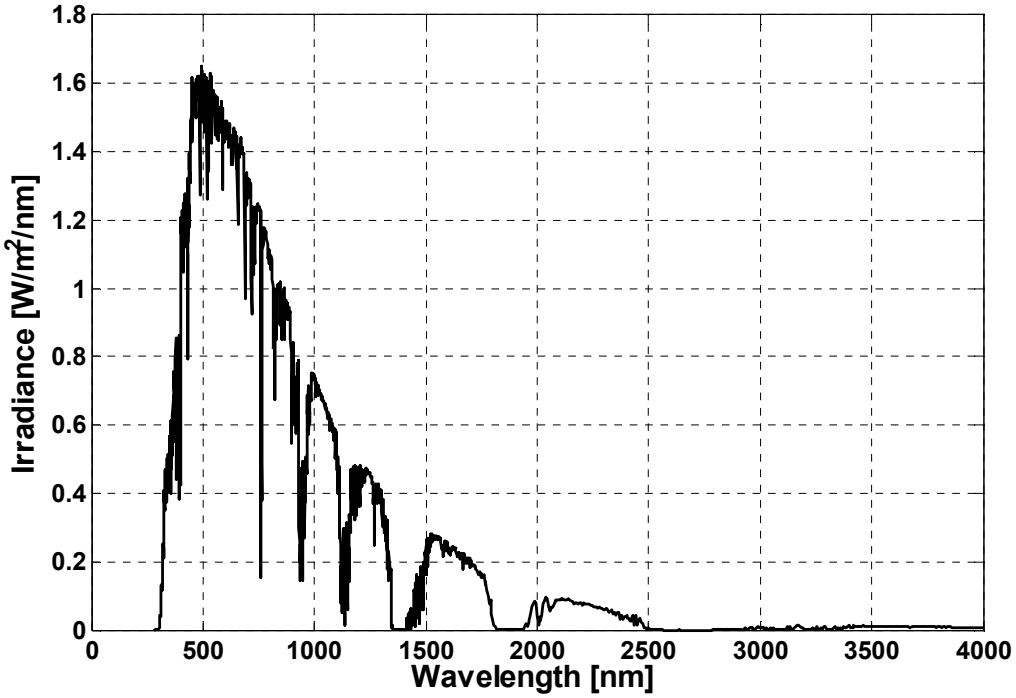

Figure 4.14: ASTM (American Society for Testing and Materials) Global tilt AM 1.5 Solar spectrum irradiance reference [59].

I measured the I-V curve of a $1mm^2$ $P+/N_{WELL}$ diode in two conditions of dark and Solar conditions. The result is shown in Fig. 4.15.

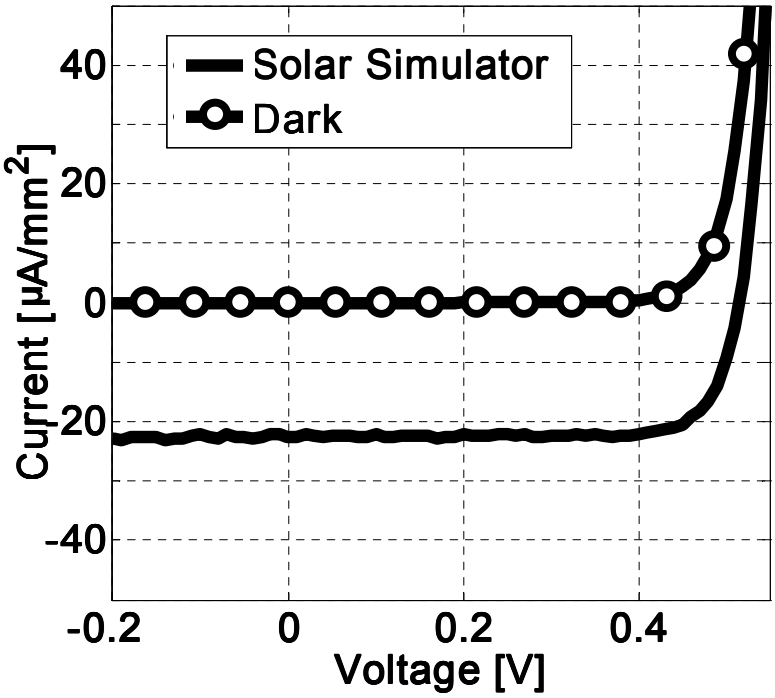

Figure 4.15: 1mm^2 CMOS P+/N$_{WELL}$ PV cell (a) I-V curve, and (b) spectral responsivity.

As it is evident in the measured I-V curve of Fig. 4.15, I_{sc} density in the presence of a solar emulator light source is approximately 22μA/mm^2. When no light is present (*i.e.*, the chip is covered), this current drops to below 0.2nA/mm^2. At bright light, the open-circuit voltage in the PV mode, V_{oc}, is between 0.4V-0.5V. The next sub-sections discuss the PV cell parameters that are extracted from the measured I-V curve.

4.3.3.1 Maximum Available Power

In Fig. 4.16 the available power from the diode is shown under two light conditions. The maximum power density available from the diode, P_m, is measured to be

9.3μW/mm^2 at 1 Sun. The voltage and current density at this point are denoted by V_m and J_m such that

$$P_m = V_m \cdot J_m. \tag{4.7}$$

This level of power can be achieved if the load, R_m, of the PV cell equals the ratio of V_m and I_m, such that

$$R_m = V_m / I_m, \tag{4.8}$$

where, $I_m = J_m \cdot A$.

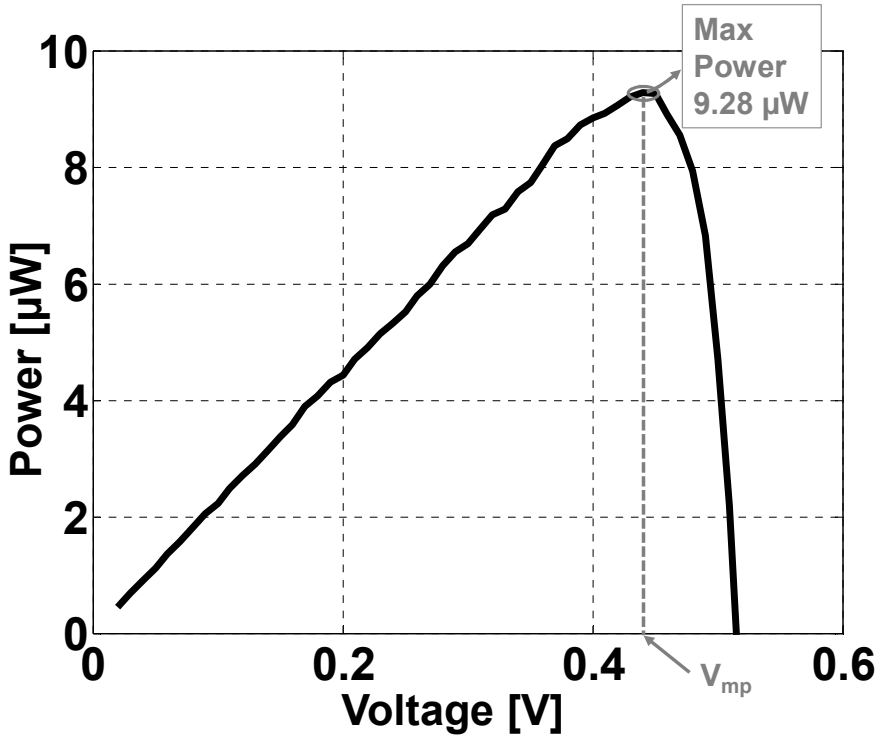

Figure 4.16: Available power from the 1mm^2 P+/N$_{WELL}$ PV cell under sunlight.

4.3.3.2 Power Fill Factor

This parameter demonstrates the ratio between the maximum available power to an ideal power, which is the product of I_{SC} and V_{OC}.

$$FF_p = \frac{J_m V_m}{J_{sc} V_{oc}} = \frac{9.3}{22*0.51} = 83\%. \quad (4.9)$$

In this equation, J_m and V_m show the current density and voltage of the maximum available power point. Comparing this number to the reported fill factors in [58], it is confirmed that the fill factor of this solar cell is in higher range of the available solar cells.

4.3.3.3 Power Efficiency

Another important parameter of solar cells is their efficiency. Efficiency of a solar cell is the ratio between the maximum available power density to the incident light power density. The light power density is 1mW/mm^2 for 1 Sun solar light condition.

$$\eta = \frac{J_{mp} V_{mp}}{P_s} = \frac{9.3}{1000} = 0.93\ \% \quad (4.10)$$

This value is about 1/20 of the typical numbers reported for the non-CMOS solar cells in [58]. This is expected because no chemical/mechanical optimization is performed on the cells to avoid recombination and maximize the light absorption.

4.3.3.4 Characteristic Resistance

Characteristic resistance (R_{CH}) of a solar cell is the ratio between its open circuit voltage to its short circuit current at the maximum available power point. If the load to a solar cell is equivalent to the characteristic resistance, then the solar cell operates at its maximum power point.

$$R_{CH} = \frac{V_{MP}}{I_{MP}} = \frac{0.44}{21.08} = 20.87\ k\Omega \tag{4.11}$$

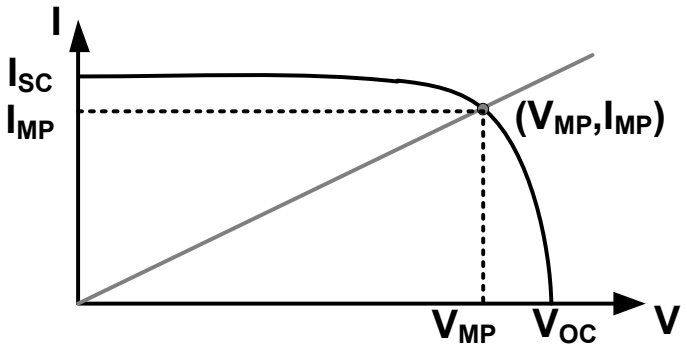

Figure 4.17: The maximum available power point in the IV curve.

4.3.3.5 Parasitic Resistors

Second order modeling of a PV cell takes into account the series and shunt parasitic resistances. This model is shown in Fig. 4.18. A photovoltaic cell is modeled as a diode in parallel with a current source. R_S is usually a function of the cell material and R_{SH} arises from the leakage of the current through the device edges and the cell contacts [58].

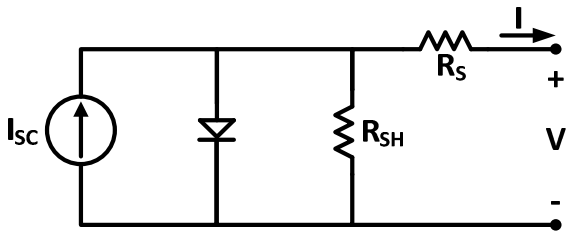

Figure 4.18: A second order circuit model for PV cells including the parasitic resistors.

Series and shunt resistances can be estimated using the I-V curve. As shown in Fig. 4.19 the series and shunt parasitic resistances affect the ideal I-V curve of a diode.

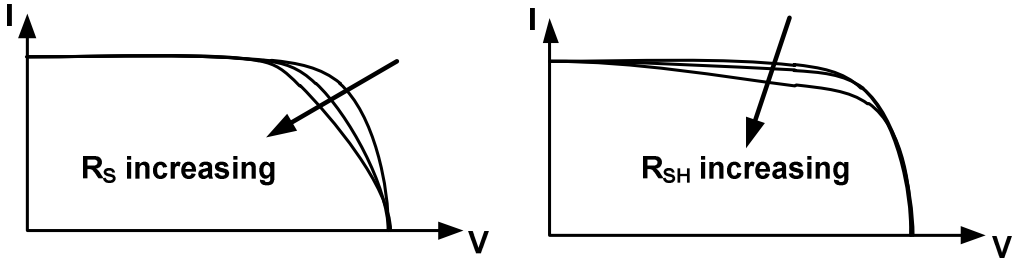

Figure 4.19: Effects of the parasitic resistors on the I-V curve [58].

In dark situations, when the parasitic resistors are not taken into consideration, the current can be written as a function of the voltage at its terminal by Shokley Diode model:

$$I = I_s\left[1 - e^{V/nV_T}\right]. \tag{4.12}$$

In (4.12) I_s denotes the saturation current and n stands for the ideality factor. On the other hand, when the effects of the parasitic resistors are included, the equation has the following form:

$$I = I_s\left[1 - e^{(R_S I+V)/nV_T}\right] - \frac{R_S I+V}{R_{SH}}. \tag{4.13}$$

It is not easy to find a closed form solution for the values of the parasitic resistors and these values are usually estimated by numerical methods. I have estimated the values of the parasitic resistors by fitting the I-V data of the diode to the model equation (4.13). The results show that R_S and R_{SH} are approximately equivalent to 11.22 Ωcm^2 and 745 k Ωcm^2 respectively. The ideality factor (n) is also estimated to be 1.44 from the curve fitting.

These parasitic resistors affect the fill factor of the diode

$$FF_S = FF_0(1 - \frac{R_S}{R_{CH}}) \tag{4.14}$$

$$FF_{SH} = FF_0(1 - \frac{R_{CH}}{R_{SH}}) \tag{4.15}$$

FF_S and FF_{SH} show the effect of the series and shunt resistances on the fill factor, while FF_0 shows an ideal fill factor that is not affected by shunt and series resistances. From the estimations in the above equations the effect of the parasitic resistances on the fill factor can be observed below.

$$\frac{FF_S}{FF_0} = 1 - \frac{R_S}{R_{CH}} \cong 1$$

$$\frac{FF_{SH}}{FF_0} = 1 - \frac{R_{CH}}{R_{SH}} = 0.97$$

Considering these results, the series and shunt resistances in the implemented diode do not deteriorate the fill factor heavily. Table 4.2 summarizes the measured parameters of the $1mm^2$ $P+/N_{WELL}$ diode.

Parameter	Definition	Value
Diode type	Type of junction	$P+/N_{WELL}$
Size	Diode area	1 mm^2
Optical FF	Ratio of the area exposed to light to the whole area	55%
I_{SC} Dark	Short circuit current at the dark condition	0.2 nA/mm^2
I_{SC} Solar	Short circuit current at the Solar light condition	22 $\mu A/mm^2$
V_{OC}	Open circuit voltage	0.51V
$P_{max,ideal}$	$I_{SC} \times V_{OC}$	11.22 μW
P_{max}	Maximum power available under Solar condition	9.28 μW
η	The ratio between P_{max} and the light source power	0.93%
Power FF	$P_{max}/P_{max,ideal}$	83%
R_{CH}	V_{OC}/I_{SC}	20.87 kΩ
R_S	Series parasitic resistance	11.22 Ωcm^2
R_{SH}	Shunt parasitic resistance	745 $k\Omega cm^2$
n	Diode ideality factor	1.44

Table 4.2: Summary of the measured parameters of the $P+/N_{WELL}$ diode.

4.3.4 Responsivity Measurement

In a photo-detector, responsivity shows the electrical output per optical input. In my experiments I have measured the short circuit current of the diodes vs. the input optical power for a range of wavelengths including the visible range and a portion of Near Infrared. The block-diagram of the setup used for this measurement is shown in Fig. 4.20. In this measurement, the monochromator sweeps the spectrum and generates light

with a known power level, and the background light is cancelled from the optical input to the diode using the chopper.

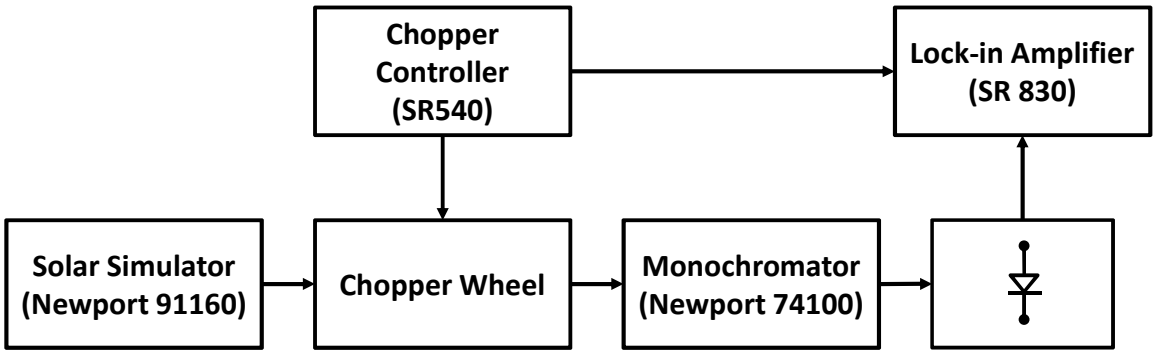

Figure 4.20: Block diagram of the setup for measurement of responsivity.

In Fig. 4.21, the measured responsivity of the 1mm^2 P+/N_{WELL} cell is shown at zero bias voltage. It is important to mention that this data can also be used to compute $Q_{ex}(\lambda)$ since responsivity is essentially $hcQ_{ex}(\lambda)/\lambda$ where h and c being Planck's constant and speed of light, respectively. The external quantum efficiency of this diode is equal to 1.6%.

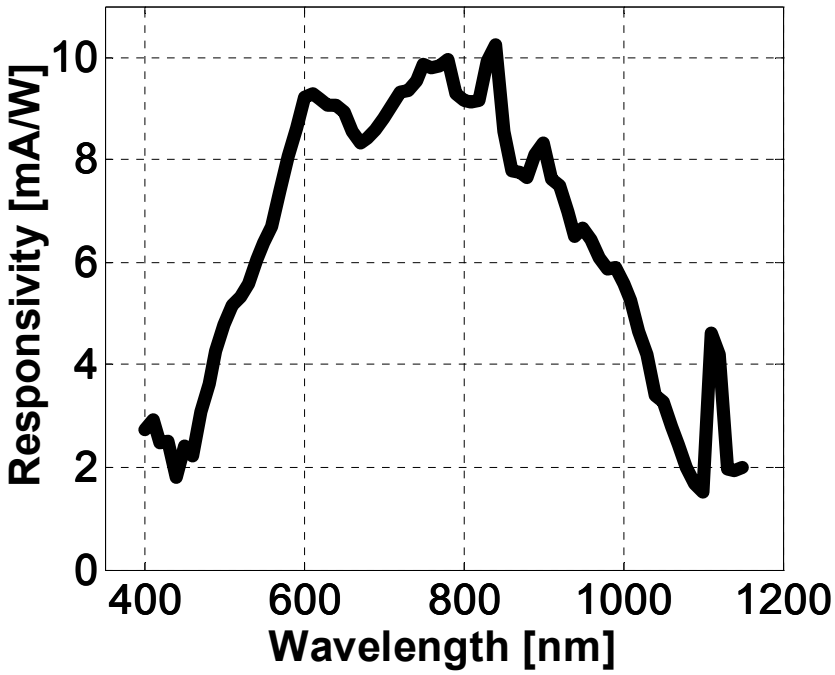

Figure 4.21: Spectral responsivity of the 1mm^2 CMOS P+/N_{WELL} PV cell.

4.4 A COMPARISON OF POWERING METHODS

In order to understand where this method stands compared to the other methods, a comparison is provided between their characteristics in terms of size, tissue loss, and ease of use.

4.4.1 Tissue Loss

All the methods introduced in Chapter 2 can be used to power any system outside of the body. However, to use this technology for implanted devices, one needs to have an understanding of which method is efficient when used in an implant. Therefore, I compare the power loss caused by tissue in the harvesting methods (see Table 4.3).

Application	Region	Tissue	Loss	Reference
Inductive Coupling	1 MHz	Muscle	Negligible	[60]
RF	400 MHz	Tissue	10 dB/cm	[20]
	2.4 GHz	Muscle	<20 dB/cm	[19]
Optical	515 nm	Human Muscle	5 dB/mm*	[43]
	633 nm	Aorta Adventitia	2.5 dB/mm	
	633 nm	Aorta Media	1 dB/mm	
	750 nm	Liver	2.6 dB/mm	
	546 nm	Skin Epidermis	43 dB/mm	
	380 nm	Skin Dermis	2.15 dB/mm	
	750 nm	Skin Dermis	0.86 dB/mm	

Table 4.3: A comparison between the tissue loss in three types of powering.

It can be observed that tissue loss in the near field inductive coupling method is negligible, while at RF frequencies the loss in the tissue is considerable. Optical tissue loss is the highest tissue loss among these methods.

4.4.2 MRI Compatibility

In the two methods introduced in 2.2.1 and 2.2.2 (near-field and far-field coupling,) a receiving element which is usually a loop or a coil is needed in the implant. According to [61] an object or device can be “MRI Safe” if it does not introduce any risk

to the patient but may affect the quality of the diagnostic information; and it is "MRI Compatible" if it is "MRI Safe" and it does not affect the quality of the diagnostic information nor the environment affects the operation of the device. Regardless of the frequency used, the presence of a relatively large coil or antenna is inevitable in both methods. It is widely known that larger coils (up to the order of the wavelength which is very large comparable to the size of the chip), are capable of delivering higher power. This is a fundamental disadvantage of this type of power delivery which also makes the implanted devices unsafe in MRI machines.

There is no need to use coils for this new method, therefore, the device does not present any risk to the patient. Magnetic Resonance (MR) environments do not have an effect on the functionality of this powering method and on the other hand, silicon does not cause artifacts on the diagnostic images of the MRI machine. Therefore, depending on the MR environment and the amount of metal that is used in the structure of such a device, it can be an MRI compatible. In order to ensure the MRI compatibility of the method, one needs to investigate the exact requirements of a particular MR environment and the characteristics of the final device more precisely.

4.4.3 Power Density

In order to compare different powering methods, a figure of merit can be defined which states the available power density for each powering method. For example, the batteries used in [11] provide about $10\mu W/mm^3$ for over a year, while in [1] this number is $1.81\mu W/mm^3$.

In the power harvesting methods (near-field and far-field coupling) discussed in Chapter 2, it is more convenient to report this figure of merit by the available power per

area due to the shape of the final device. In [26] and [29] the density of harvested power in the receivers are 1696 $\mu W/mm^2$ and 192.68 $\mu W/mm^2$ respectively. [32] and [33] which perform power harvesting through far-field radiation report 3660 and 44.44 $\mu W/mm^2$ power densities at the receiver. Although in these two methods, harvested power density is a function of the power radiated by TX, they show how much power is typically available in these methods for implanted devices.

Measurements of the PV cell shown in Fig. 4.16, demonstrate that the harvested power density in the designed solar cell is 9.28 $\mu W/mm^2$ under solar light condition. This number will be attenuated to approximately 0.1 $\mu W/mm^2$ under a 2mm-thick tissue slab.

4.4.4 Overall Comparison

Table 4.4 shows a comparison among the powering methods from various aspects. The power density for PV method is reported for the solar light condition, i.e. $1kW/m^2$ light intensity including 40 dB optical tissue loss.

Feature	Wires	Battery	Inductive Coupling	RF	PV
Minimum size	NA	1-10 cm^3	1-10 cm^2	1-5 cm^2	1 mm^2
Tissue loss	NA	NA	Negligible	2 dB/mm	20 dB/mm
Ease of use	Very Hard	Annual Replacement	Easy	Easy	Easy
Hazards	Infection	Leakage	No Hazard	No Hazard	No Hazard
External source	Power Supply	Replacement	Transmitter	Transmitter	Freely Available
MRI compatibility	Incompatible	Generally Incompatible	Incompatible	Generally Incompatible	Compatible
Power Density	Unlimited	10 $\mu W/mm^3$	0.8 mW/mm^2	0.6 mW/mm^2	0.1 $\mu W/mm^{2*}$

Table 4.4: Overall comparison of the old and proposed methods of powering for implanted devices.

In general, PV cells suggest an easy-to-use method for powering implants which can be implemented in small sizes. The energy supply can be freely available but with the cost of having larger levels of tissue loss compared to the other techniques. It does not introduce any hazard to the patient and can be MRI compatible. This method can totally be considered an appropriate candidate for powering ultra-low power implantable devices.

4.5 STACKING PV CELLS

In Chapter 3, it was observed that the maximum available voltage level from a CMOS PV cell is equivalent to the open-circuit voltage which is limited to 0.5 V. This

voltage level is acceptable for low-power applications. However, higher levels of voltage are desired in order to cover a broader range of applications. In this research, the $P+/N_{WELL}$ diodes have been used as the most viable option in the CMOS 0.18µm technology (see Fig. 4.22). I_P denotes the short circuit current of the parasitic diodes under illumination.

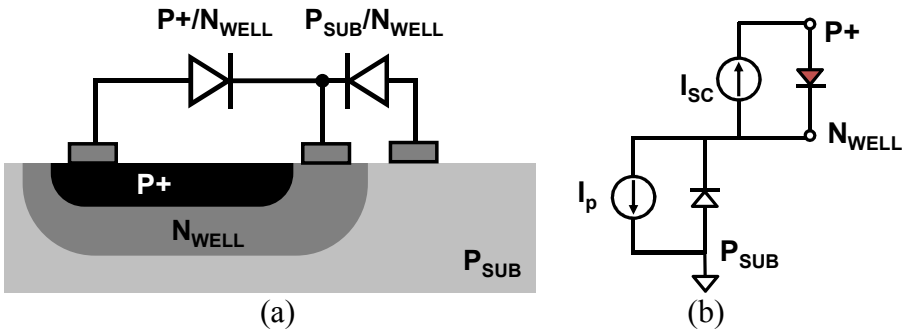

Figure 4.22: (a) Cross sectional and (b) schematic view of $P+/N_{WELL}$ diode and the parasitic junctions.

To achieve higher levels of voltage, the most obvious solution is putting the diodes in series. With a closer look at the design, it becomes clear that under illumination, the P_{SUB}/N_{WELL} parasitic diodes, in photovoltaic mode and do not allow the N_{WELL} terminals to reach a voltage higher than -0.5V (See Fig. 4.15). Although the P_{SUB}/N_{WELL} diode is deeper inside the device and a decrease in light intensity might be expected at this junction, but the penetration depth of the light in silicon at the visible range and NIR region is in a level that it does not prevent the photocurrent generation in the parasitic diodes. As discussed in Section 4.3, the QE of the parasitic diode is higher than $P+/N_{WELL}$ diode through the spectrum.

The parasitic diode *i.e.,* P_{SUB}/N_{WELL} does not affect the functionality of the single diode because the N_{WELL} and P_{SUB} terminals are connected in that case. This encourages

farther exploration of stacking PN junctions. In Fig. 4.23, the series connection of three P+/N_{WELL} diodes is illustrated.

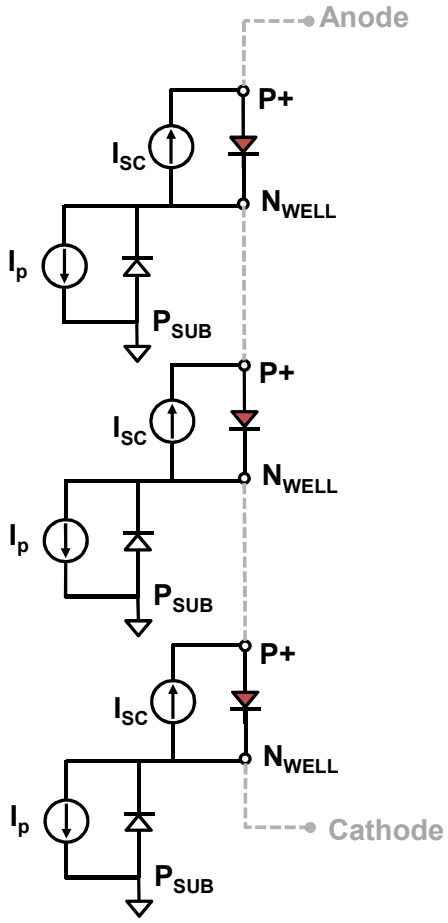

Figure 4.23: Series connection of P+/N_{WELL} diodes.

As explained in Section 4.3.1, other PN junctions are not suitable to be used as the voltage supply in a bulk CMOS process because their anode contact (P_{SUB}) is going to be directly connected to the lowest possible voltage (V_{SS}). Only in a Silicon-On-Insulator (SOI) technology, reaching an isolated PN junction from substrate seems promising; but in the non-SOI technologies, the only possible option would be the use of deep N_{WELL} (DNW) layer to isolate the N+/P_{WELL} diodes. To investigate feasibility of this, the effect

of the parasitic diodes in this case needs to be examined. Fig. 4.24 shows the desired PN junction and the relevant parasitic diodes. I_{P1} and I_{P2} denote the short circuit currents of DNW/P_{WELL} and DNW/P_{SUB} under illumination, respectively.

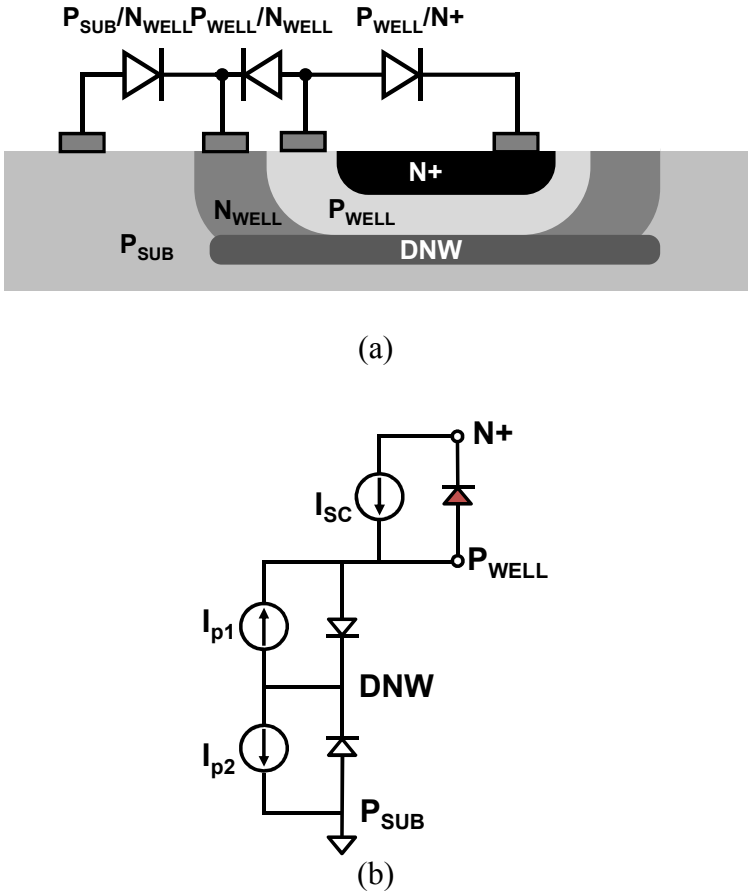

Figure 4.24: (a) Cross sectional and (b) schematic view of N+/P_{WELL} diode and the parasitic junctions.

Because of the larger areas of P_{WELL}/DNW and DNW/P_{SUB}, and their wider depletion regions, a higher amount of photocurrent than the main diode (N+/P_{WELL}) is expected under illumination. Ideally, the DNW contact should be biased at the highest voltage possible to keep the P_{WELL}/DNW diode reverse biased. The highest voltage level

is the P_{WELL} of the top device in the stack, but simulation results show it is not feasible to connect this terminal to all of the DNW contacts as they pull down the P_{WELL} voltage. Therefore, I propose stacking the diodes according to the design shown in Fig. 4.25.

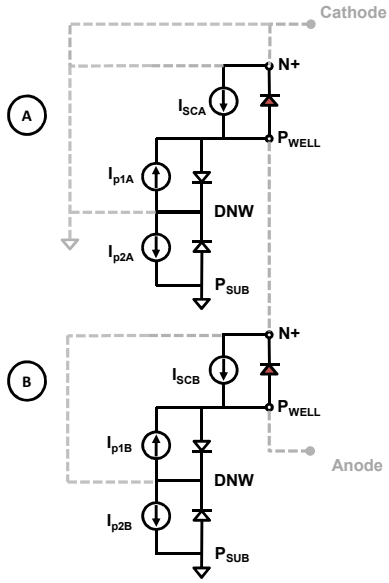

Figure 4.25: The proposed connections for the stack of two N+/P_{WELL} diodes.

At the bottom diode (device A), the N+ and DNW and P_{SUB} can be simply connected to each other, since the P_{WELL} needs to maintain only one V_{OC} and the fact that DNW is connected to ground, does not affect it. I connected the Deep N_{WELL} (DNW) to the N+ connection at the top diode (device B) to keep the DNW/P_{SUB} diode reverse-biased.

Measuring the short circuit current of the N+/P_{WELL} diodes (I_{SC}) while their DNW, N+ , and P_{SUB} are connected (shown in Fig. 4.26) will result in measuring 320 nA for the 0.01mm^2 and 39.4 μA for the 1.28 mm^2 size diodes.

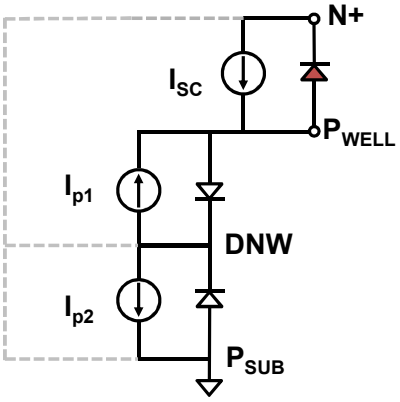

Figure 4.26: Tying N+ and DNW to P_{SUB} for I_{SC} measurement.

Simulation of the design in Fig. 4.25, shows that it is not possible to reach higher voltage levels in the stack of equal-sized diodes. I implemented a stack of two diodes with the areas of 1.28 and 0.01 mm^2. The smaller sized diode (device B) will be stacked on top of the larger diode (device A). Fig. 4.27 shows the I-V curve of the stack.

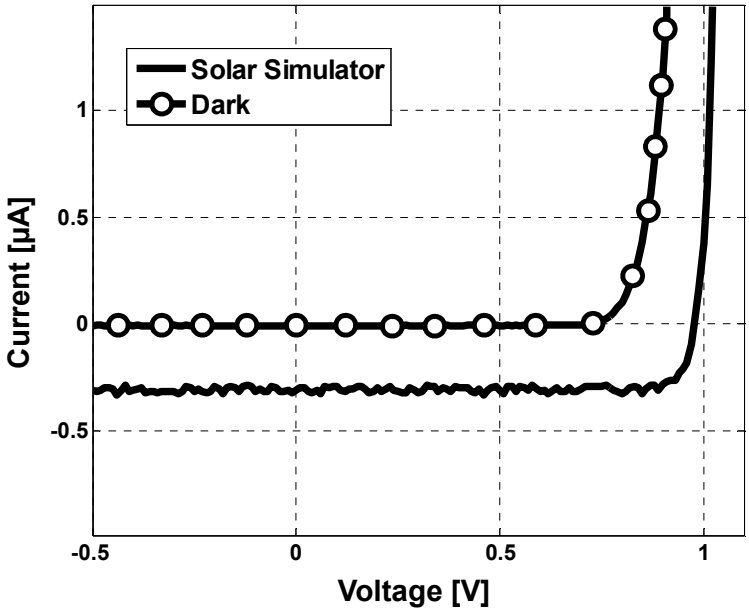

Figure 4.27: The IV curve of the combined diode of Fig. 4.25.

It is evident that in this case, a combined diode is formed with open circuit voltage of around 1V and short circuit current of 320nA, which is equivalent to the short circuit current of the smaller diode. It is obvious that in the series combination of PV cells, the final I_{SC} will be equivalent to the smallest I_{SC} in the stack.

It should be noted that in the stacking of these devices, depending on the structure of the stack and the connections between the regions, the possibility of forming parasitic bipolar junction transistor exists. These parasitic devices add to the leakage of the current and make it harder to reach to higher levels of voltage. As an example Fig. 4.28 illustrates formation of a parasitic bipolar *npn* transistor (Q) between two N+/P_{WELL} diodes on top of DNW layer. Under illumination, voltage difference is created across the P_{SUB}/DNW diode. This might not cause a problem if the substrate terminal is ideally tied to the lowest voltage of the circuit but since the resistance of the substrate is usually assumed to be finite, P_{SUB} may pick up a higher voltage than the DNW regions of one of these diodes. In that case, Q turns on and if the N+ and DNW of each diode are connected as proposed in Fig. 4.25 the cathodes of two diodes connect and this prohibits stacking of the diodes.

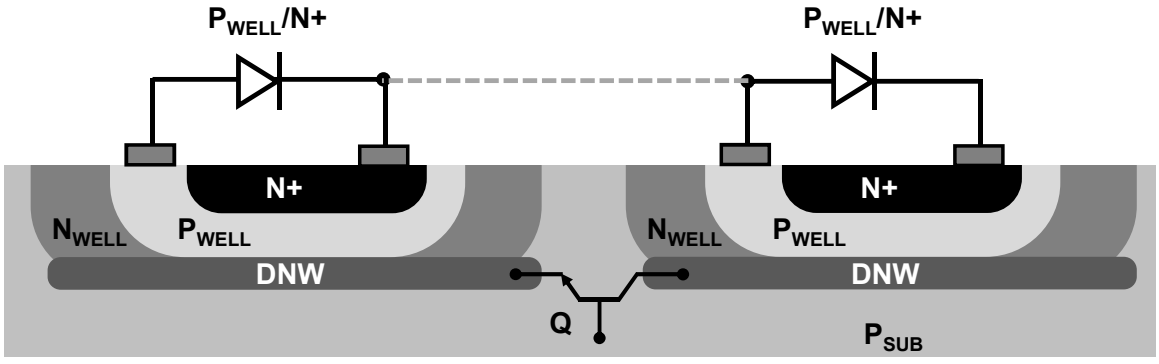

Figure 4.28: Formation of parasitic bipolar transistors between two P+/N_{WELL} diodes when stacking

4.6 SUMMARY

This chapter studied the available diodes in the bulk CMOS process and investigated their capacities to be used as PV cells to power up CMOS devices in general and implanted devices specifically. It is clear now that under sunlight μW's of power from mm^2 size areas of PV cell can be harvested. Including the results of Chapter 3 measurements generation of 100's of nW from a $1mm^2$ sized P+/NWELL PV cell put under 2-3mm thick animal tissue is expected. These results are verified through implementing a prototype device in CMOS 0.18μm TSMC process.

Chapter 5: CMOS Power Delivery Device Design

I designed and fabricated an implantable sensor in CMOS 0.18µm to verify the possibility of powering implanted devices by optical power harvesting through the tissue. This chapter explains the details of the circuit blocks in the fabricated chip and the challenges faced in the design of such circuits.

5.1 Introduction

The sensor high level architecture is shown in Fig. 5.1. The idea is to design a sensor that can measure the value of an unknown impedance indicating an environmental variable and send the data to outside across the tissue. All of these circuit blocks should be run solely by the PV cells (discussed in Chapter 4). "Sensor and Reference" carry out the job of transducing the unknown impedance to an electrical signal and "Electrode Driver" transmits the signal to a pair of "*in vivo* Electrodes".

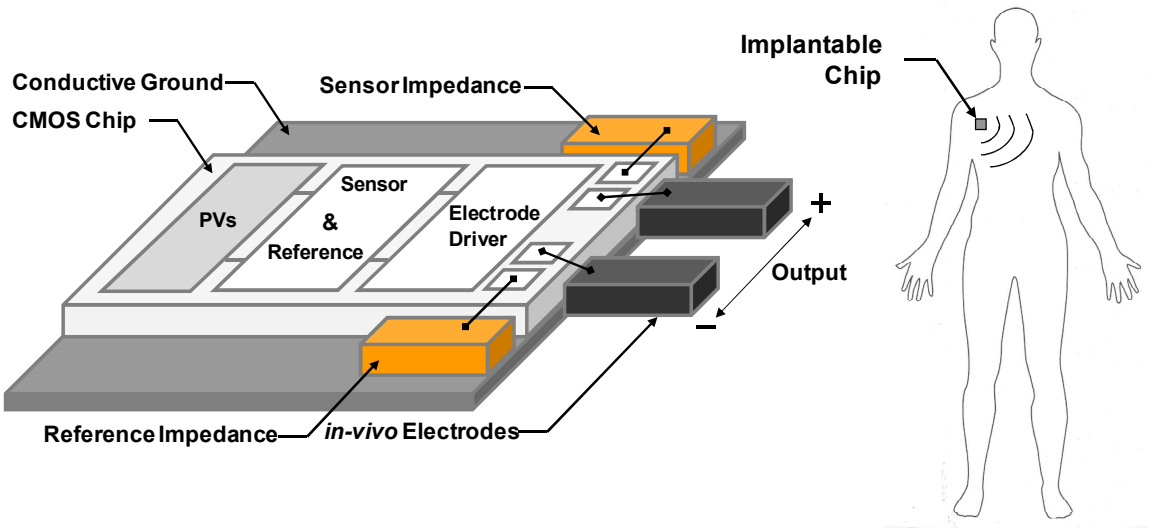

Figure 5.1: Top level architecture of the sensor.

The block diagram of the sensor is illustrated in Fig. 5.2. In order to efficiently utilize the <0.5V and sub-μW PV power supplies, a ring oscillator is implemented as the core sensing block. *In vivo* measurements can be done by altering the output frequency of the oscillator, f_S, based on the value of either a resistance- or capacitance-based off-chip transducer (e.g., thermistor [62] or MEMS pressure sensor [63]). Reference is a replica of the sensor except that no transducer is connected to it and is used for calibration purposes.

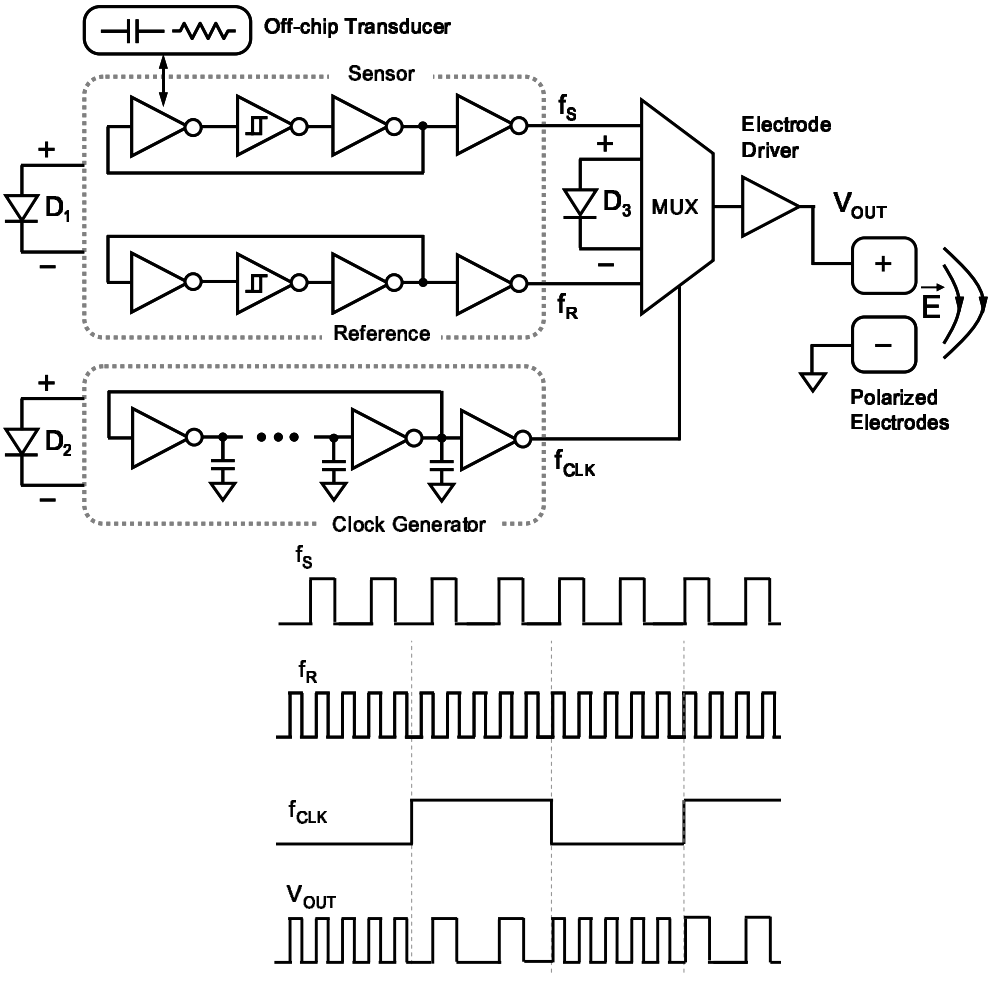

Figure 5.2: Top level architecture of the sensor and a scheme of the signals.

This particular topology has two advantages which make it appropriate for implantable applications. The first advantage is that the ring oscillator can operate in the sub-threshold region and with PV currents as low as 65nA. Such a current level, based on results of Fig. 3.7 and 4.15, requires only 0.5mW/mm^2 optical power at the surface of the skin, which is an in fact dim light condition. The second advantage is the measured output of this sensor is frequency-modulated; consequently it is less susceptible to amplitude-affecting non idealities of the transmission path through the tissue,. The oscillation frequency of this reference oscillator, f_R, is only a function of harvested current of D_1. Therefore, by measuring f_S and f_R concurrently, the PV current of D_1 is estimated first, and subsequently is used to determine the transducer value. A similar oscillator-based readout circuitry architecture is used in [64] for transmission of measured data along with the calibration data.

For transmitting the measured signal to the outside, a neuromorphic technique is used which its implementation was inspired by electrocardiography (ECG) systems [65]. In this method, the implanted chip mimics the heart muscle by creating a polarizing-depolarizing electrical field within the tissue that can be sensed by ECG electrodes on the surface of the skin. As illustrated in Fig. 5.2, a multiplexer unit (MUX) is incorporated in this system to time-interleave f_S and f_R into a FSK signal, which is then applied to a pair of *in vivo* polarized (non-Faradaic) electrodes. The time-interleaving clock, f_{CLK}, is generated by another on-chip 49-stage ring oscillator, powered by a separate 1mm^2 size PV cell (D_2). In the rest of this chapter, the details of the design of the system components will be described.

5.2 TRANSDUCER

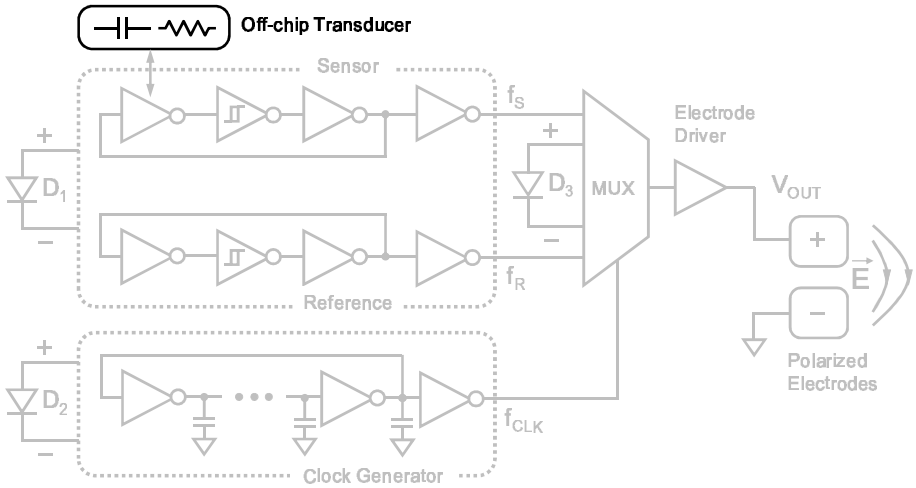

Figure 5.3: Off-chip transducer.

Since the focus of this research is on addressing the powering issue of implantable devices, the transducer is chosen to be a ready-to-use element. It can be either a variable capacitor or resistor, which can resemble sensors like MEMS pressure sensors [63] or thermistors [62], respectively. In the following sections it will be explained how the value of this unknown impedance is measured.

5.3 READ-OUT CIRCUIT

In this section the sensor, which is the core block of the system and has the role of reading out the physical variable, is discussed. First, an analysis about the operation of the sensor oscillator with the new powering method is presented. Next, the details of the final circuit will be discussed.

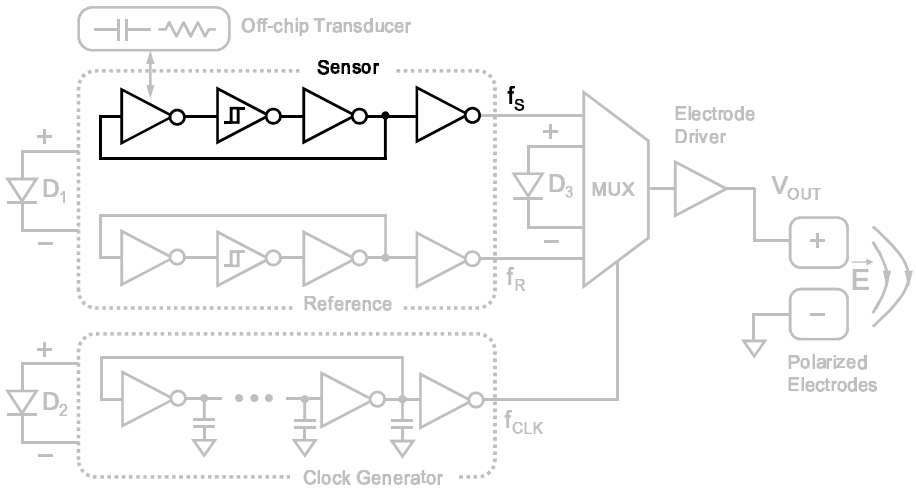

Figure 5.4: Sensor.

5.3.1 PV Ring Oscillator Analysis

The CMOS PV is designed to serve as the power supply for the circuit. However, the IV characteristic of the PV cell shows that it can never act as an ideal power supply which virtually provides unlimited current for a predefined voltage level. Fig. 5.5 shows the I-V curves of an ideal voltage source and a PV cell. V_S shows the voltage level of the ideal voltage source.

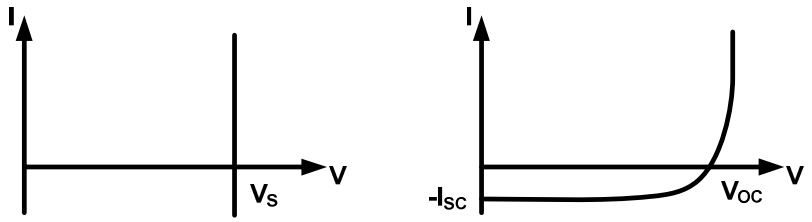

(a) (b)

Figure 5.5: Comparison of the I-V curve of (a) an ideal voltage supply with (b) a PV cell.

A PV cell generates an amount of current which is a function of its physical properties (doping level, junction depth.), the light condition, and finally the load connected to the cell. On the other hand, the cell is aimed to be used *in vivo*. Thus, the total available current will be small. According to calculations in Chapter 4, this value will be in the range of tens of nA.

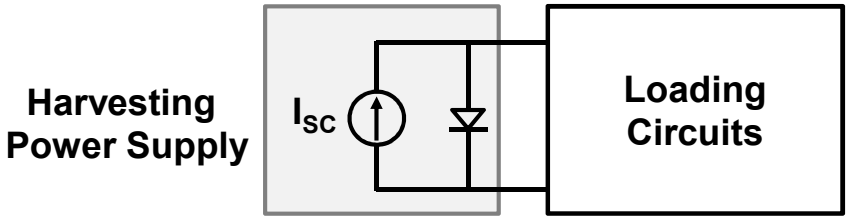

Figure 5.6: PV cell used as a direct power supply to run a device.

The maximum voltage available from the cell will be equivalent to its open circuit voltage which is around 0.5V according to the measurements presented in Chapter 4. This implies that any circuit implemented in 0.18µm CMOS technology with medium and high threshold devices will operate in sub-threshold region because most of the devices have threshold voltages below 0.5V. As a result, I decided to base the core of the sensor on a ring oscillator because a ring oscillator has a robust architecture and works in low current and low voltage conditions [66]. In this sub-section, the behavior of a three-stage, inverter-based ring oscillator fed by a PV cell is analyzed (Fig. 5.7.)

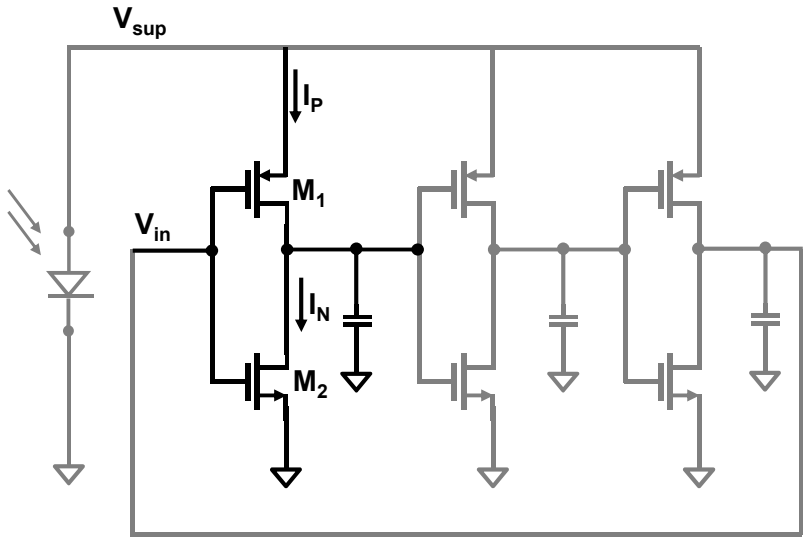

Figure 5.7: A three-stage inverter-based ring oscillator fed by the PV cell.

The model used in simulations for the PV cell is a first order cell model (Fig.4.2). In the sub-threshold region, the drain current of the devices are described as

$$I = I_s e^{\frac{V_{gs}}{nV_T}}, \tag{5.1}$$

where

$$V_T = \frac{kT}{q}. \tag{5.2}$$

In equation (5.2) k denotes the Boltzman constant and T and q stand for the absolute temperature and the electrical charge of an electron, respectively. n shows the ideality factor of the diode and equals one for an ideal diode where no defects are present. The PV cell open circuit voltage is a function of available photovoltaic short circuit current (I_{SC}).

$$V_{OC} = \frac{kT}{q} ln\left(\frac{I_{SC}}{I_s} + 1\right) \cong \frac{kT}{q} \ln\left(\frac{I_{SC}}{I_s}\right), \tag{5.3}$$

which means:

$$I_{SC} = I_s e^{\frac{V_{OC}}{V_T}}. \tag{5.4}$$

where I_s is the saturation current of the device. In the oscillator, the input/output of each stage switches between two voltage values, zero and V_{sup}, which is the voltage provided by the supply (PV cell) and is a function of its load. According to equation (5.1) the current passing through the PMOS and NMOS in a simple inverter stage can be described by the following equation:

$$I_P = I_s e^{\frac{V_{sup}-V_{in}}{nV_T}}, \tag{5.5}$$

and

$$I_N = I_s e^{\frac{V_{in}}{nV_T}}, \tag{5.6}$$

where V_{in} is the input voltage of the stage. Supply voltage (V_{sup}) can be approximated by V_{OC}, because at the instant that PMOS of one stage starts to draw current, the other stages are off and can approximately be assumed as open circuit loads for the PV cell. The stage that is drawing current also can be assumed to be a high impedance load for DC current because it can be modeled as a series connection of the PMOS on-resistance and the load capacitor. The PMOS draws current until the output voltage of that stage gets close to V_{sup} ($\approx V_{OC}$). So V_{sup} in equation (5.5) can be replaced by V_{OC} as in the following equation:

$$I_P = I_s e^{\frac{V_{OC}-V_{in}}{nV_T}}. \tag{5.7}$$

When the input is high (V_{in} equals V_{sup}), then $I_P = I_s \cong 0$ and $I_N = I_s e^{\frac{V_{OC}}{nV_T}}$, and if V_{in} is low ($V_{in} = 0$), then, $I_N = I_s \cong 0$ and $I_P = I_s e^{\frac{V_{OC}}{nV_T}}$. On the other hand, from (5.4) this value is equivalent to I_{SC} (assuming $n = 1$). When the output of a stage is rising or falling, the circuit can be assumed to be a current source with the value of I_{SC} in series

with a charging or discharging, respectively. Hence, the rise-time (T_r) and fall-time (T_f) of each stage is equivalent to

$$T_r = T_f = \frac{CV_{OC}}{I_{SC}}, \tag{5.8}$$

where C stands for the total capacitance at the output of the stage. The total period for a ring oscillator is expected to be approximately:

$$T = \frac{6CV_{OC}}{I_{SC}}. \tag{5.9}$$

The simulation results for a three-inverter ring oscillator confirms this result. In the simulated circuit, the aspect ratio of the PMOS and NMOS devices are $\frac{10}{0.18}\ \mu m$ and $\frac{5}{0.18}\ \mu m$, respectively. The capacitor at the output of each stage is 100 fF. Fig. 5.8 shows the transient output of the oscillator when I_{SC} of the feeding PV cell is equivalent to 200nA.

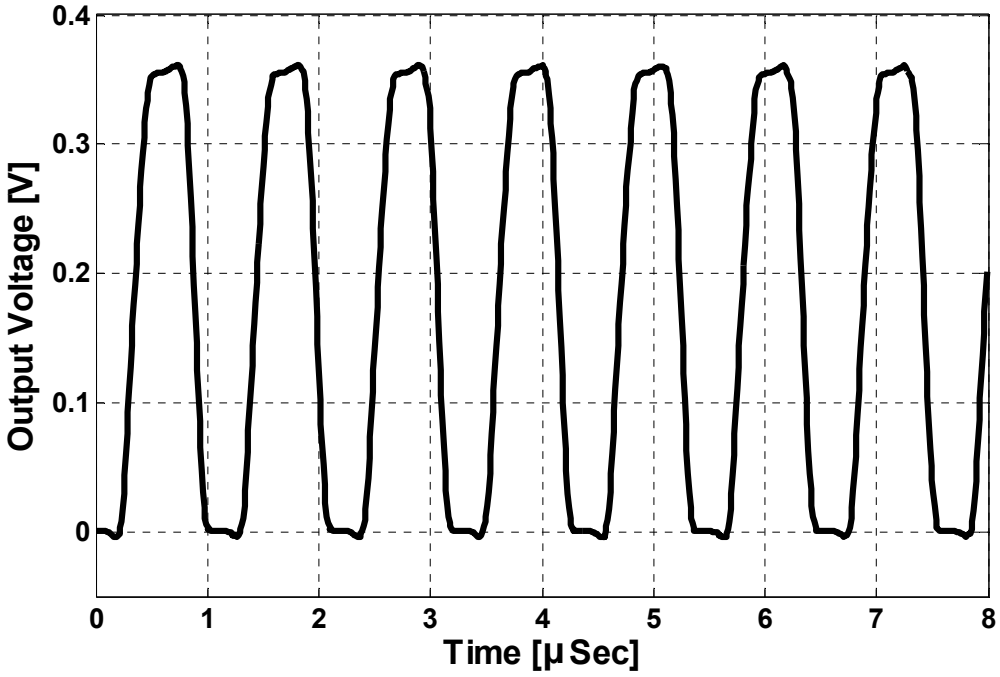

Figure 5.8: The transient output of the ring oscillator when I_{SC} is 200 nA.

The rise and fall delays of each stage ($T_r + T_f$) from calculation and simulation for $I_{SC} < 1\mu A$ is shown in Fig. 5.9. The two graphs show that the calculation results match the simulation results very closely.

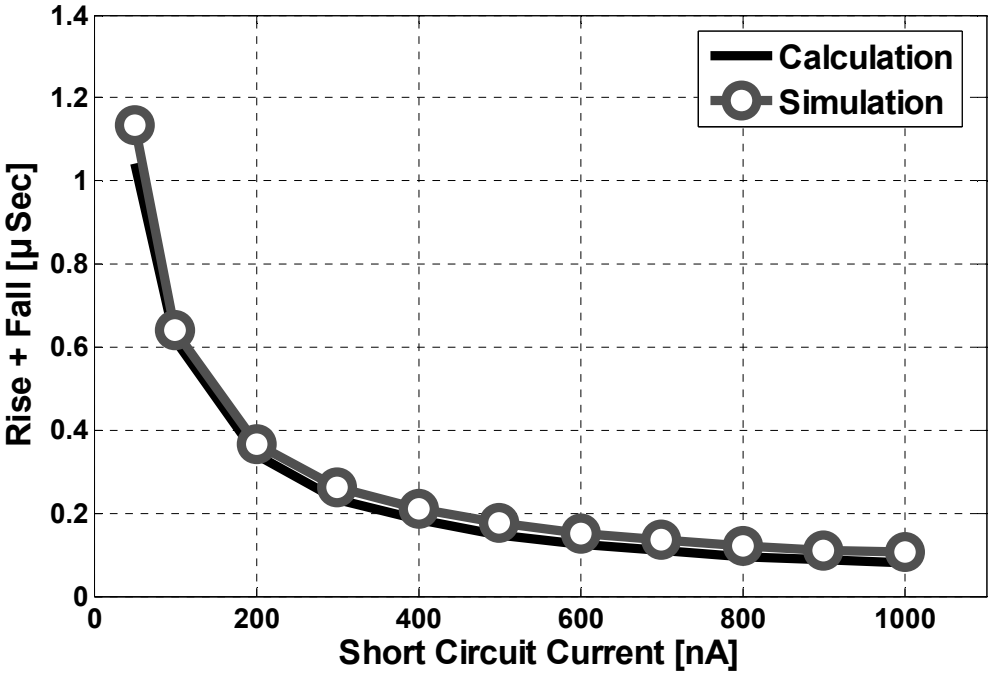

Figure 5.9: The rise and fall delay of one inverter stage with 100fF load capacitance.

5.3.2 Circuit Design

The analysis presented in the last section shows how the delay of the inverters changes with the I_{SC} of the PV cells. The result enables estimating the amount of current from the measured delay. However, as discussed before, the objective of designing this sensor is measuring an unknown resistance or capacitance. To accomplish this goal, the unknown element should be fit in one of the stages of the ring oscillator such that it modifies the frequency of oscillation. Subsequently, by observing the change in the frequency, the value of the unknown impedance can be calculated. Fig.5.10 shows the final architecture of the sensor. The off-chip transducer element modifies the delay of the first stage to change f_S and the switches facilitate alternating between resistive and

capacitive measurement modes. They can be eliminated in an implementation that functions only in one mode. The block is run by a quarter mm^2 PV cell (D_1).

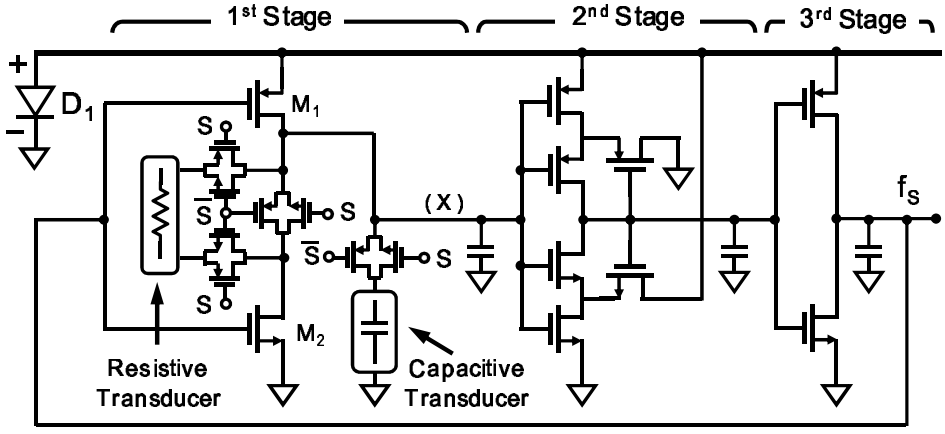

Figure 5.10: Final schematic of the sensor core.

5.3.2.1 First Stage

The core of this design is a three-inverter ring oscillator but the first two stages have been modified. The first stage is a modified inverter. The inverter is modified such that it provides the option of using the sensor in a resistive measurement mode too. Fig. 5.11 shows how this possibility is accommodated in the first stage of the sensor.

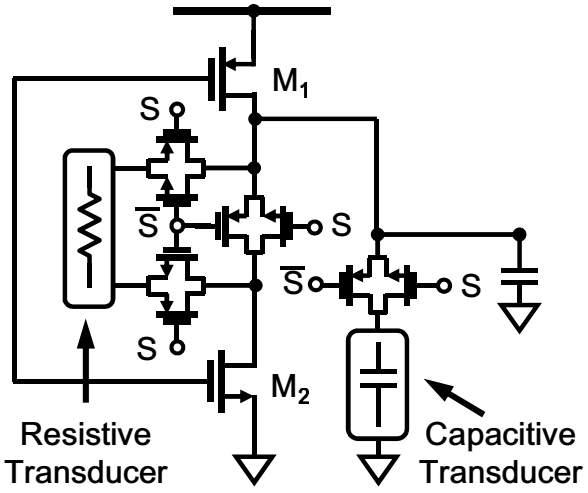

Figure 5.11: The first stage of the sensor read out circuit.

When S=1, the switches are set as the sensor works in capacitive sensing mode, and when S=0, the sensor will be in resistive sensing mode. As shown in Fig. 5.11, the switches are CMOS transmission gates with on-resistance of 142 Ω. In the capacitance sensing mode (S=1), pF-range capacitors are connected from the output node to ground to alter both the charging and discharging of node "X" through transistors M_1 and M_2, respectively. In the resistance sensing mode (S=0), the MΩ-range resistors are connected in series with M_2 to only affect the discharge without creating a DC path from node "X" to ground in the current-limited charge up phase.

5.3.2.2 Second Stage

In the second stage of the ring oscillator, a Schmitt-trigger inverter is implemented to increase the swing of node "X" and reduce the jitter of f_S. The block, shown in Fig. 5.12, has a well-known design [67].

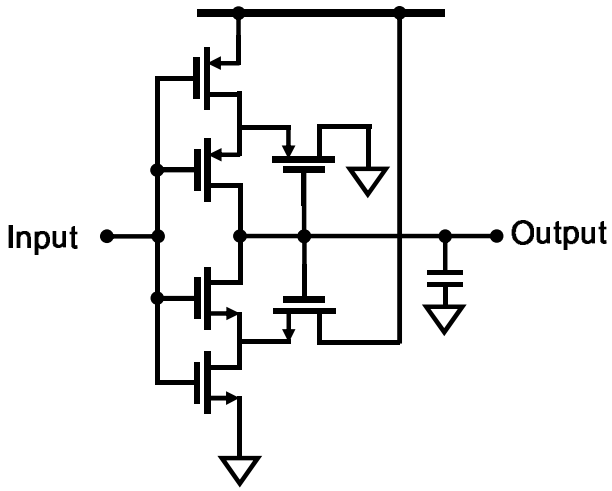

Figure 5.12: The schematic of the Schmitt Trigger block.

The input-output characteristic of the block when the I_{SC} of the feeding PV cell is 200 nA, is shown in Fig. 5.13. The graph demonstrates a 78mV hysteresis window. This hysteresis window protects the circuit against the noise from outside which might be injected from the unknown impedance connection node.

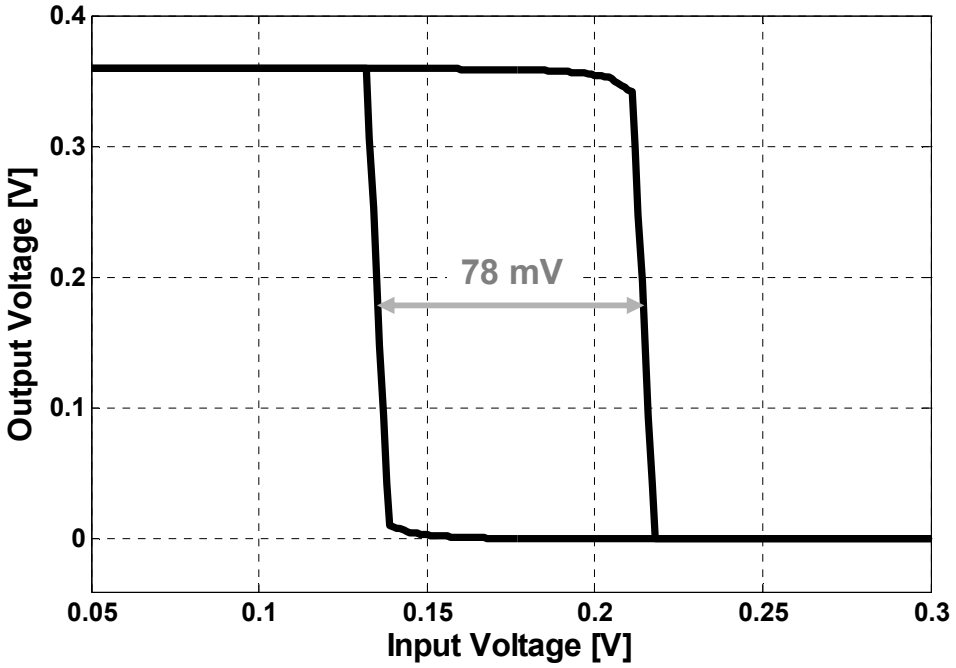

Figure 5.13: The input-output characteristic of the Schmitt Trigger block.

5.3.2.3 Third Stage

The third stage is a static CMOS inverter. To tune f_S within the 1–10 kHz frequency range, 100nF on-chip MIM capacitors are placed at each stage**.**

5.3.2.4 Reference Oscillator

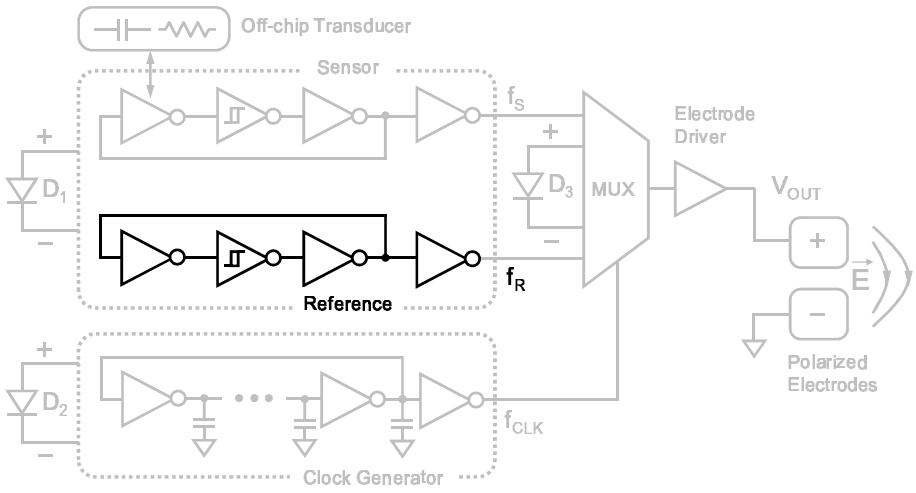

Figure 5.14: Sensor transfer function in the resistive mode for various current values.

The simulation results show that the frequency of oscillation is a function of I_{SC} that itself is a function of light condition. It is also obvious how the light condition will be a function of the environment in which the device exists. This makes the interpretation of the results very complicated. To address this issue, I implemented a reference circuit which is exactly equivalent to the sensor core and is fed by the same PV cell that feeds the sensor but has no unknown element connected to it. The reference impedance will be an open circuit in the capacitive sensing mode and a short circuit in the resistive sensing mode. The frequency of this reference oscillator is only a function of the environment and assists predicting the PV short circuit current. By knowing the short circuit current, the value of the unknown element can be figured out. In the next section it is shown how the frequency of oscillation is dependent on the unknown impedance.

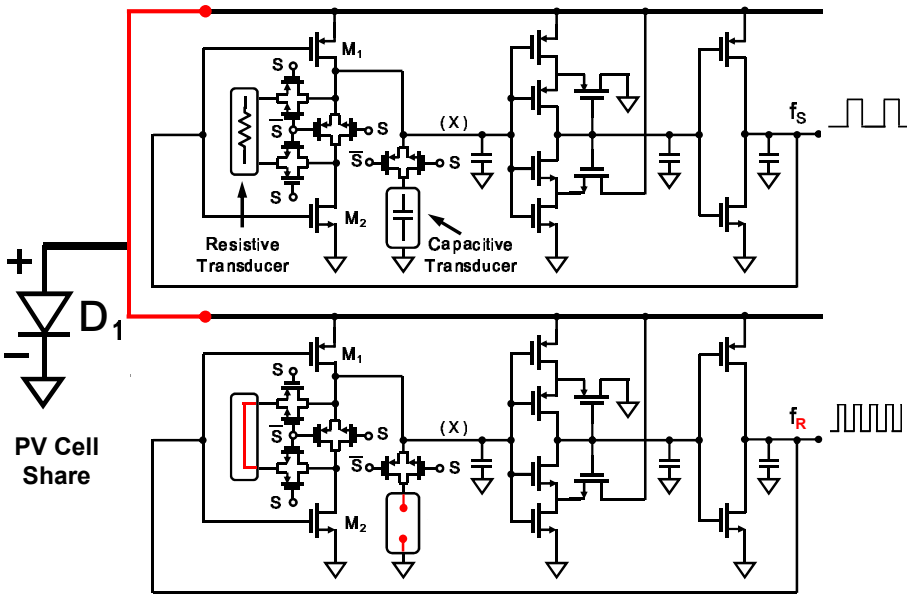

Figure 5.15: Sensor and reference schematic.

5.3.2.5 Interpretation of the Oscillation Frequency

In the capacitive sensing mode, I put the capacitance in the output of the first stage (see Fig 5.16).

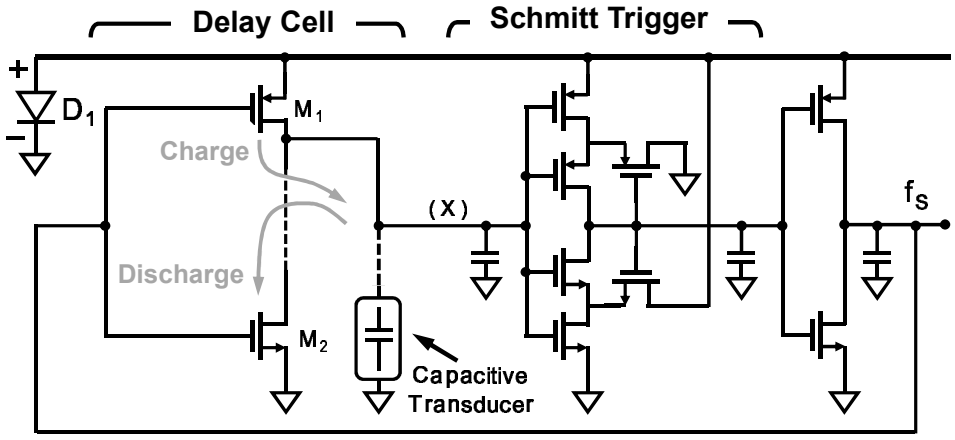

Figure 5.16: Sensor schematic in capacitive sensing mode.

Fig. 5.17 shows the transient response of the output for two values of capacitive transducer when I_{SC} of PV is equivalent to 50 nA. It shows how the charge and discharge phase lengthens with higher capacitance value.

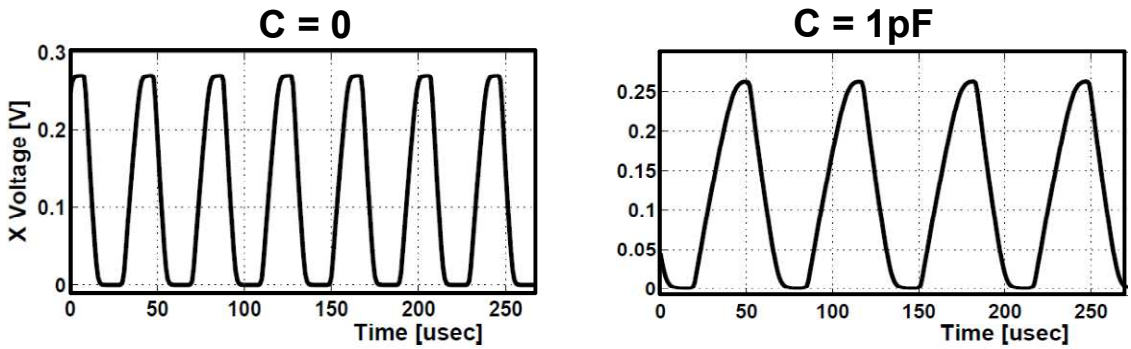

(a) (b)

Figure 5.17: Sensor transient output in capacitive mode for (a) C = 0, and (b) C = 1pF.

The delay of all the three stages should be known as a function of the unknown capacitance and the I_{SC} of the PV cell to make the calculation of the oscillation frequency possible. In the previous section, a closed form for the delay of the inverter stage was found. But, because of the presence of the switches in stage 1, the delay will be different from a plain inverter. On the other hand, finding a closed form for the rise and fall delay of the second stage is not an easy task. Therefore, characterizing the oscillation frequency of the sensor can be carried out by multiple simulations for various light conditions and capacitor values. You can find these characterizations in Appendix A. Fig. 5.18 shows the final sensor transfer function in the capacitive mode for a couple of light conditions (i.e. I_{SC} of the PV). The sensor transfer function is defined as $f_{R-}f_S$ vs. unknown capacitance. As expected, this difference increases by the available current from the PV cell and the variable capacitor.

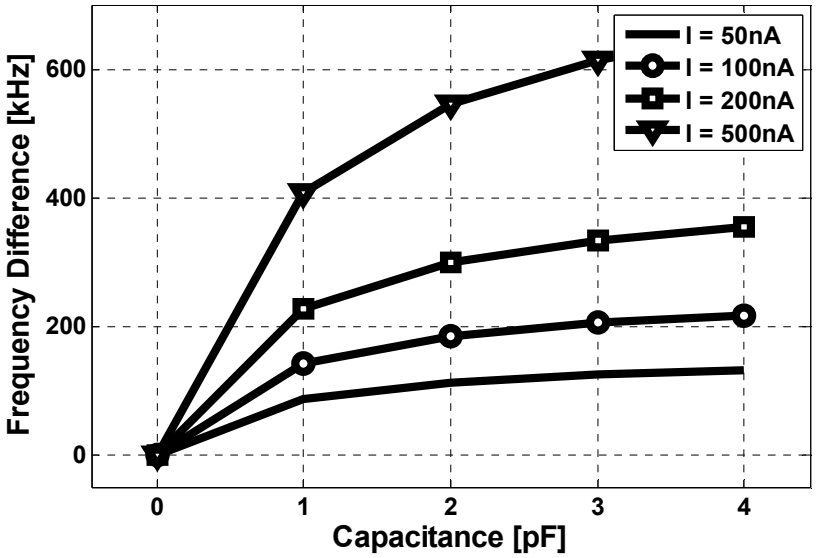

Figure 5.18: Sensor transfer function in capacitive mode for various current values.

In the resistive sensing mode, I put the resistor in the path between the capacitor and the bottom NMOS device. The sensor architecture will look like Fig. 5.19 when it is in the resistive sensing mode. The analysis of the delays in resistive sensing mode can be found in Appendix B.

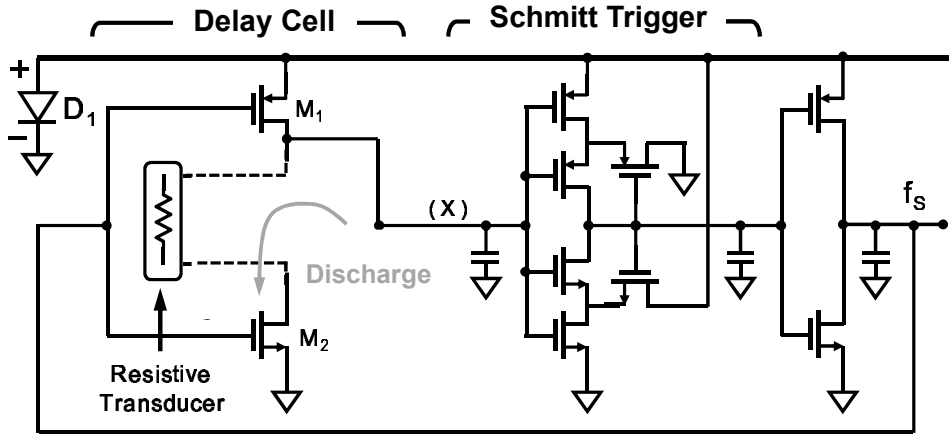

Figure 5.19: Sensor schematic in resistive sensing mode.

Fig. 5.20 shows the transient response of the sensor in resistive sensing mode for resistive transducer values of 10 Ω and 10 MΩ. I_{SC} of PV is equivalent to 50 nA in these cases.

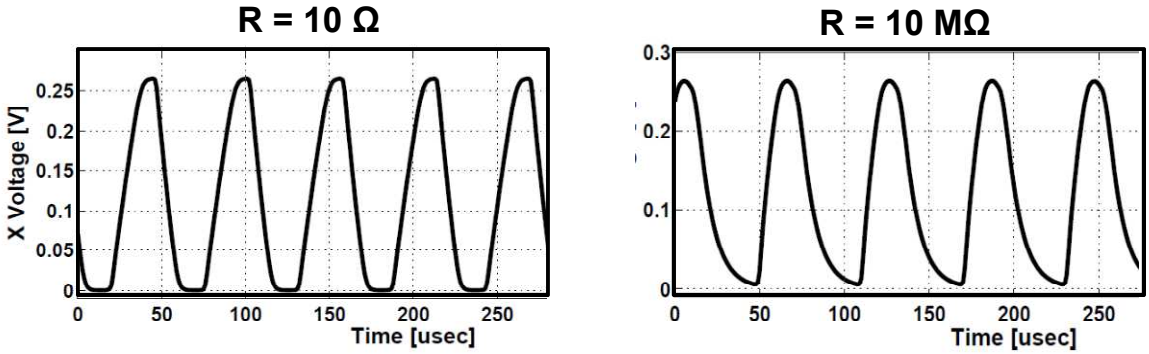

(a) (b)

Figure 5.20: Sensor transient output in resistive mode for (a) R = 10Ω, and (b) R = 10 MΩ.

The graphs in Fig. 5.21 depict sensor transfer function, $f_R - f_S$ vs. unknown resistance for a range of resistors and various light conditions.

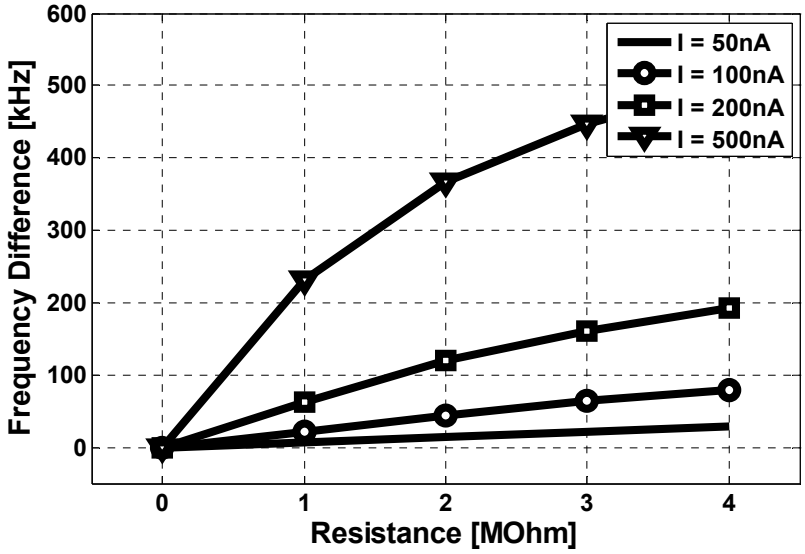

Figure 5.21: Sensor transfer function in the resistive mode for various current values.

The frequency difference is higher at higher levels of PV short circuit current and higher levels of resistor.

5.4 TRANSMITTER AND OUTPUT INTERFACE

For transmitting the measured signal to outside, a neuromorphic technique is used that was inspired by electrocardiography (ECG) systems. In this method, the implanted chip mimics the heart muscle by creating a polarizing-depolarizing electrical field within the tissue that can be sensed by ECG electrodes on the surface of the skin. As illustrated in Fig. 5.2, a multiplexer unit (MUX) is incorporated in this system to time-interleave f_S and f_R into a FSK signal, which is then applied to a pair of *in vivo* polarized (non-Faradaic) electrodes. This section discusses the details of the circuit.

5.4.1 Timer

The timer generates a clock signal with the aid of which the frequency shift keying of the sensor and reference signals can be realized. The exact value of f_{CLK} is not critical. The only requirement is that its value has to be much less than f_S and f_R (e.g., below 200Hz) to ensure that f_S and f_R can properly be detected and differentiated. For this reason, an on-chip 49-stage ring oscillator is implemented and powered by a separate 1 mm^2, PV cell (D_2). To further decrease the frequency of the timer, 100 nF capacitors are inserted at the output of each stage.

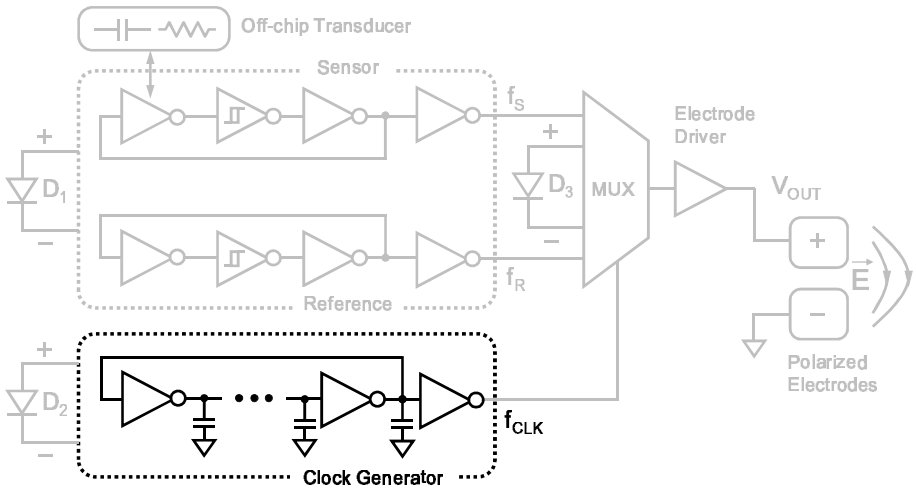

Figure 5.22: Clock generator.

5.4.2 Multiplexer and Electrode Driver

Multiplexer (MUX in Fig. 5.23) does the job of time interleaving the output of the sensor and reference by the aid of clock signal, and electrode driver prepares the signal to be sent out to the *in vivo* electrode. One dedicated 1mm^2 size PV cell (D_3) provides power for this part of the system.

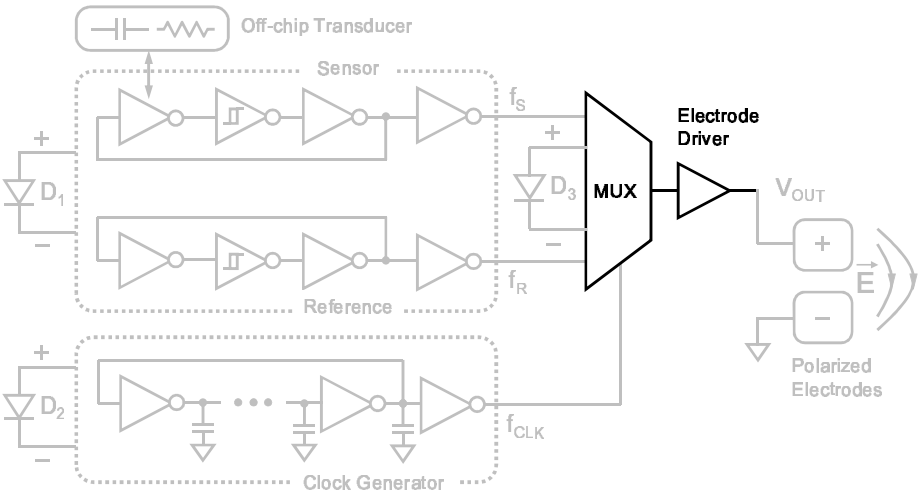

Figure 5.23: Multiplexer and electrode driver.

Fig. 5.24 shows the circuit structure of the electrode driver. First to create a FSK signal, the output signals from sensor and reference oscillators are multiplexed, using a pair of transmission gates. The generated signal is then passed through a couple of static CMOS inverters for buffering and finally is applied to trigger the polarizing-depolarizing switches (M_{pol} and M_{dpol}).

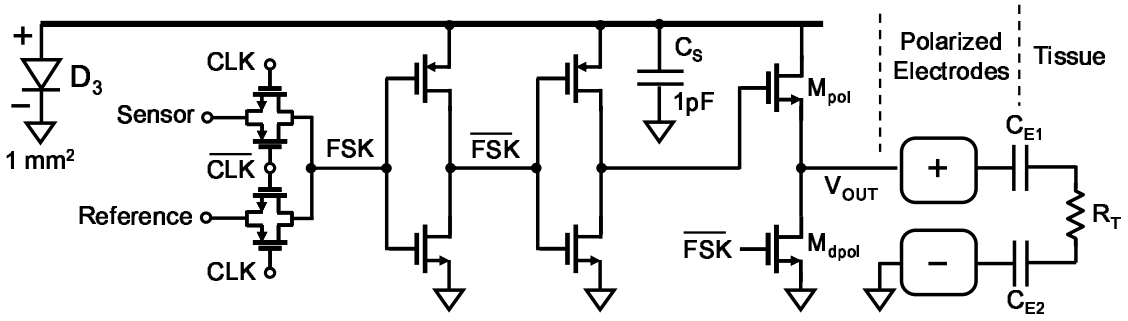

Figure 5.24: Circuit diagram of the electrode driver.

A PV cell (1 mm^2) is dedicated to this block to prohibit kicking back the generated signals to the sensor and reference, which could modulate their outputs and generate false tones.

5.4.3 Electrode-Tissue Modeling

As discussed in the previous section, a sensor and a reference oscillator are used to interpret the collected data. These two signals need to be sent to the outside world. Here, the modeling of the interface of the electrode and tissue inside the body is discussed.

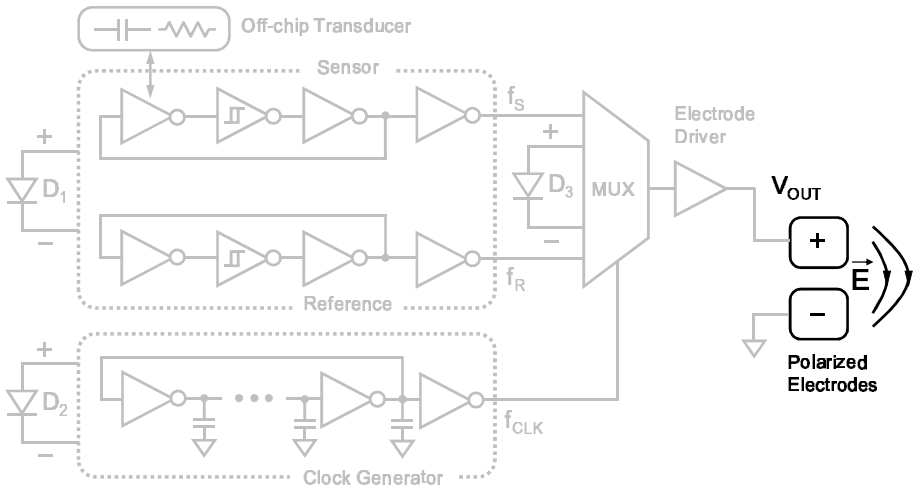

Figure 5.25: Polarized electrodes.

It is important to understand that the load for driver circuitry is the *in vivo* electrode pair that is in contact with the tissue. The actual value of the load (*i.e.*, input impedance of the electrode-tissue interface) depends on the area of the electrode and the physiochemical characteristics of the tissue. Studying all aspects of this problem is beyond the scope of this thesis and therefore a semi-empirical approach is chosen to design the electrode system and the driver circuitry.

In this approach, the tissue is modeled as a homogeneous electrolyte with constant resistivity. Therefore, the impedance seen by the driver circuitry can be represented by the impedance model of an electrode-electrolyte interface [65] as shown in Fig. 5.25. E_{hc} shows the half-cell potential between the metal and the electrolyte. Since we are interested only in the time varying component of the transmitted signal, the half-cell potential formed between the tissue and the metal interface has a negligible effect on the measured signal and therefore, we neglect it in this model.

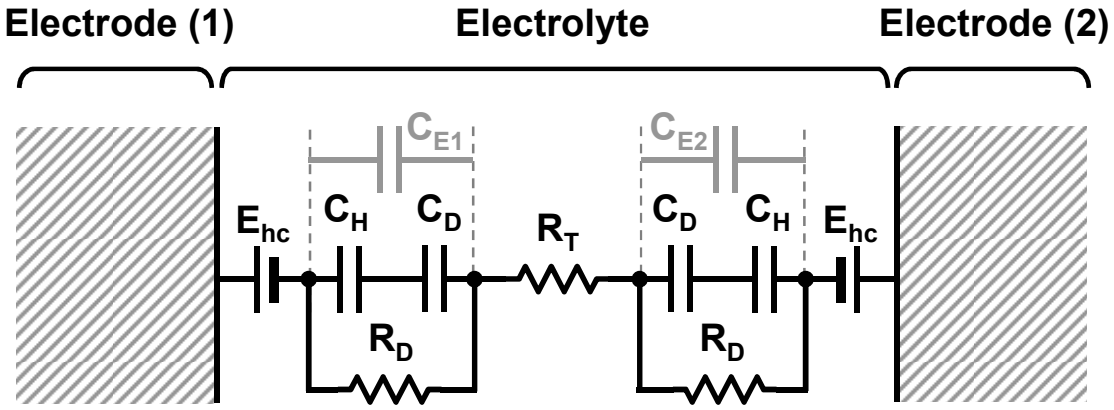

Figure 5.26: Electrode- tissue interface model.

The capacitances present in this model are from the layer of adsorbed ions on the interface (also called the Stern layer) and diffusion layer (C_H and C_D, respectively). The overall capacitance at each electrode (C_{E1} and C_{E2}) when the salt concentration is high is around 10-20 μF/cm^2 [68], which is generally dominated by the value of the smaller capacitance, C_D. At the frequency of interest, the impedance of this capacitance is much smaller than the electrode-electrolyte interface resistance (R_D) and hence, R_D is also ignored in the final impedance model. Finding the tissue resistive load, R_T, is more involved, since it is not only a function of electrode area, but also its topology. In this design, the method described in [69] is used to estimate R_T, which offers formulations to compute the equivalent resistance of an electrolyte seen through two planar electrodes as shown in Fig. 5.27. For an electrolyte (tissue here) with resistivity ρ_T, the value of R_T is

$$R_T = \frac{\rho}{L} \cdot \frac{2\theta(k)}{\theta(\sqrt{1-k^2})}, \tag{5.10}$$

where

$$k = 1 - \frac{2W}{2W + D}, \tag{5.11}$$

and

$$\theta(k) = \int_0^1 \frac{d\alpha}{\sqrt{(1-\alpha^2)(1-k^2\alpha^2)}}. \quad (5.12)$$

According to [70], the resistivity of the live human muscle is between ~500 to ~1050Ωcm. To create electrodes which are within the same dimensions as the CMOS IC, 1mm^2 electrodes with 2mm pitch are used in this implantable sensor. Based on (5.10) to (5.12), the predicted value for R_T is between 6.1 kΩ and 12.8 kΩ. Furthermore, the interface capacitance using the 10-20μF/cm^2 assumption is 100-200nF. Hence, the electrode load (*i.e.*, lower impedance) can be estimated to be 300nF || 1kΩ.

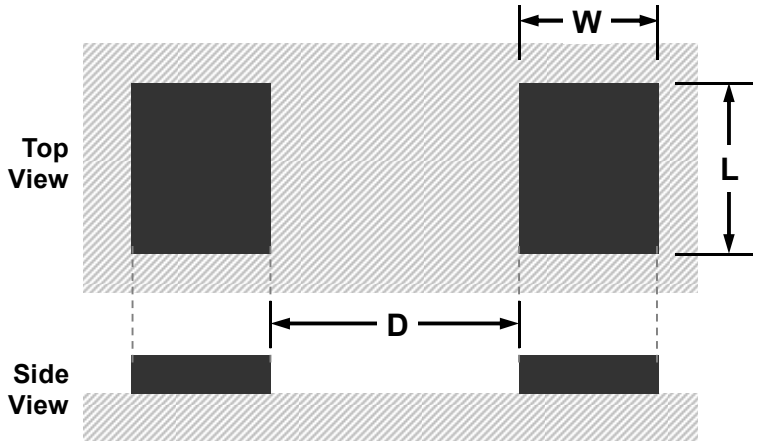

Figure 5.27: Planar two-electrode structure.

5.5 BUFFER

In order to measure the oscillating frequency of the sensor and reference individually, I have implemented a buffer in the circuit, which is not shown in Fig.5.2. I have the option of sending each output (sensor or reference) to the buffers or through the electrode driver. The buffer has also the option to be powered by an ideal power supply or with a dedicated PV cell (D_2, when it is not used by the electrode driver). The size of

the devices in the second and third stages is larger than the first and second stages respectively to enable driving the load at the output. The load which will be one of the probing devices usually has a large capacitor at the input port (e.g. 25pF).

5.6 SUMMARY

This chapter discussed the design of the sensor and the challenges for this particular application. Fig. 5.28 illustrates the die photo of the circuit and the dedicated areas to each circuit block.

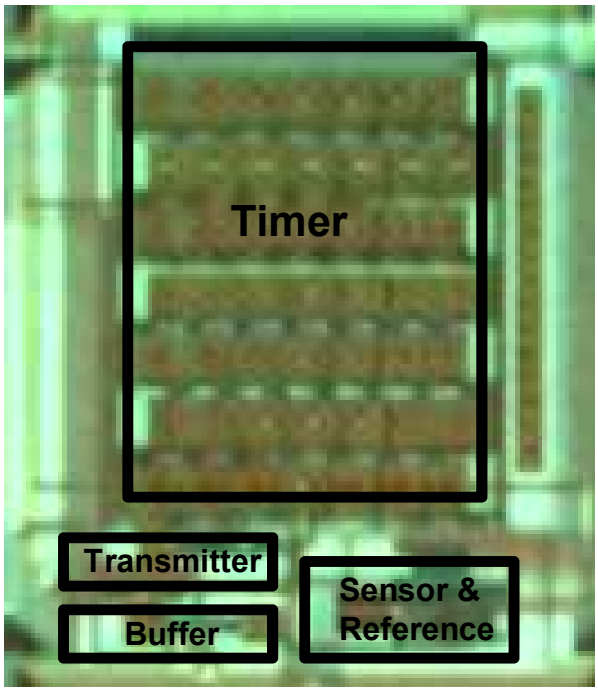

Figure 5.28: Die-photo of the circuits

In Fig. 5.29, the final implemented system is demonstrated, which includes the CMOS IC, the polarized electrodes, and an off-chip transducer. The total area is approximately 16mm^2 and the thickness is less than 0.5mm.

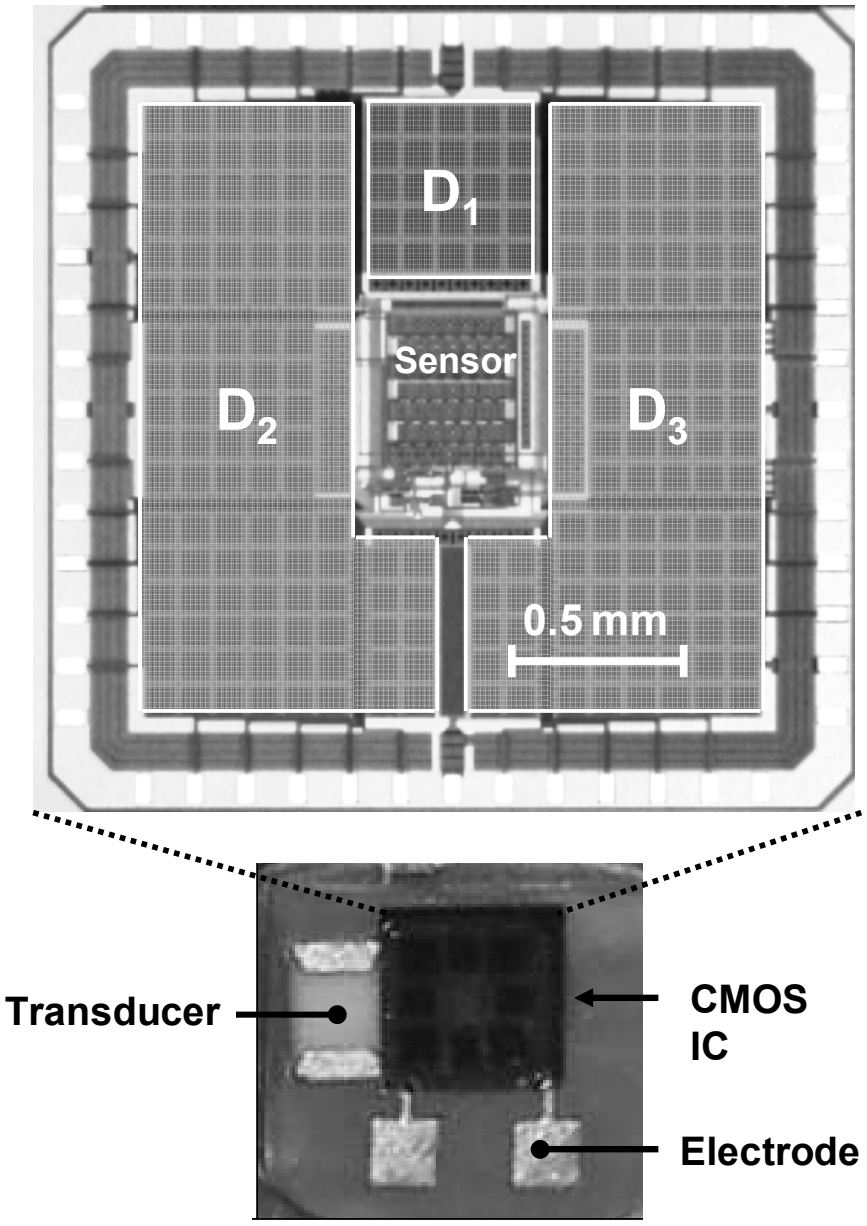

Figure 5.29: Die-photo of the whole device and a possible final structure

The next Chapter will demonstrate the measurement results.

Chapter 6: Sensor Measurement Results

6.1 INTRODUCTION

In the previous chapter, the design and implementation of a fully integrated standard CMOS power harvesting sensor was demonstrated. The measurements of this device include electrical, optical, and *in vitro* tissue-involved experiments for various parts of the chip. This chapter presents the measurement results.

The measurements can be classified into two main categories. In the first category, the optical and electrical characteristics of the sensor are evaluated from different aspects. In the second category, the *in vitro* measurement results of the whole device are discussed. During all the measurements, the chip which is a 44 pin die fabricated in standard 0.18µm CMOS technology is inserted into a 44 pin PLCC package mounted on the Printed Circuit Board (PCB) as shown in Fig. 6.1.

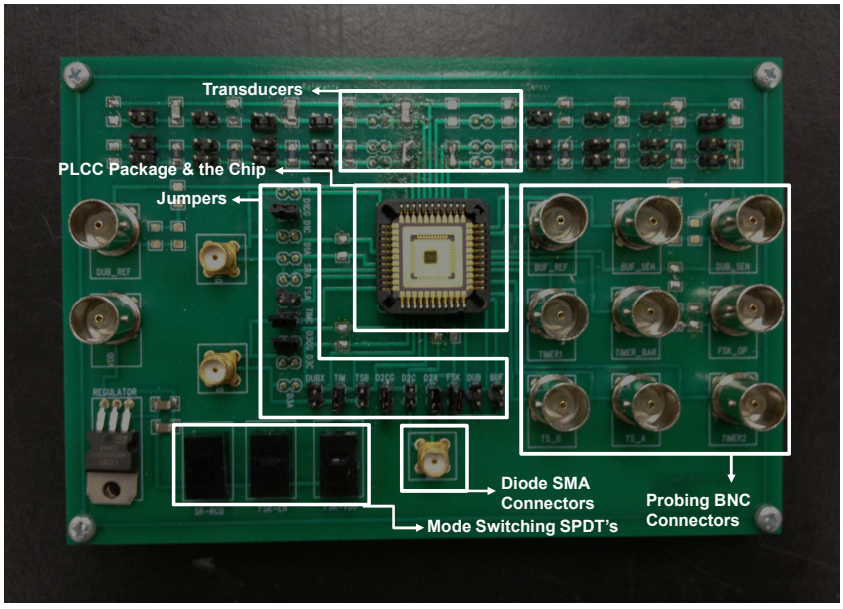

Figure 6.1: Printed circuit board (PCB) used for the measurements

6.2 OSCILLATION FREQUENCY

To understand how the oscillation frequency varies with illuminance, I formed a setup shown in Fig 6.2.

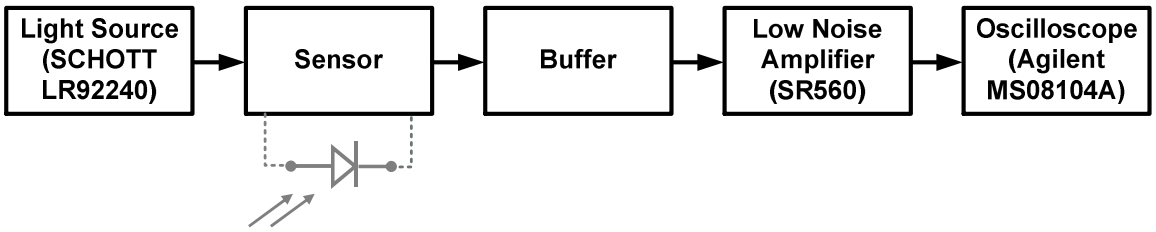

Figure 6.2: Test setup for characterizing the sensor

The variable light source is a 150-watt halogen microscope illuminator (SCHOTT LR92240 ACE-I). The light source has been calibrated by several measurements with a light meter (Extech HD450). By knowing the illuminance of the light source and its power, the incoming photon flux power can be estimated. Knowing the halogen lamp characteristics and given that the diameter of the light sensor in the light-meter is one inch, the total power of the light received by the sensor can be estimated from the total illuminance received by the sensor. The halogen lamp luminous flux is approximately 3600 lumens [71] for 100 Watts power. Since the luminous flux changes in proportion to its physical photometric equivalent in watts, the electrical power can be calculated, knowing the luminous flux received.

Fig. 6.3 shows the measured oscillation frequency of the reference oscillator as a function of incident photon flux illuminance. There is no transducer connected to the oscillator in these measurements (open and short circuit for capacitive and resistive modes). As evident, the frequency of oscillation is within the kHz range for both resistance and capacitance sensing modes; a range which can easily be sensed using conventional ECG electrode on the skin.

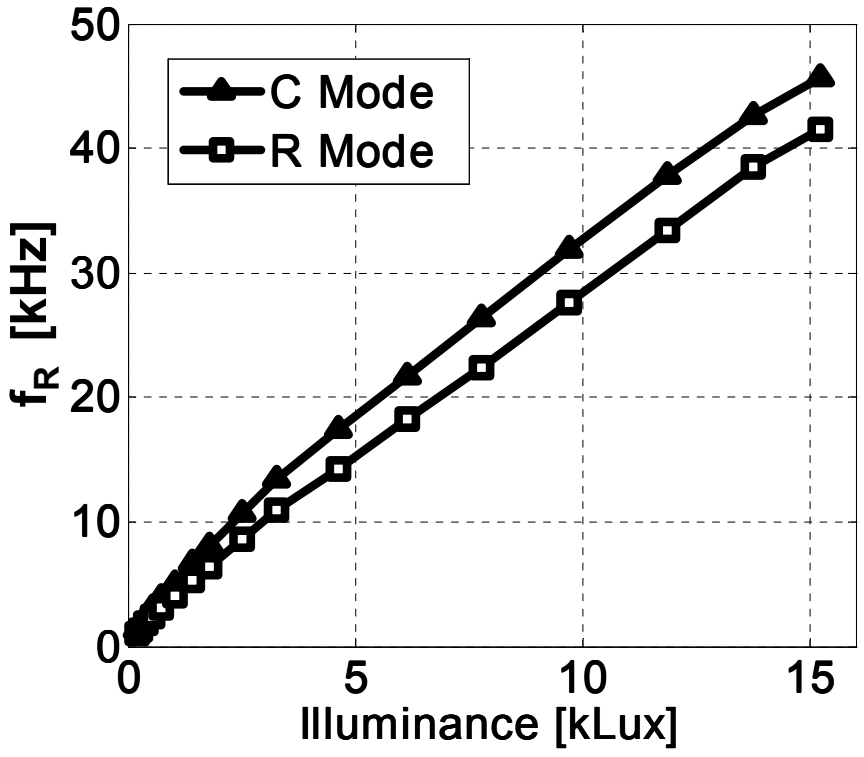

Figure 6.3: Reference frequency vs. illuminace in Capacitive and resistive sensing modes

As expected from equation (5.9) the frequency of oscillation increases with illuminace, which indicates an increase in short circuit current in the PV cells.

6.3 PHASE NOISE

The setup shown in Fig. 6.4 was used to measure the phase noise of the oscillator. The chip was illuminated by an LED flashlight. A flashlight was used because it is DC battery powered and the fluctuation in the light source is minimal. In this test the buffer is powered by a PV cell.

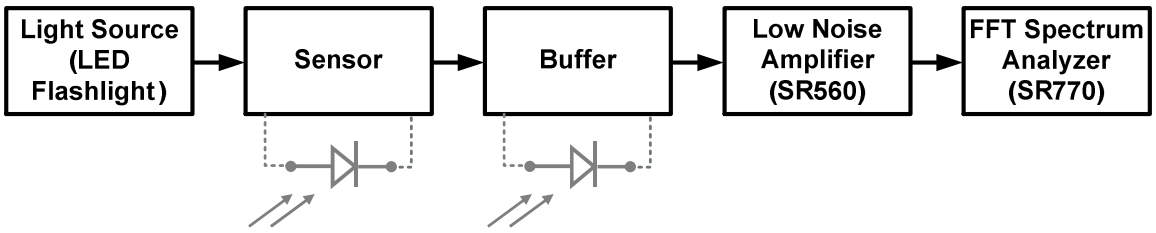

Figure 6.4: Phase noise measurement setup

In this test, the reference frequency in resistive mode was measured under 1.2klux illuminance. Fig. 6.5 shows the normalized spectral power vs. the offset frequency from the main tone.

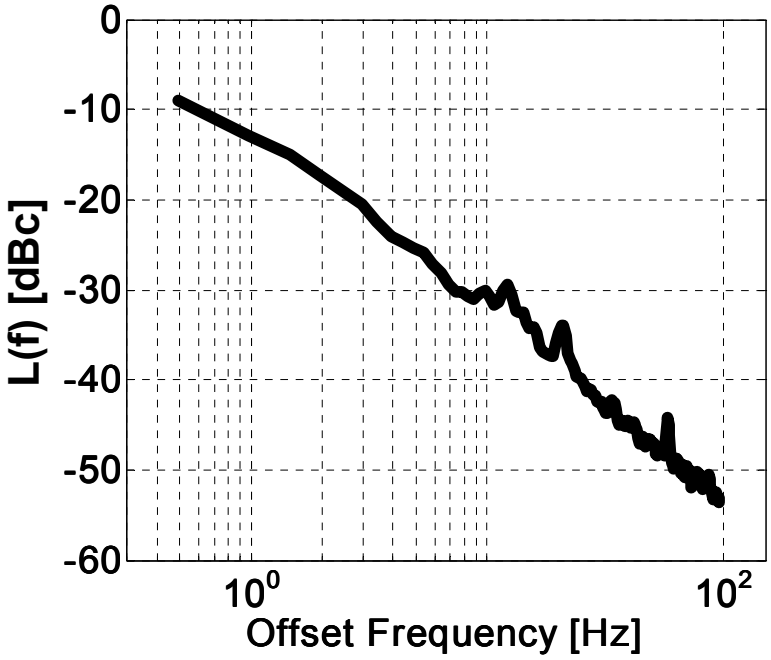

Figure 6.5: Phase noise of R-mode reference tone at 6.2 kHz under 1.2 klux

6.4 SENSOR TRANSFER FUNCTIONS

The transfer function of a sensor shows the relation between the physical input and the observed electrical output. In this sensor, I define the transfer function as the relation between the resistance or capacitance values and the observed frequency difference between the sensor and the reference. In order to determine the transfer function of the sensor in the two modes (capacitive and resistive sensing modes), I used the setup shown in Fig. 6.2 and measured the frequency of oscillation as I changed the parameters. In Fig. 6.6 and 6.7, the measured sensor transfer functions for both modes of operation are reported. Based on this data, at 2.5 klux, $\Delta f = f_R - f_S$ has a sensitivity of 600 Hz/pF and 390 Hz/MΩ for capacitance and resistance sensing modes, respectively. As discussed previously, if illuminance is measured indirectly, the value of Δf is sufficient for estimating the transducer value.

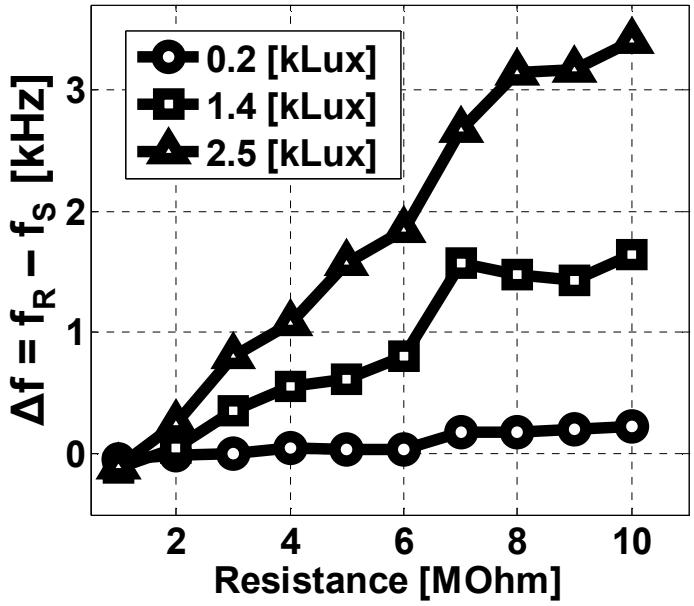

Figure 6.6: Sensor transfer function in resistive measurement mode at three levels of illuminace.

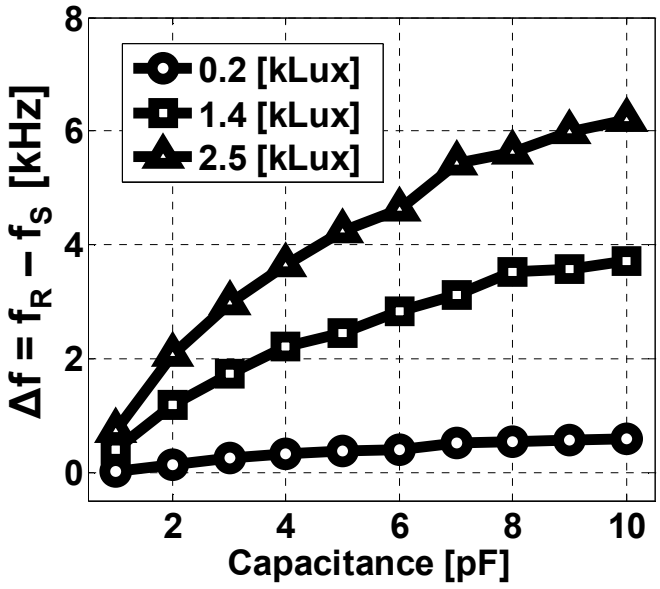

Figure 6.7: Sensor transfer function in capacitive measurement mode at three levels of illuminace.

Allan variance is a parameter that shows frequency stability in components like clocks and oscillators. This parameter can be calculated from phase noise data [72] using Cutler's equation (6.1). This power-law model is frequently used to estimate the Allan variation. It assumes that the spectral density of normalized frequency fluctuations is equivalent to sum of the terms that vary as integer power of Fourier frequency. Therefore, the slope of the output in a log-log graph and its amplitude should be known to find out the value of the frequency fluctuations. The slope (α) is a straight line (f^{α}) in the log-log graph.

$$\sigma^2(\tau) = h_{-2}\left(\frac{2\pi}{6}\right)^2 \tau + h_{-1} 2\ln(2) + \frac{h_0}{2\tau} + h_1 \frac{\left[1.038 + 3\ln(2\pi f_h \tau)\right]}{(2\pi)^2 \tau^2} + h_2 \frac{3 f_h}{(2\pi)^2 \tau^2} \quad (6.1)$$

In this equation τ represents the sampling time, and $\sigma^2(\tau)$ stands for the frequency variation for the respective sampling period (τ). h_i shows the amplitude of the f^{α} line. Figure 6.8 shows how the values of h_i can be extracted from the phase noise graph. The values of h_i are listed in Table 6.1.

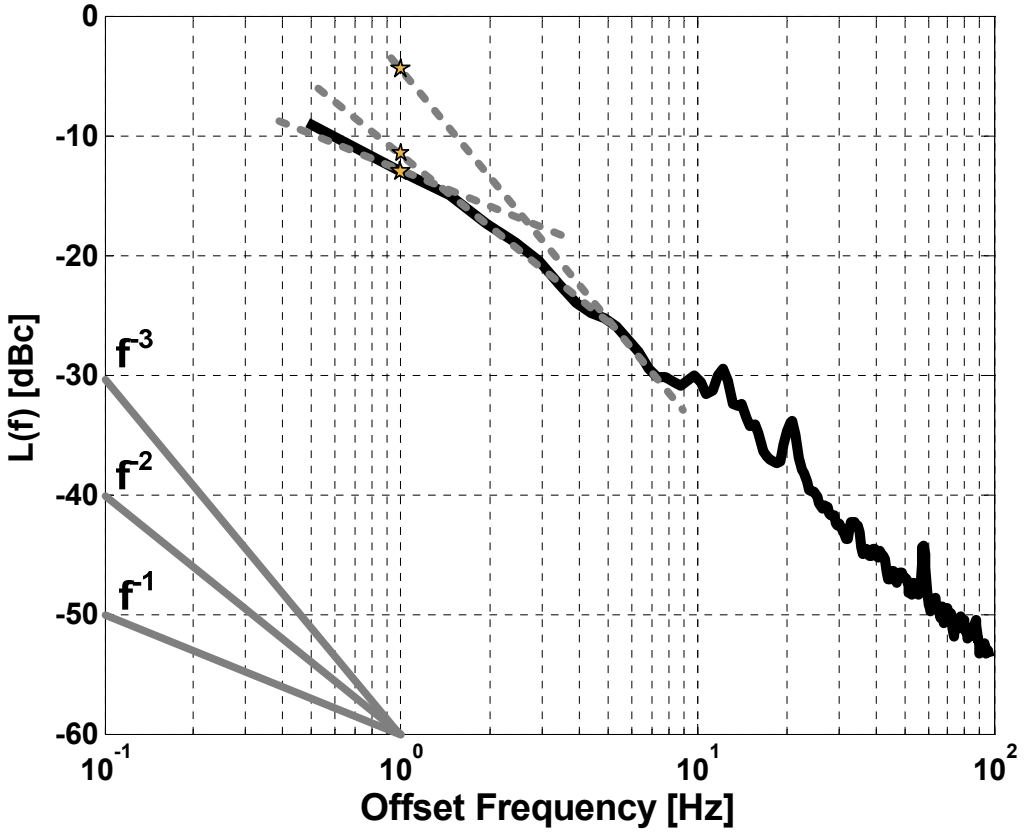

Figure 6.8: Deriving the Cutler's equation parameters for the Allan variance calculation

Parameter	Slope	Cross Section (dB)
h_{-2}	f^{0}	-200
h_{-1}	f^{-1}	-13
h_{0}	f^{-2}	-12
h_{1}	f^{-3}	-7
h_{2}	f^{-4}	-200

Table 6.1: Cutler's equation parameters extracted from noise figure shape

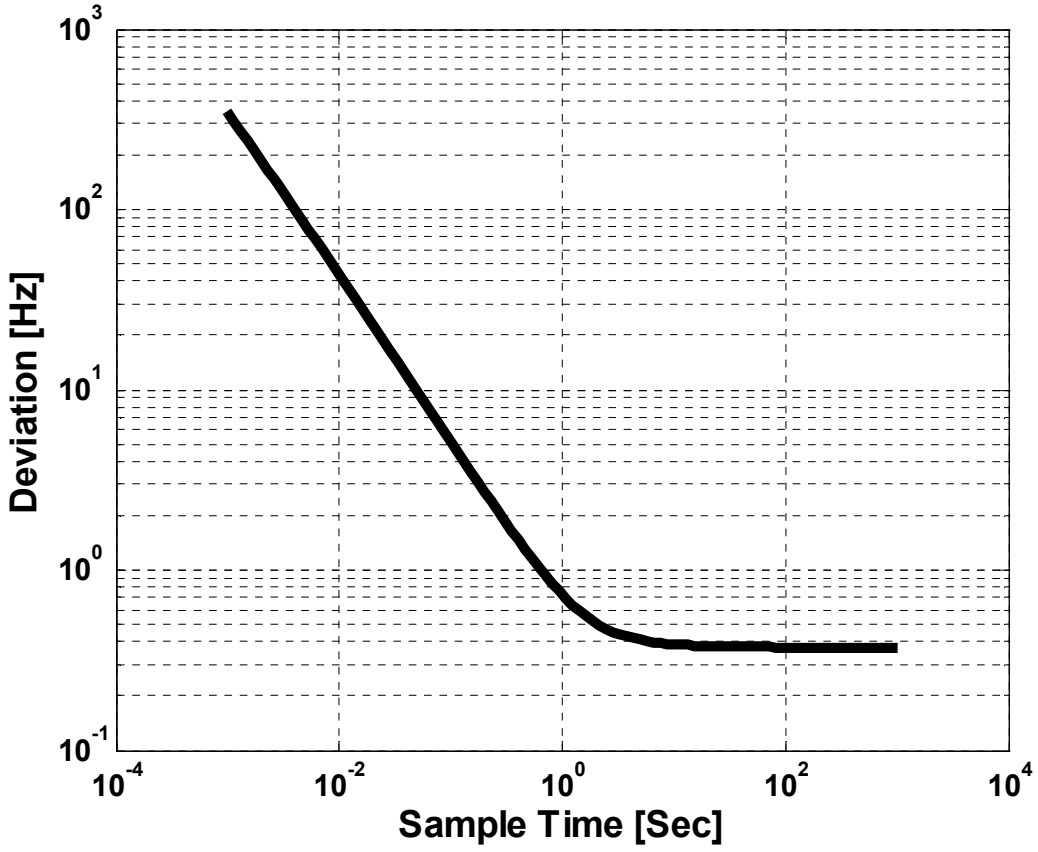

Figure 6.9: Deviation in frequency measurement (Allan deviation) vs. sampling time

The Allan deviation for a 1sec sampling period is equivalent to 0.7 Hz. This value corresponds to MDLs of 1.2 fF and 1.8kΩ for 1 sec measurements. However, in actual *in vivo* applications, this level of accuracy has not been demonstrated and so far MDLs in the range of 100fF and 153kΩ range have been achieved. This is mainly due to unwanted spontaneous fluctuations of f_S which originate from ambient light (energy source) instabilities, 60Hz power line coupling into the tissue, motion artifacts and other *in vivo* interference sources. The next section shows how the light fluctuations affect the sensor output.

6.5 LIGHT FLUCTUATION MEASUREMENT

The fluctuations in the light source result in the generation of unwanted tones in the sensor oscillator. More analytical details about the variations in the light source are presented in Appendix C. In this section, the measurement results of two light conditions are demonstrated which show how the fluctuations in the light source appear in the output of the sensor. The setup shown in Fig. 6.4 is utilized for this experiment. The chip is lit by the specific light source and the output of the sensor is connected to the spectrum analyzer. In this set of measurements two types of light source were used. In the first test, a halogen lamp run by main power lines, was used to light the chip. In the second measurement, the chip was lit by a flashlight run with all-purpose batteries. All of the components in the chip are run by the COMS PV cells that exist in the chip. When the chip is lit by the lamp, two unwanted tones with an offset of 60 Hz are observed around the main tone (Fig. 6.10a). These signals are 10dB smaller than the main tone. When the circuit is lit by a flashlight, a constant amount of photon flux hits the chip surface and the

main tone is observed without any considerable interfere around it. The spectrum is shown in Fig. 6.10b.

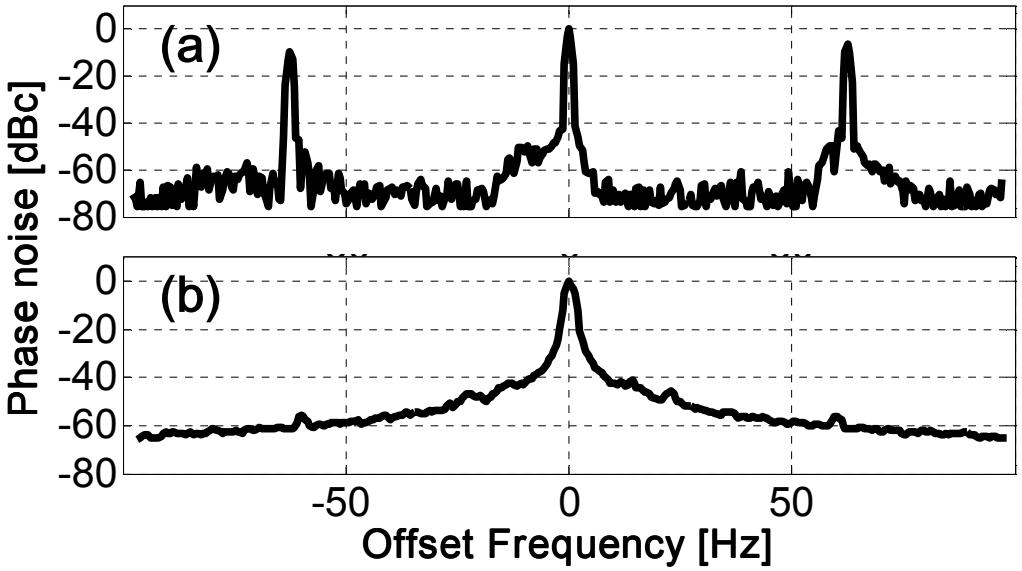

Figure 6.10: Measured spectrum of the sensor output when lit by (a) incandescent light run by power line and (b) flashlight run by batteries

These unwanted tones can complicate distinguishing of the main signal. Should this circuit be used in a specific light condition, the properties of the light source must be clearly characterized. An important specification of theses interferers is that they appear symmetrically around the main tone. So they can be distinguished from the unknown signals that are going to be measured.

6.6 TEMPERATURE TEST

Temperature is another environmental factor that affects the measurements. Since the Silicon optical absorption, carrier mobility, and threshold voltage all vary as a function of temperature [73-74], it is important to study the behavior of the circuit with

temperature. The knowledge of the circuit temperature dependence is required for correct interpretation of the sensor measurement results.

Silicon optical absorption increases with temperature and it means higher short circuit current level in the PV cell, hence higher frequency. But carrier mobility drops and threshold voltage increases with temperature and they will have an opposite effect on the frequency. So it is not obvious how the oscillation frequency changes by temperature. To figure this out, I measured the reference oscillation frequency under 690 lux illuminance. I put the test board on a heating plate and continuously measured the temperature of the chip package with a K thermocouple and the oscillating frequency as the temperature went up. The result is shown in Fig. 6.11.

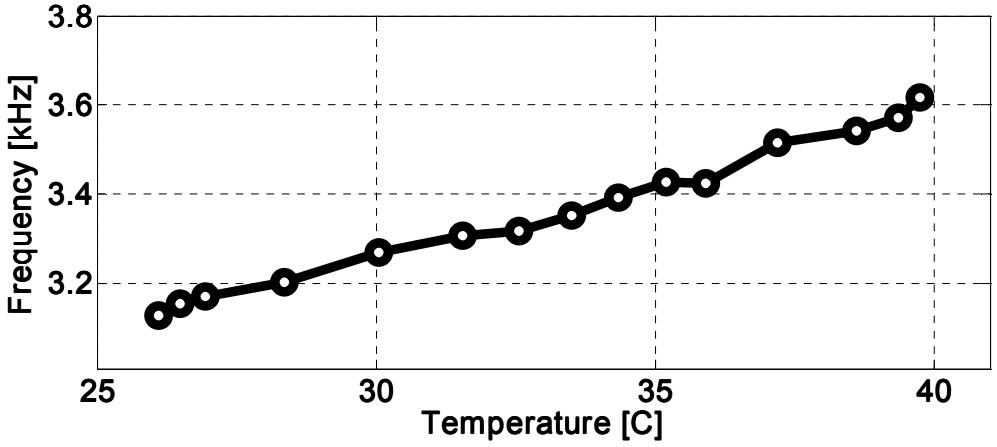

Figure 6.11: Reference frequency (R-mode) as a function of temperature at 690 Lux.

It is clear that the oscillation frequency is increasing with temperature. The reason is that the effect of the increase in the optical current and the decrease in the threshold voltage are dominant and hence the frequency increases.

6.7 FSK TEST

In this measurement, I verified the functionality of the timer, MUX, and electrode driver using the setup shown in Fig. 6.12.

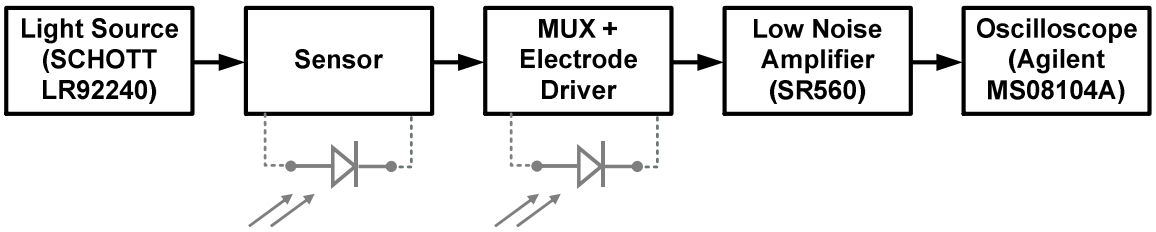

Figure 6.12: Setup for FSK test.

The sensor is functioning in the capacitive measurement mode, where the transducer capacitance is 10 pF. The output of the sensor and reference are fed into the multiplexer and consequently to the electrode driver. In this case, the output of the electrode driver is directly probed without being connected to the *in vivo* electrodes. The light source illuminace is equivalent to 1.42 klux. The transient output of the electrode driver and the timer signal are shown in Fig. 6.13.

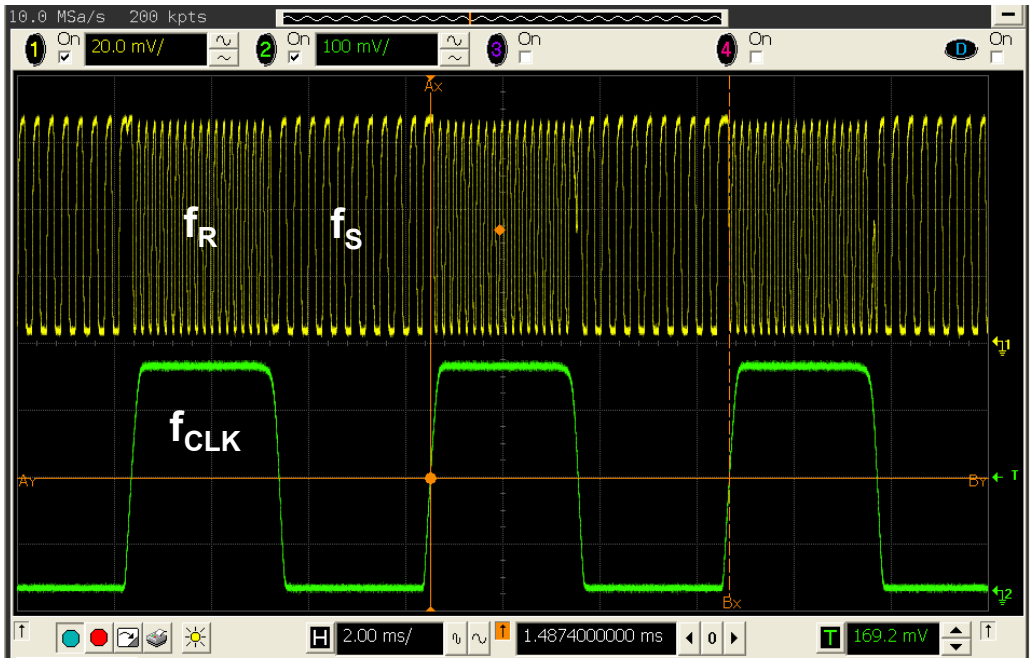

Figure 6.13: Transient output of the electrode driver in the FSK test.

The FSK output of the electrode driver is formed by the reference and sensor output signals with oscillation frequencies of 6.268 and 3.264 kHz respectively. Timer is generating a 160 Hz square-wave signal and facilitates the alternation of the output between reference and sensor signals.

6.8 *IN VITRO* MEASUREMENTS

In vitro validation experiments for this sensor were done in two parallel setups. In one setup, the transmission path using the subcutaneous electrodes was characterized while the other focused on energy harvesting. The main rationale behind this was the measurement practicality and the fact that special packaging is required to simultaneously do both. In the future implementation, this can be achieved by wirebonding the die output to the electrode and sealing the CMOS chip using a transparent yet biocompatible resin.

6.8.1 Electrode Coupling

As discussed in Chapter 5, a neuromorphic method is designed for transmission of the data to the outside world. In this method, the signal is dumped on a pair of electrodes and a conventional set of ECG electrodes picks up the signal from the top of the skin (see Fig. 6.14).

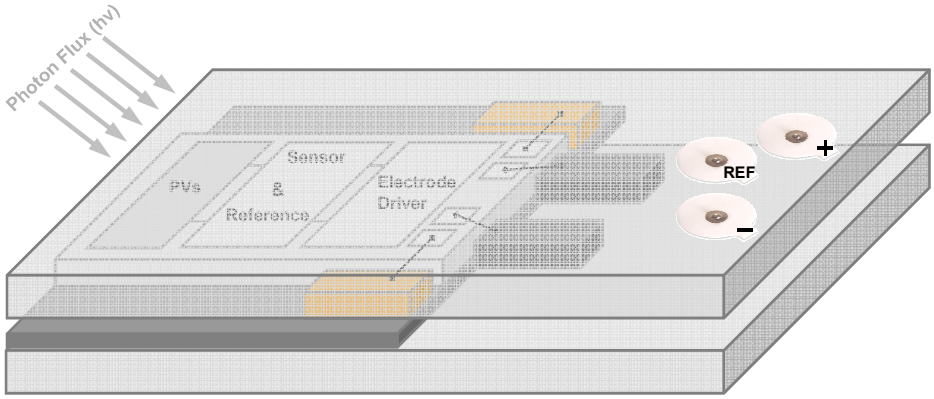

Figure 6.14: The tissue inserts some loss on the output signal from the device

In order to characterize this transmission technique, it should be known how the signal is modified when it is transmitted through the tissue from one set of electrodes inside to the other set on the top. The size of the *in vivo* electrodes should be chosen such that they do not increase the size of the device to make it infeasible for implantable applications. Therefore, the electrode pair size is expected to be around a few millimeters. On the other hand, the frequency range of the device is a few kHz. In this frequency range, the size of the electrode and the length of the signal path are much smaller than the wavelength of the signal ($\lambda \approx 10^5$ m). Under this condition, the signal transmission is not considered electromagnetic and the transmission can be expected to be only of resistive

coupling between the two sets of electrodes. This model is inspired by how the thoracic tissue is modeled for measuring body surface potentials in ECG readings (See Fig. 6.15).

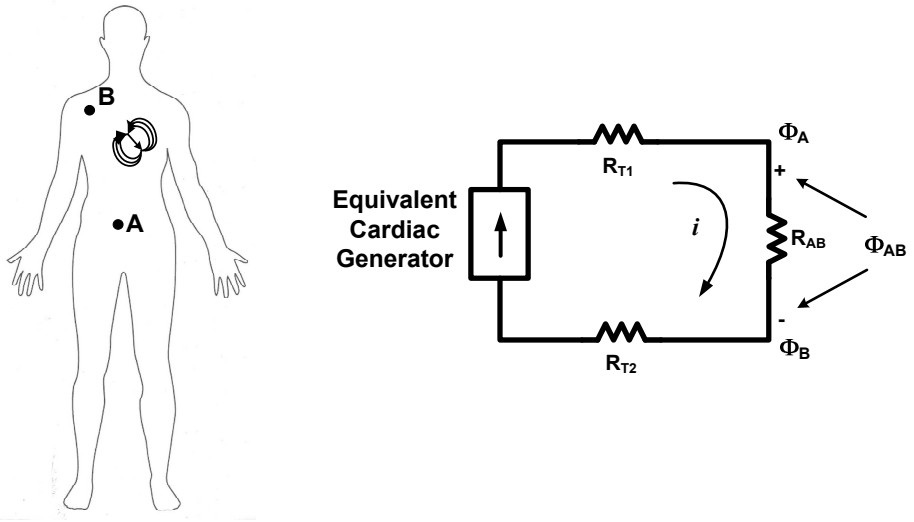

(a) (b)

Figure 6.15: The electrocardiographic problem [65].

The electric activity of the heart is modeled by an electric dipole which is located in the thorax [65]. The potential that is generated by this dipole appears in the whole body and on the surface. Fig. 6.15a illustrates the heart dipole in a human body at one instant of time. A and B are two observation points. If the observation points are located on different equal-potential lines of the electric field, a nonzero voltage can be measured between these two points and can be used to reveal the activity of the heart. Different pairs of observation points on the body will result in different voltages due to the spatial dependence of the electric field.

Fig. 6.15b shows the equivalent circuit diagram of 6.17a where R_{T1} and R_{T2} resemble thoracic medium resistances and R_{AB} is the resistance between the two points. Φ_A and Φ_B are the potentials of the A and B nodes to another reference potential. Φ_{AB} which is the difference between these two voltages is the reported voltage by this set of

electrodes and estimates the cardiac activity. Similarly, I have used a three-electrode set shown in Fig. 6.16. This setup was used to estimate the coupling between the subcutaneous electrode pair with the external ECG electrodes.

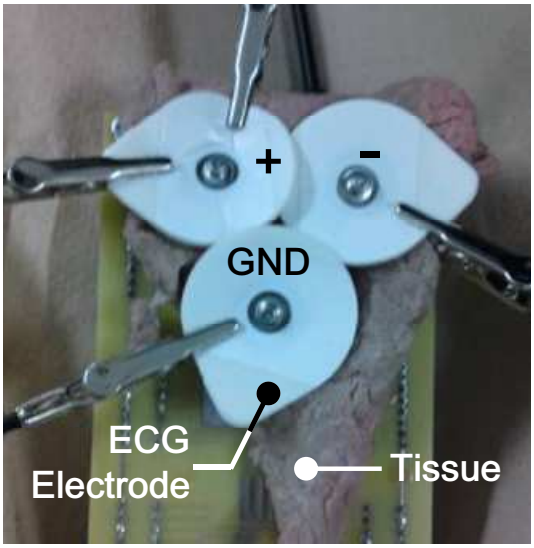

Figure 6.16: ECG electrode to implanted electrode coupling measurement setup across a 3mm thick slab of *post mortem* bovine muscle.

The *in vivo* electrode pair (also shown in Fig. 5.30) is located on the bottom board and cannot be seen in this figure. The tissue shown in Fig. 6.16 is a 3mm thick slab of *post mortem* bovine muscle. The ECG electrode setup contains three electrodes, one of which serves as a reference electrode (GND). The block diagram of the setup is shown in Fig. 6.17.

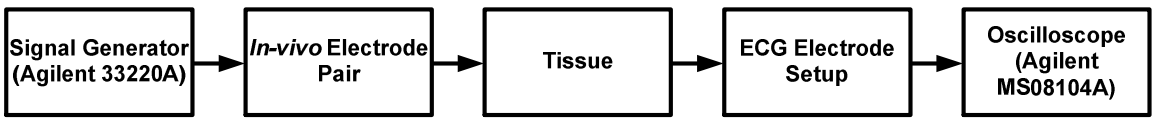

Figure 6.17: Block diagram of ECG electrode to implanted electrode coupling measurement setup.

The implantable to ECG electrode coupling was measured to be approximately -35dBV/V within the 0.1 to 20 kHz range as shown in Fig. 6.18.

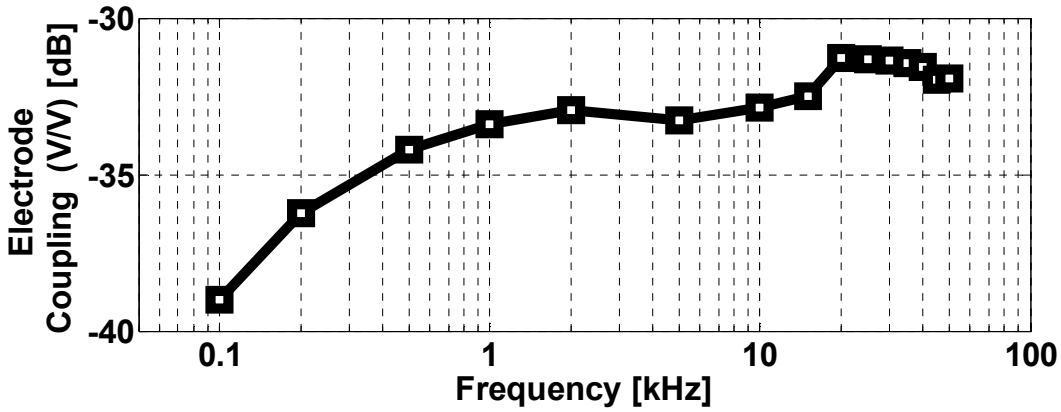

Figure 6.18: ECG electrode to implanted electrode measured coupling.

6.8.2 Sensor Tissue Test

The *in vitro* energy harvesting capabilities were tested in a setup (Fig. 6.19), where a 3mm thick *post mortem* bovine muscle (red meat) slab and 1~2 mm thick chicken skin were used to emulate tissue loss. The output of the chip in this setup was connected to 300nF ‖1kΩ external load which approximates the tissue load in the setup of Fig. 6.20.

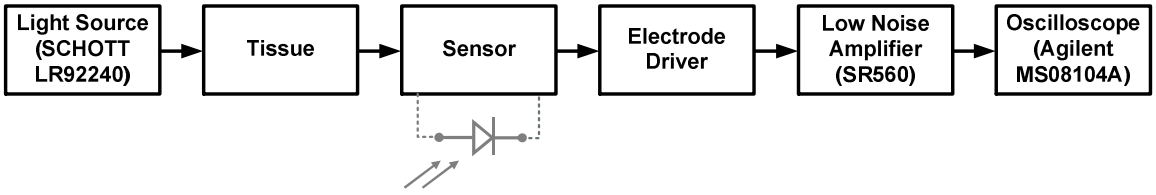

Figure 6.19: Block diagram of the sensor tissue test setup.

The variable light source (150-watt halogen microscope illuminator, SCHOTT LR92240 ACE-I) was applied from top and normal to the skin surface, while the CMOS chip was placed under the muscle slab beneath the skin. The illuminance in this setup was measured to be 15 klux which is equivalent to the illuminance of a sunny day with scattered clouds. Based on this number, 1.2 μW is available at the surface of the chip when no tissue is present. The presence of the tissue used in this setup attenuates this available power to approximately 120nW.

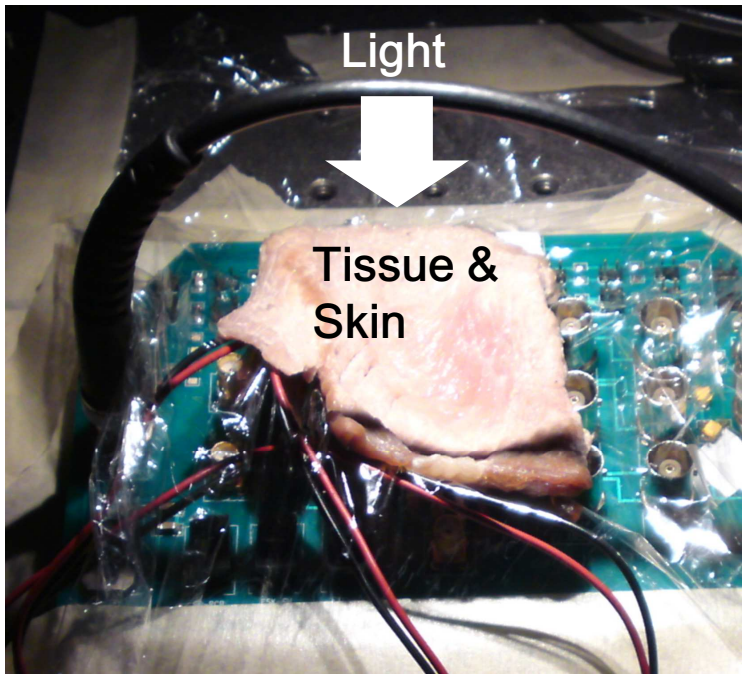

Figure 6.20: Sensor *in vitro* measurement setup. The chip is illuminated through a 3mm thick *post mortem* bovine muscle slab and 1~2 mm thick chicken skin.

Since the sensor circuitry input impedance do not coincide with the optimum operating point of the PV cells, the PV cell power transfer efficiency (the ratio between consumed to the maximum available power) was estimated to be around 23%. In average,

the sensor and reference blocks consumed around 11nW and the electrode driver consumes 19nW.

The measured output FSK signal is shown in Fig. 6.21. The frequency difference between the reference and the sensor phases in the FSK signal demonstrates the value of the measured capacitor which was 10pF. This particular result, considering the mV-range amplitude at the output of the CMOS chip, demonstrates that FSK signals with 10-100 μV magnitude can be generated on top of the skin. This value is well within the detection range of ECG systems.

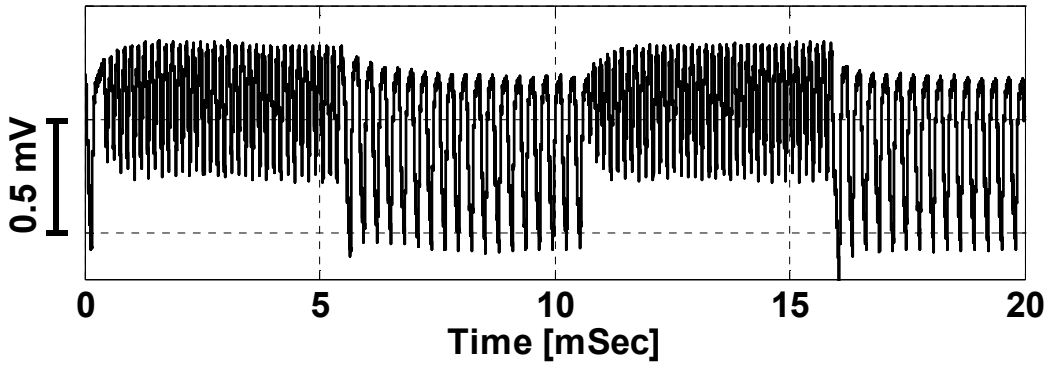

Figure 6.21: Measured FSK output signal at 15klux ambient light

6.9 SUMMARY

In this chapter, the measurement results of the fabricated CMOS implantable sensor were explained. The results show it is possible to run an ultra-low power circuit in an implantable device through optical power harvesting. This result suggests the

feasibility of implementation of MRI-compatible wirelessly powered implantable devices.

Chapter 7: Summary and Future Work

7.1 SUMMARY

This research demonstrates a new technique for delivering power to implanted devices. The goal of this project was to prove the feasibility of harvesting the energy of light passing through the tissue and converting it to electrical power by the use of integrated CMOS PV cells. In the previous chapters, the optical properties and the advantages and disadvantages of CMOS PV cells were. The optical loss of the body tissue depends on the type of the tissue but the bottom line is that around 20 dB/mm loss is expected in the visible range.

I also examined the characteristics of CMOS PV cells and found out under solar spectrum light conditions, and conclude that approximately 20 μA's short circuit current in a $1mm^2$-size $P+/N_{WELL}$ diode can be expected. Such devices, therefore, can give the maximum power of 10 μW when loaded with the optimum load. Putting all these results together, it can be concluded that the generation of 200nW power in a $1mm^2$ size PV cell when put under a slab of 2 mm-thick tissue is quite possible.

In order to empirically prove these assessments, the design and successful implementation of an implantable sensor was presented which can be run solely by on-chip CMOS PV cells fabricated on the same die. The measurement results confirm the primary conclusions and the implantable circuit can be operated by the light that is passed through an emulated tissue on top of the device.

To send the measurement results to the outside world, a neuromorphic method is proposed in which transferring the output signal of the sensor is applied to a pair of *in vivo* electrodes and can be picked up by an ECG electrode set on top of the tissue. The coupling of the two electrode sets across a 3mm-thick slab of *post mortem* animal meat

was measured. The results of the measurement, in addition to the sensor characterization results show that the signal amplitude at the ECG electrodes is adequate for precise reading of the *in vivo* signals.

7.2 FUTURE WORK

7.2.1 Full test in live animal

All of the measurements involving with tissues in this work have been done with *post mortem* muscle and skin tissues. The system is expected to work in an *in vivo* condition as well, as there is no fundamental difference between these two cases, which would annul the functionality of the system. However, the movement of the subject, body temperature changes, and the dynamic changes in the tissue optical loss due to blood circulation and other factors may deteriorate the performance of the sensor. This test is imperative before the functionality of such implants inside a live animal body can be confirmed. In order to do the tests, the *in vivo* electrodes should be wirebonded to the die and specific packaging should be used such that the device is sealed using a transparent yet biocompatible resin.

Another interesting subject to study is the effect of the body on the functioning of the PV cells when implanted in the body for a long time. It is important to have a long term analysis of the functionality of the implanted PV cells to be able to promise that such a system would not need frequent maintenance.

7.2.2 Design of ultra-low power regulators for CMOS PV cells

In this dissertation, the design of a device directly powered by the CMOS PV cells was introduced that had no storing or regulating element to enhance the supply

voltage and current. As shown in section 6.5, the fluctuations in the ambient light are observed in the PV short circuit current which directly affect the sensor output. On the other hand, the maximum available voltage from a single cell does not exceed its open circuit voltage, which is not sufficient for many applications. A higher level, regulated power supply is generally preferred. Therefore, it is very beneficial to include DC-DC converting and regulating blocks in more demanding applications. This might be quite challenging as the available power supply is usually limited and stepping up and regulating architectures can be power hungry and leaky. Therefore, a comprehensive study on the feasibility of PV voltage regulators is appropriate. This study can be divided to two categories. The first category involves design of voltage regulators for systems where a storing element, stores the harvested energy. In this category, unpredictable fluctuations in the optical energy source do not deteriorate the performance of the load. In the second category, the design of voltage regulators for real-time energy harvesting should be studied. The voltage regulators in this case must be able to suppress the random changes in the energy supply.

7.2.3 Study of the stochastic power supplies

Power harvesting supplies usually deal with energy supplies which are unregulated, unpredictable, and conditional. Generally, it is desired to have a reliable power supply which can provide a regulated power to feed the load. For this reason, many of the harvesting power supplies include modules to store and regulate the converted energy. The regulator needs power to start working and may be leaky and power hungry. It would be desirable if the power supplies can be used without any regulation or storage. A study on the possible circuit designs that can tolerate such kind

of power supplies namely “stochastic power supplies” is valuable. Although the harvesting energy sources might have a random nature, they are not completely unpredictable. The performance of the circuits that are run by such power supplies depends on the statistics of the available power. Burst mode designs are appropriate candidates for this application, where the output is only generated when adequate power exists in the supply. Apparently, the output will also be conditional, but will not be completely unknown. Depending on the average harvesting energy and its deviation, the low power circuit can be designed and expected to function.

Appendix A: Analysis of the Sensor in Capacitive Sensing Mode

In this section a detailed characterization of the sensor in capacitive sensing mode is discussed. This discussion is an extension to section 5.3.2.5.

The period of the designed sensor circuit can be written as:

$$T = T_1 + T_2 + T_3, \tag{A1}$$

where

$$T_i = T_{ri} + T_{fi}. \tag{A2}$$

T_{ri} and T_{fi} represent the rising and falling delay at the output of each stage in Fig. 5.10, when S=1. T_1 shows the delay in the first stage which is the modified inverter including the unknown component. T_2 denotes the delay in the Schmitt-trigger. The third stage is a simple inverter stage with a known load capacitance (C_0), so T_3 is known from (5.8). The graph shown in Fig. A1 illustrates the delay of the three stages for PV short circuit current values of $I_{SC} < 0.5\mu A$. The load capacitance of each stage is equal to the default value of 100fF.

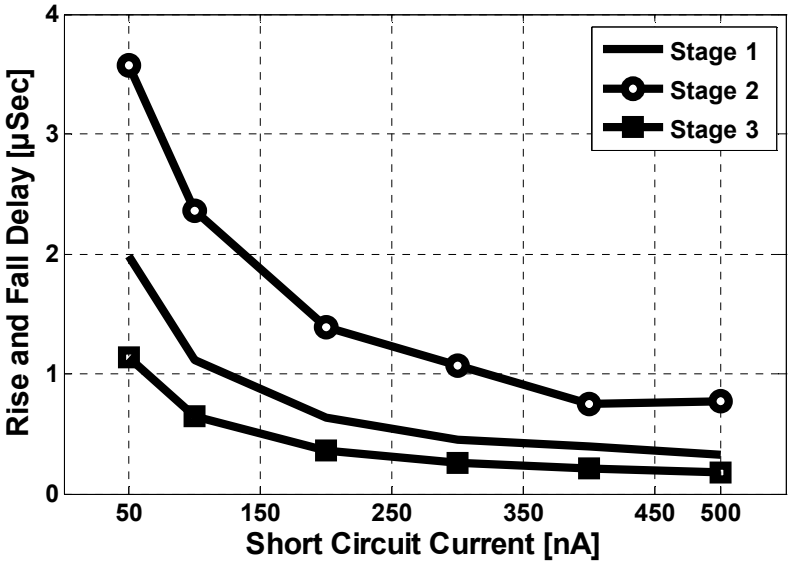

Figure A1: The rise and fall delays of three different stages of the sensor vs. PV short circuit current.

The presence of the switches in the first stage makes the delay of the first stage different from a simple inverter. There exists an offset between the two graphs due to the presence of the switch parasitic capacitors. In order to characterize this offset, the first stage rise and fall delays have been measured for various capacitance and current values and compared to the rise and fall delays of a simple inverter which is run by the same current and has the same load capacitance.

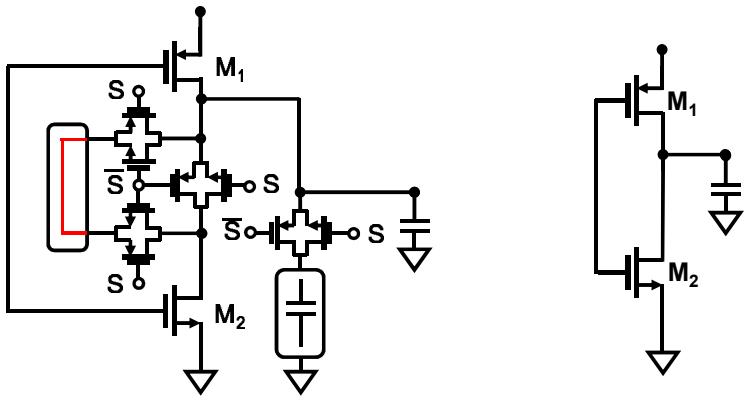

(a) (b)

Figure A2: Schematic of Stage 1 in capacitive sensing mode (a) with switches and (b) simplified

As shown in Fig. A3, this offset is a function of available current but almost constant for different values of load capacitance. By characterizing these values, it can be observed that the offset is due to about 35fF parasitic capacitor existing in the output of stage 1, when switches are present.

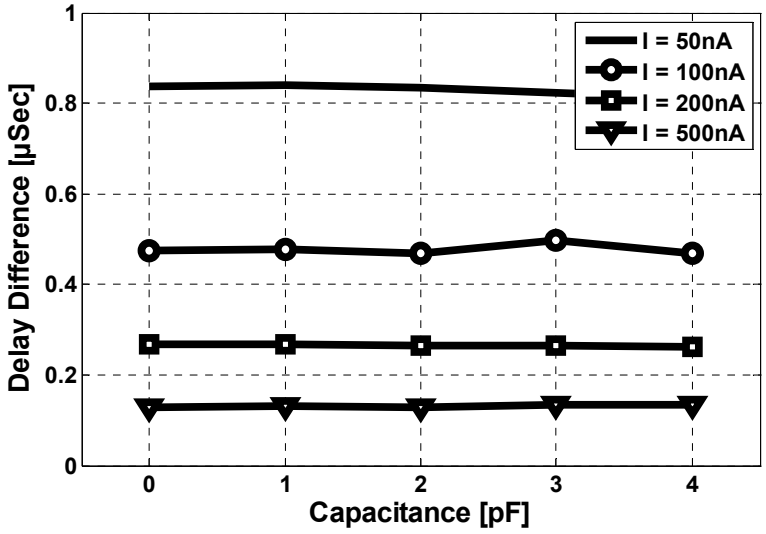

Figure A3: Delay offset between stage 1 and a CMOS inverter.

Finding a closed form for the delay of the second stage is not a trivial job, but I try to characterize it as much as possible by comparing the delay of that stage with a simple inverter stage through simulation. As shown in Fig. A4, the delay of the second stage (inverting Schmitt Trigger) is almost three times the delay of a simple inverter stage with the same loading capacitance.

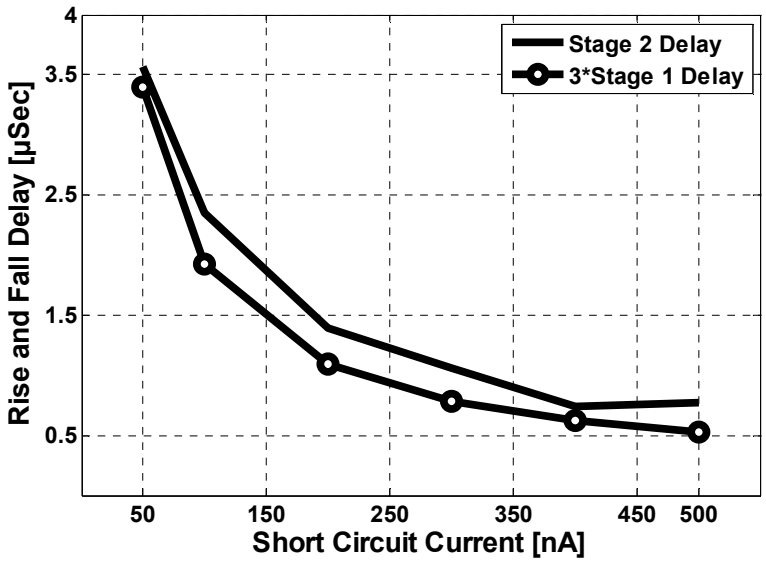

Figure A4: Comparison of the delay of the second stage with the simple inverter stage vs. PV short circuit current.

Appendix B: Analysis of the Sensor in Resistive Sensing Mode

In this section a detailed characterization of the sensor in resistive sensing mode is discussed. This discussion is an extension to section 5.3.2.5

In order to find out how the oscillation frequency changes with the available PV current and the unknown resistance in the resistive sensing mode, a simplified circuit is analyzed first. This circuit is an inverter with a resistor between its two devices, run by a PV cell.

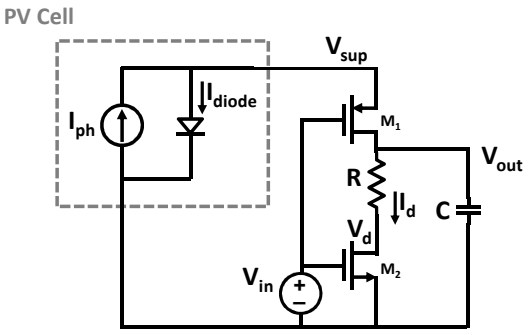

Figure B1: The first stage in the resistive sensing mode.

Since the resistor is present in the discharge path, the rising time of the stage output is not a function of the resistor and the delay is equivalent to the rising delay in the capacitive sensing mode. In order to understand the relation between falling delay and the resistance, a second-order modeling for the sub-threshold device is used. In this model, the drain current is formulated as below:

$$I_d = I_{d0} e^{\frac{V_{gs}}{nV_T}} \left(1 - e^{\frac{-V_{ds}}{V_T}} \right), \tag{B1}$$

where

$$V_{out} = V_d + I_d R. \tag{B2}$$

In (B1), I_{d0} denotes the drain saturation current of the transistor and n shows the diode ideality factor . V_T stands for the thermal voltage. Since the NMOS is off at this phase:

$$-\frac{1}{C}\int I_d dt = V_d + I_{d0} e^{\frac{V_{in}}{nV_T}} \left(1 - e^{\frac{-V_d}{V_T}}\right) R. \tag{B3}$$

Taking the time derivative of the upper equation (B3) will result in this nonlinear differential equation:

$$V_d' + \frac{V_d'}{nV_T} I_{D0} e^{\frac{V_{in}}{nV_T}} e^{\frac{-V_d}{V_T}} R + \frac{1}{C} I_{D0} e^{\frac{V_{in}}{nV_T}} \left(1 - e^{\frac{-V_d}{V_T}}\right) = 0, \tag{B4}$$

where

$$V_d' = \frac{\partial V_d}{\partial t}. \tag{B5}$$

Equation (B4) shows the nonlinear dependence of V_d and subsequently V_{out} with respect to R . It is not trivial to find a closed form for V_{out} as a function of R therefore, the dependence of the oscillation frequency to the unknown resistance and the available photocurrent can be characterized by simulation and measurements. In Fig. B2 it is shown how this delay varies as a function of R.

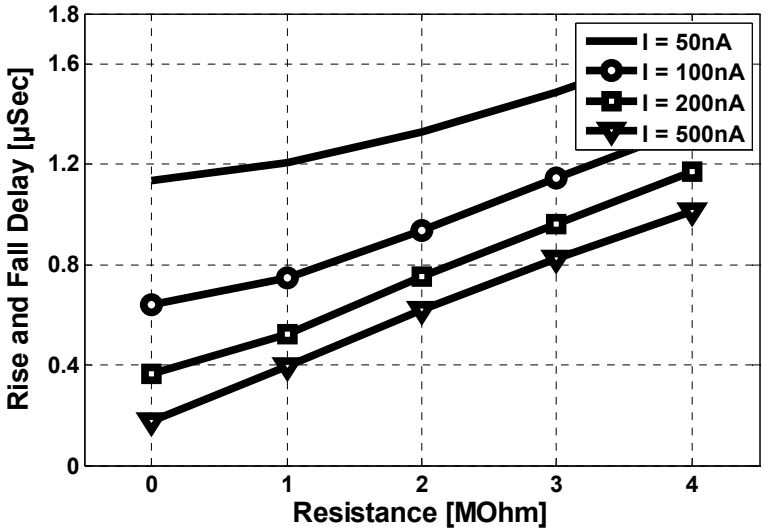

Figure B2: Rise and fall delay of the stage 1 in resistive sensing mode.

To figure out the effect of the switches on the observed delays, a comparison is done between the rise and fall delay of stage 1, when the switches exist and with the simple circuit without switches (see Fig. B3 (b)).

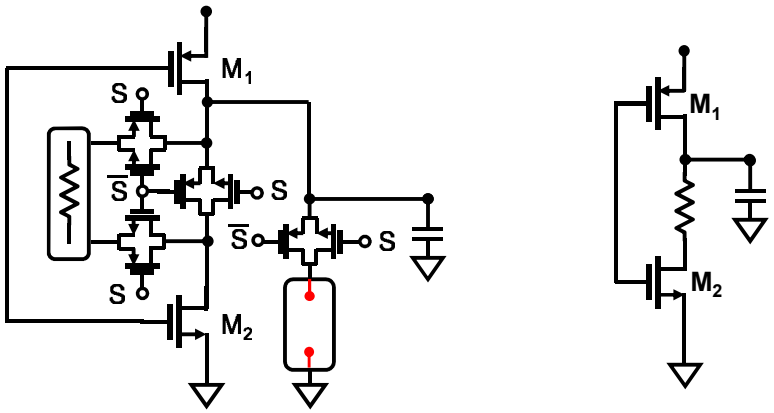

(a) (b)

Figure B3: Schematic of stage 1 in resistive sensing mode (a) with switches and (b) simplified

The graph shows in Figure B4 shows the difference between the delay of the resistor sensing stage and the simple inverter stage for various resistor values.

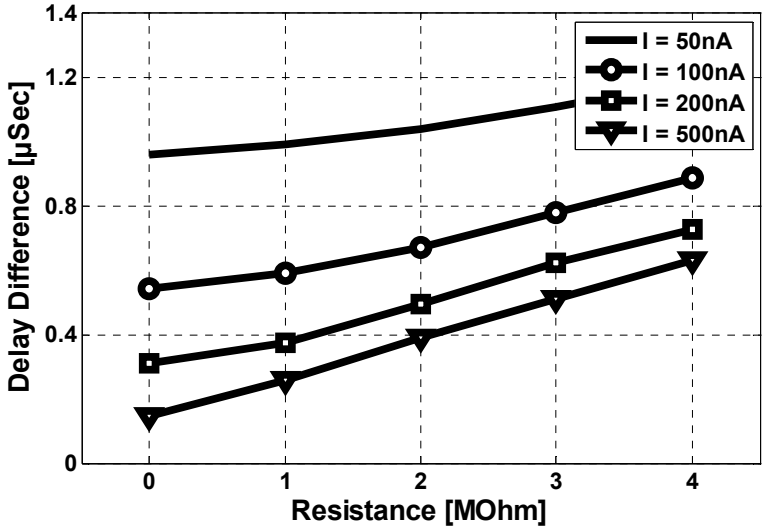

Figure B4 : Difference between rise and fall delay of the stage 1 in resistive sensing mode for switched mode and the simple mode.

Appendix C: Effects of Light Source Fluctuations on the Sensor Output

Different types of artificial light sources generate interference tones at different frequencies. The light sources can be categorized into three types: incandescent lamps, fluorescent lamps driven by conventional ballasts, and fluorescent lamps driven by electronic ballasts [75]. In [75] the interference signals produced by these light sources have been measured in a photodiode. Although the study in [75] is aimed to characterize the different environments for optical communication systems, it gives information about the fluctuations present in the ambient virtual light sources.

Six different incandescent lamps have been tested and they showed similar results. The incandescent lamps generate even harmonics of the main power lines up to 2kHz. For frequencies higher than 800 Hz the magnitude of the result is 60 dB smaller than the first harmonic.

According to [75] when a fluorescent light source with conventional ballast is used, the observed spectrum is not very regular and various tones are present up to 20 kHz. Although, the magnitude of the signal tones of frequencies higher that 5kHz are at least 50 dB smaller than the main tone. In addition, odd harmonics of the 50Hz is also observed in the spectrum.

In the other category of fluorescent lights, where the lights are driven by electronic ballasts, the switching frequency used to drive these lamps is different for different manufacturers and is in the range of 20 to 40 kHz. But generally, the tone at that frequency and its entire harmonics are observed in the spectrum in addition to the irregular tones seen in the case of the lamps with conventional ballast. The magnitudes of the tones in higher harmonics are comparatively larger. Some tones grow by 30 dB

around the second harmonic. According to [75], the magnitude of these fluctuations can rise up to 100% of the average irradiance.

There are other sources that generate unwanted signals and will be detected by the photodiodes. In [76] the RF spectrum from IR light transmission detected by the photodiode form two models of SONY IR headphones is shown. The strongest tones are located at 2.3 and 2.7 MHz and the spectrum extends to more than 15MHz. TV remote control is the most widely used IR transmitter in the houses [76]. The remote control transmitter is very directive and it will cause problems to the other detectors if it points to the receiver. Since the signals generated by these sources are at a distinct range of frequencies, they are not expected to affect this system.

Light Source	Interferer	Fluctuation magnitude (compared to the average irradiance)
Incandescent lamps	Even harmonics of the main power lines frequency	22%
Fluorescent lamps with conventional ballasts	Odd harmonics of the main power lines frequency and various tones up to 20 kHz	66 to 100%
Fluorescent lamps with electronic ballasts	Switching frequency and its harmonics in addition to the interferers for fluorescent lights with conventional ballast	30 to 44%

Table C1: Various light sources and their associated unwanted interferers

The study in [74], shows that variation in general ambient light sources are expected to be of the main lines and up to tens of kHz from incandescent and fluorescent lights. Let's see how these interferers appear in a photovoltaic cell.

6.3.4.1 Photovoltaic cell current fluctuation

The generated photocurrent is a function of junction parameters, such as junction depth and width and the light condition. Equation (1) shows the function.

$$j_{ph} = \frac{qF_0}{\alpha(\lambda)}\left\{\frac{1-e^{-\alpha(\lambda)x_1}}{x_1} - \frac{e^{-\alpha(\lambda)x_2} - e^{-\alpha(\lambda)x_3}}{x_3 - x_2}\right\} \qquad \text{(C1)}$$

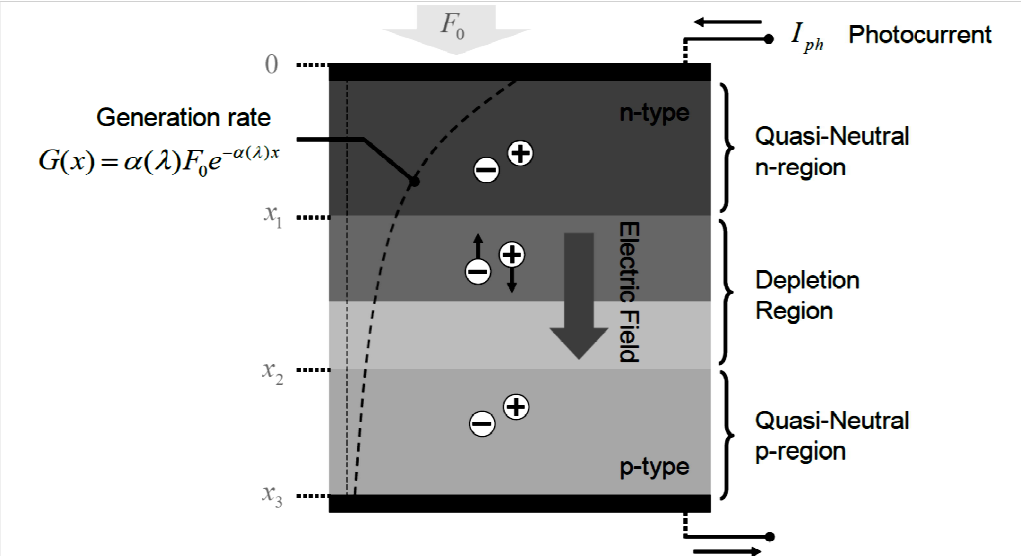

Figure C1: P-N junction under illumination

In this equation, the incoming photon flux is assumed to be constant with time. If the light source has fluctuations with time, the photon flux will be variable with time and it can be shown as . Therefore, the short circuit current formed in the PV cell will

also be time variable ($j_{ph}.f(t)$). When the power supply is modulated by a signal, it is expected that all the signals in the circuit get affected and have the unwanted tones if no protection is implemented.

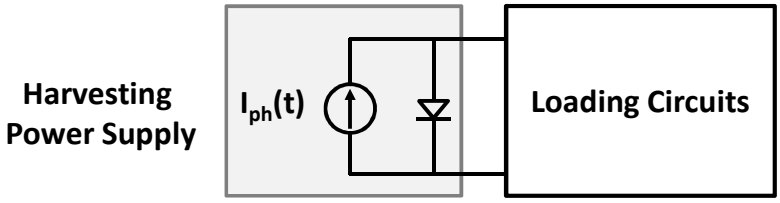

Figure C2: A system run by PV cells with fluctuations.

6.3.4.2 Sensor Simulation

In this section, the behavior of the circuit is studied when the light source has unwanted fluctuations. In the simulations, the PV cell is modeled by a diode in parallel with a current source which represents the short circuit current of the cell (Fig. C2). As explained above, the short circuit current is a function of photon flux. The fluctuations in the photon flux is modeled by a sinusoidal ripple on a DC source. Depending on the intensity of the fluctuations, the amplitude of this ripple will be a percentage of the DC current.

At first, the output spectrum of the reference circuit is studied when the light source is a constant photon flux. At this test, the short circuit current is assumed to be 40nA. At this current level, the oscillating frequency of the reference circuit is approximately 4.5 kHz. The power spectral density (PSD) of the output is shown in Fig. C3a. In this figure, the main tone and its harmonics are present. There exist other spurs, which are not significant because their magnitude is at least 30 dB less than the main signal and can be ignored at the output. In the second test, a 1kHz ripple is applied in the

current source modeling the PV cell. The magnitude of this ripple is 10% of the DC current. Fig. C3 shows how the PSD changes. In addition to the main tone (4.5 kHz) and its harmonics, unwanted signals are present around the main tone with an offset equivalent to the frequency of the ripple, which represents the light source fluctuations. The magnitude of the unwanted tones is 20 dB smaller than the main tone.

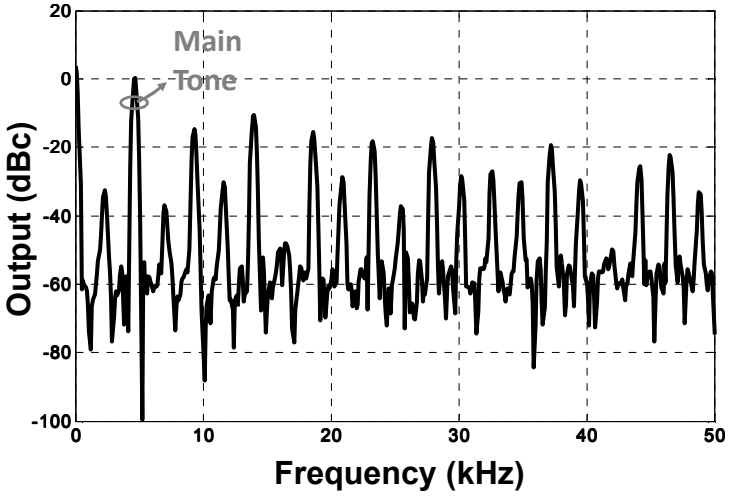

(a)

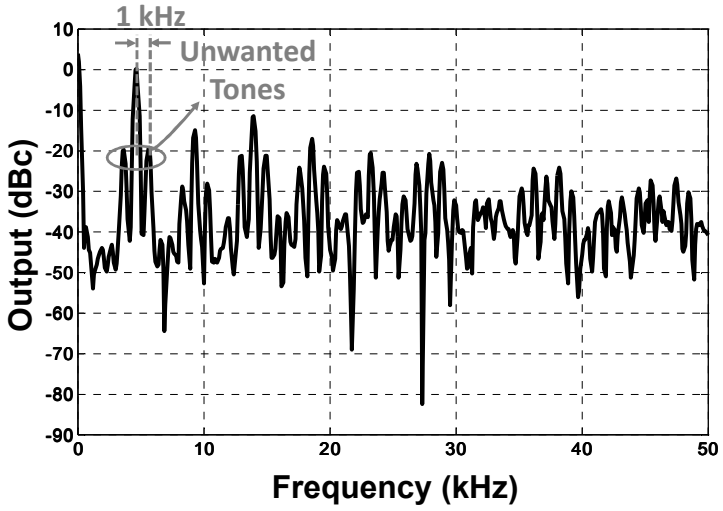

(b)

Figure C3: Output of the reference when driven by (a) constant photon flux, (b) fluctuating photon flux.

This misrepresentation by the interferers can be avoided by applying filters at the power supply node. For example if a low pass filter is used by adding a capacitance at the power supply node, the unwanted tones can be attenuated. The PV cell itself has an internal capacitance approximately equal to 1nF/mm^2. According to the simulation results, 12 dB of attenuation is observed in unwanted signals by introducing 1n F of capacitance at the supply node (see Fig. C4).

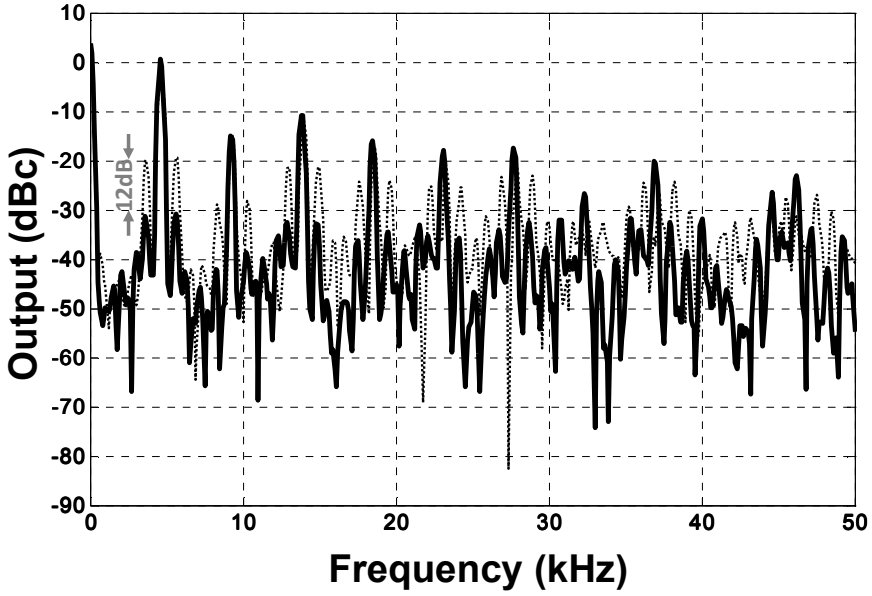

Figure C4: Suppression of the unwanted tones by filter

References

[1] Zoll, P. M., Frank, H. A., Zarsky, L. R. N., Linenthal, A. J. and Belgard, A. H., "Long-term electric stimulation of the heart for Stokes-Adams disease," Ann. Surg., 154: 330,196l

[2] Parkins, C. W., "Cochlear Implant: A Sensory Prosthesis Frontier," Engineering in Medicine and Biology Magazine, vol. 2(2), pp. 18-27, June 1983.

[3] Troup, P., "Early development of defibrillation devices," Engineering in Medicine and Biology Magazine, vol. 9(2), pp. 19-24, June 1990.

[4] Koudelka-Hep, M., de Rooij, N.F. , "*In vivo* evaluation of an amperometric glucose sensor implanted subcutaneously in rats," Engineering in Medicine and Biology Society, vol.1, pp. 155-156, Oct. 1992.

[5] Collins, C. C., "Miniature Passive Pressure Transensor for Implanting in the Eye," IEEE Transactions on Biomedical Engineering, vol. BME-14(2), pp. 74-83, Apr. 1967.

[6] Shill, H. A., Setter, A. G., "Reliability in deep brain stimulation," IEEE Transactions on Device and Materials Reliability, vol. 5(3), pp. 445-448, Sept 2005.

[7] Mouine, J., Ali Ammar, K., "A miniaturized implantable spinal cord microstimulator for treating intractable chronic pain," 1st Annual International Conference On Microtechnologies in Medicine and Biology, pp. 630-634, 2000.

[8] Oesterle et al., "New Interfaces to the Body through Implantable System Integration," ISSCC Tech Digest, 2011

[9] Ji J. and Wise K. D., "An implantable CMOS circuit interface for multiplexed multielectrode recording arrays," IEEE J. Solid-State Circuits, vol. 27, pp. 433–443, Mar. 1992.

[10] Santhanam G., Linderman M. D., Gilja V., Afshar A., Ryu S. I., Meng T. H., and Shenoy K. V., "HermesB: A Continuous Neural Recording System for Freely Behaving Primates," IEEE Trans. BIOCAS, vol. 54(11), pp. 2037 - 2050, Nov. 2007.

[11] Leung A. M., Ko W. H., Spear T. M., and Bettice J. A., "Intracranial pressure telemetry system using semicustom integrated circuits," IEEE Trans. Biomed. Eng., vol. BME-33, pp. 386–395, Apr. 1986.

[12] Dorman M. G., Prisbe M. A., and Meindl J. D., "A monolithic signal processor for a neurophysiological telemetry system," IEEE. J. Solid- State Circuits, vol. SC-20, pp. 1185–1193, Dec. 1985.

[13] Akin T., Najafi K., and Bradley R. M., "A wireless implantable multichannel digital neural recording system for a micromachined sieve electrode," IEEE J. Solid-State Circuits, vol. 33, no. 1, pp. 109–118, Jan. 1998.

[14] Zoll, P. M., Frank, H. A., Zarsky, L. R. N., Linenthal, A. J. and Belgard, A. H., "Long-term electric stimulation of the heart for Stokes-Adams disease," Ann. Surg., 154: 330,196l

[15] Smith B., Peckham P. H., Keith M. W., and Roscoe D. D., "An externally powered, multichannel, implantable stimulator for versatile control of paralyzed muscle," IEEE Trans. Biomed. Eng., vol. BME-34, pp. 499–508, July 1987.

[16] Allen H. V., Knutti J. W., and Meindl J. D., "Integrated power controllers and RF data transmitters for totally implantable telemetry," Biotelemetry Patient Monit., vol. 6, pp. 147–159, 1979.

[17] Galbraith D. C., "An implantable multichannel neural stimulator," Ph.D. dissertation, Stanford Univ., Stanford, CA, Dec. 1984.

[18] Yang L., Chow E. Y., Irazoqui P. P., Chappell W., "RF Powering for Embedded Glaucoma Sensors in Miniature Packages," Proceedings of the URSI General Assembly, Chicago, IL (Aug, 2008)

[19] Kurup, D., Joseph, W., Vermeeren, G. and Martens L., "Path-Loss Model for In-Body Communication in Homogeneous Human Muscle Tissue," Electronics Letters, vol. 45(9), pp. 453 - 454, April 2009.

[20] Yuce, M. R.,W. P. Ng, S., Myo, N. L., Khan, J. Y., Liu, W., "Wireless Body Sensor Network Using Medical Implant Band," Journal of Medical Systems, vol. 31(6)

[21] Handa, T., et. al, "A Very Low-Power Consumption Wireless ECG Monitoring System Using Body as a Signal Transmission Medium," Solid-State Sensors, Actuators and Microsystems Conference, vol. 2, pp. 1003 – 1006, Chicago, 1997.

[22] Jow, U., and Ghovanloo, M., "Optimization of Data Coils in a Multiband Wireless Link for a Neuroprosthetic Implantable Devices," IEEE Trans. BIOCAS, June 2010.

[23] Greatbatch, W., Holmes, C. F., "History of Implantable Devices," IEEE Engineering in Medicine and Biology, pp. 38-49, Sep. 1991

[24] Leung A. M., Ko W. H., Spear T. M., and Bettice J. A., "Intracranial pressure telemetry system using semicustom integrated circuits," IEEE Trans. Biomed. Eng., vol. BME-33, pp. 386–395, Apr. 1986.

[25] Dorman M. G., Prisbe M. A., and Meindl J. D., "A monolithic signal processor for a neurophysiological telemetry system," IEEE. J. Solid- State Circuits, vol. SC-20, pp. 1185–1193, Dec. 1985.

[26] Smith B., Peckham P. H., Keith M. W., and Roscoe D. D., "An externally powered, multichannel, implantable stimulator for versatile control of paralyzed muscle," IEEE Trans. Biomed. Eng., vol. BME-34, pp. 499–508, July 1987.

[27]Allen H. V., Knutti J. W., and Meindl J. D., "Integrated power controllers and RF data transmitters for totally implantable telemetry," Biotelemetry Patient Monit., vol. 6, pp. 147–159, 1979.

[28] Ko, W. H., Liang, S. P., and Fung, C. D., "Design of radio-frequency powered coils for implant instruments," Med. Biol. Eng., Comput., vol. 15, pp. 634–640, 1977.

[29] Ghovanloo et al., "A Wide-Band Power-Efficient Inductive Wireless Link for Implantable Microelectronic Devices Using Multiple Carriers" IEEE Trans. CAS I, vol. 54(10), pp. 2211 - 2221, Oct. 2007.

[30] Tang, Z., Smith, B., Schild, J. H., and Peckham, P. H., "Data Transmission from an Implantable Biotelemeter by Load-Shift Keying Using Circuit Configuration Modulator," IEEE Transactions on Biomedical Engineering. vol. 42. No 5. May 1995

[31] Yang, L., Chow, E. Y., Irazoqui, P. P., Chappell W., "RF Powering for Embedded Glaucoma Sensors in Miniature Packages," Proceedings of the URSI General Assembly, Chicago, IL (Aug, 2008)

[32] Heetderks, W. J., "RF Powering of Millimeter- and Submillimeter-Sized Neural Prosthetic Implants," IEEE Transactions On Biomedical Engineering, Vol. 35, No. 5, May 1988

[33] Chaimanonart, N., and D. J. Young, "Remote RF Powering System for Wireless MEMS Strain Sensors," IEEE Sensors Journal, Vol. 6, No. 2, April 2006

[34] Chen, H., Liu, M., Jia, C., and Wang, Z., "Power Harvesting Using PZT Ceramics Embedded in Orthopedic Implants," IEEE Transactions on Ultrasonics, Ferroelectrics, and Frequency Control, vol. 56, no. 9, Sep. 2009

[35] Torres, E. O., and Rincón-Mora, G. A., "A 0.7-µm BiCMOS Electrostatic Energy-Harvesting System IC," IEEE Journal Of Solid-State Circuits, Vol. 45, No. 2, Feb. 2010

[36] Venkatasubramanian, R., Watkins, C., Stokes, D., Posthill, J. and Caylor, C., "Energy Harvesting for Electronics with Thermoelectric Devices using Nanoscale Materials," Electron Devices Meeting, pp 367-370, Dec. 2007

[37] Welch, A. J. and Van Gemert, A. J. C., Optical-Thermal Response of Laser-Irradiated Tissue, Plenum Press, New York, 1995.

[38] Cheong, W., Prahl, S.A., and Welch, A.J. (1990) A review of the optical properties of Biological Tissues. IEEE J. of Quantum Electronics, 26(12), 563-568.

[39] http://omlc.ogi.edu/classroom/ece532/class3/muaspectra.html

[40] Segelstein, D. J., "The complex refractive index of water," University of Missouri-Kansas City, (1981).

[41] Prahl, S. (http://omlc.ogi.edu/spectra/hemoglobin/summary.html)

[42] Pieter van der Zee, "Measurement And Modelling of the Optical Properties of Human Tissue in the Near Infrared," PhD thesis, The University of London

[43] Wilksch, P.A., Jacka, F., Blake, A.J. (1984) in: Porphyrin localisation and treatment of tumours. ed. Doiron, D.R. and Gomer, C.J., Alan Liss, New York, 149-161.

[44] Wilson, B.C., Patterson, M.S., Burns, D.M. (1986) 'Effect of photosensitiser concentration in tissue on the penetration depth of photoactivating light', Lasers in Medical Science, 1, 235-244.

[45] Flock, S.T., Wilson, B.C., Patterson, M. (1987) 'Total attenuation coefficients and scattering phase functions of tissues and phantom materials at 633 nm', Medical Physics, 14, 835-841.

[46] Karagiannes, J.L., Zhang, Z., Grossweiner, B., Grossweiner, L.I. (1989) "Applications of the 1-D diffusion approximation to the optics of tissues and tissue phantoms," Applied Optics, 28, 2311-2317

[47] Marchesini, R., Bertoni, A., Andreola, S., Melloni, E., Sichirollo, A.E. (1989) "Extinction and absorption coefficients and scattering phase functions of human tissues *in vitro*," Applied Optics, 28, 2318-2324.

[48] Anderson, R.R., Parrish, J.A., "The optics of human skin", Journal of Investigative Dermatology, 77, 13-19, 1981

[49] Anderson, R.R. "Tissue optics and photoimmunology," in: Photo-Immunology, Ed. Parrish, J.A., Kripke, M.L., Morrison, W.L., Plenum Publishing Corporation, NY. (1983)

[50] Diffy, B.L., "A mathematical model for ultraviolet optics of skin," Physics in Medicine and Biology, 28, 647-657. (1983)

[51] Everett, M.A., Yeargers, E., Sayre, R.M., Olson, R.L., "Penetration of epidermis by ultraviolet rays", Photochemistry and Photobiology, 5, 533-542. (1966)

[52] Bruls, W.A.G. (1984) PhD thesis.

[53] Bruls, W.A.G., van der Leun, J.C., "Forward scattering properties of human epidermal layers," Photochemistry and Photobiology, 40, 231-242. (1984)

[54] van Gemert, M.J.C., Jacques, S.L., Sterenborg, H.J.C.M., Star, W.M., "Skin Optics," IEEE transactions on Biomedical Engineering, 36, 1146-1154. (1989)

[55] Wan, S., Anderson, R.R., Parrish, J.A., "Analytical modelling for the optical properties of the skin with *in vitro* and *in vivo* applications," Photochemistry and Photobiology, 34, 493-499. (1981)

[56] Jacques, S.L., Alter, C.A., Prahl, S.A. "Angular dependence of HeNe laser light scattering by human dermis," Lasers in the Life Sciences, 1, 309-333. (1987)

[57] Salih, F. M., "Effect of clothing varieties on solar photosynthesis of previtamin D3: an in vitro study," Photodermatology, Photoimmunology & Photomedicine, Vol. 20, Issue 1, pp 53-58, Feb. 2004.

[58] Nelson J., The Physics of Solar Cells, Imperial College Press, 2008.

[59] http://rredc.nrel.gov/solar/spectra/am1.5/

[60] Stephenson et al., "Energy Transport through Tissue by Inductive Coupling," The American Journal of Surgery Volume 114, Issue 1, July 1967, Pages 87-94

[61] http://www.revisemri.com/questions/safety/safe_compatible

[62] Siegel, D., Garabieta, I., Hollerbach, J., "An integrated tactile and thermal sensor," International Conference on Robotics and Automation, pp. 1286-1291, Vol. 3, 1986

[63] Ylimaula, M., Aberg, M., Kiihamaki, J., Ronkainen, H., "Monolithic SOI-MEMS capacitive pressure sensor with standard bulk CMOS readout circuit," 29th European Solid-State Circuits Conference, pp. 611-614, Sep. 2003.

[64] Shih, Y., Shen, T., Otis, B., "A 2.3uW Intraocular Pressure/Temperature Monitor," IEEE Asian Solid-State Circuits Conference (A-SSCC), November 2010.

[65] Webster, J. G., "Medical Instrumentation Application and Design," Third Edition, John Wiley & Sons, Inc.

[66] Rabaey J., Chandrakasan A., and Nikolic B. "Digital Integrated Circuits," Prentice Hall, 2003

[67] Filanovsky, I. M., Baltes, H., "CMOS Schmitt trigger design," IEEE Transactions on Circuits and Systems I: Fundamental Theory and Applications, Vol. 41, Issue: 1, pp. 46 – 49, 1994

[68] Hassibi A., Navid R., Dutton R. W., and Lee T. H., "Comprehensive Study of Noise Processes in Electrode Electrolyte Interfaces," Journal of Applied Physics, vol. 96(2), pp. 1074 - 1082, Jul. 2004.

[69] Jacobs P., Varlan A., and Sansen W., "Design optimisation of planar electrolytic conductivity sensors," Medical & Biological Engineering and Computing, vol. 33, pp. 802-810, Nov. 1995.

[70] Faes T. J. C., Meij H.A. van der, De Munk J.C., and Heethar R. M., "The electric resistivity of human tissues (100 Hz–10 MHz): a metaanalysis of review studies," Physiol. Meas., vol. 20(4), R1-R10, 1999.

[71] http://zeiss-campus.magnet.fsu.edu/articles/lightsources/tungstenhalogen.html

[72] Chang, P. C., Peng, H. M., Lin, S. Y., "Allan Variance Estimated by Phase Noise Measurements," 36th Annual Precise Time and Time Interval Meeting, 2004.

[73] Wurfel, P., Physics of Solar Cells. Wiley-VDH, 2005, ch. 7.

[74] Streetman, B. G., Banerjee, S., "Solid State Electronic Devices," Prentice Hall, 2005

[75] Moreira, A. J. C., Valadas, R. T., de Oliveira Duarte, A. M.,"Characterisation and Modelling of Artificial Light Interference in Optical Wireless Communication Systems," The 1995 Sixth IEEE International Symposium on Personal, Indoor and Mobile Radio Communications (PIMRC'95) Toronto, Canada, September 27-29, 1995

[76] Boucouvalas, A.C., "Indoor ambient light noise and its effect on wireless optical links," Optoelectronics, IEE Proceedings, Vol. 143, Issue 6, 1996, pp 334 - 338